ABSTRACT

Title of Dissertation: HIGH REPETITION RATE LASER-DRIVEN ELECTRON ACCELERATION TO MEGA-ELECTRON-VOLT ENERGIES

Fatholah Salehi
Doctor of Philosophy 2019

Dissertation directed by: Professor Howard Milchberg
Department of Physics

Laser-driven particle accelerators have the potential to be a compact and cost-effective replacement for conventional accelerators. Despite the significant achievements of laser wakefield acceleration in the last two decades, more work is required to improve the beam parameters such as the energy spread, emittance, repetition rate, and maximum achievable energy delivered by these advanced accelerators to values comparable to what conventional accelerators offer for various applications.

The goal of this dissertation is to lower the threshold of the laser pulse energy required for driving a wakefield and in turn enable higher repetition rate particle acceleration with current laser technology. In the first set of electron acceleration experiments presented in this dissertation, we show that the use of a thin gas jet target with near critical plasma density lowers the critical power for relativistic self-

focusing and leads to electron acceleration to the ~MeV range with ~1pC charge per shot, using only ~1mJ energy drive laser pulses delivered by a 1kHz repetition rate laser system. These electron beams accelerated in the self-modulated laser wakefield acceleration (SM-LWFA) regime have a thermal energy distribution and a rather large divergence angle (>150mrad). In order to improve the energy spread and the divergence, in the second set of the experiments, we employ a few-cycle laser pulse with a ~7fs duration and ~2.5mJ energy as the driver, to perform wakefield acceleration in the bubble regime using near critical plasma density targets. The results show a significant improvement in the energy spread and divergence of the beam. The electron bunches from this experiment have a quasi-monoenergetic peak at ~5MeV with an energy spread of $\Delta E/E \simeq 0.4$ and divergence angle of ~15mrad.

These results bring us closer to the use of tabletop advanced accelerators for various scientific, medical, and industrial applications.

HIGH REPETITION RATE LASER-DRIVEN ELECTRON ACCELERATION TO MEGA-ELECTRON-VOLT ENERGIES

by

Fatholah Salehi

Dissertation submitted to the Faculty of the Graduate School of the
University of Maryland, College Park, in partial fulfillment
of the requirements for the degree of
Doctor of Philosophy
2019

Advisory Committee:
Professor Howard Milchberg, Chair
Professor Wendell Hill
Professor Abolhassan Jawahery
Professor Phillip Sprangle
Doctor Jared Wahlstrand

Dedication

Dedicated to my mother, Batool Salehi, and to the memory of my father, Ali Salehi.

Acknowledgements

"*Do not seek water, get thirst, so that the water may gush forth from above and below*" Rumi

I would like to thank my adviser, Professor Howard Milchberg for providing me the opportunity to work in his group. Howard's work ethic and passion for physics are really inspiring. I have learned a lot from him during my time in his lab, and I am grateful for his guidance, support, and encouragement.

I would like to thank my fellow lab mates and especially Andy Goers, Sina Zahedpour, and George Hine, for teaching me how to work with lasers and lab equipment during my first days in the lab. It was a pleasure to collaborate and work with Eric Rosenthal, Nihal Jhajj, Bo Miao, Ilia Larkin, Linus Feder, Daniel Woodbury, Robert Schwartz, and Scott Hancock. I am very happy and grateful for having the chance to work with all of them and learn from them. I am glad to see our newer lab members Manh Le, Jaron Shrock, and Andrew Goffin, have already made great progress in their research, and I am expecting very exciting research outcomes from the lab in coming years. I appreciate the help from our undergraduate researchers Ryan Smith, Dan Younis, Jesse Griff-McMahon, and Luke Pascal, and I wish them the best in their journey ahead. I would also like to thank Dr. Jared Wahlstrand, Prof. Ki-Yong Kim and his former lab members Yungjun Yoo, and Donghoon Kuk for the productive discussions and their help with experiments.

I would like to thank IREAP staff members for the help with administrative services. The machine shop crew, and in particular, Don Schmadel, Nolan Ballew, Jay Pyle,

Thomas Weimar, and Bryan Quinn have been a great help with equipment maintenance, machining, and mechanical designs, and for that, I am grateful to them.

Outside the lab, I would like to thank all my friends who have helped to create memorable moments at poetry nights, outdoor trips, sports leagues, and physical activities during the last few years.

Finally, I do not know how to thank my family back in Iran for their patience and unconditional love and support every step of the way. I could not have accomplished any of this work without their support. Thank you for everything.

Table of Contents

List of Figures

List of Abbreviations

BBO	beta barium borate
CCD	charge-coupled device
CEP	carrier envelope phase
CPA	chirped pulse amplification
DLA	direct laser acceleration
FROG	frequency-resolved optical gating
FWHM	full width at half maximum
GDD	group delay dispersion
GVD	group velocity dispersion
HCF	hollow-core fiber
HC-PCF	hollow-core photonic crystal fiber
ID	inner diameter
IR	infrared
LWFA	laser wakefield acceleration
MPI	multiphoton ionization
Nd:YLF	neodymium-doped yttrium lithium fluoride
OAP	off-axis parabolic
OPCPA	optical parametric chirped pulse amplification
PIC	particle-in-cell
RF	radio frequency
SC	supercontinuum
SHG	second harmonic generation
SM-LWFA	self-modulated laser wakefield acceleration
SPIDER	spectral phase interferometry for direct electric-field reconstruction
SPM	self-phase modulation
TG	transient grating
Ti:sapphire	titanium-doped sapphire
YAG	yttrium aluminum garnet

Chapter 1: Introduction

1.1 Motivation

High energy particle accelerators are well known for their critical role in fundamental physics discoveries, but they also have a wide variety of applications in industry, medicine, security, and energy and environmental fields [1]. There is a large demand for charged particle beams at a wide range of energies spanning less than a mega-electron-volt (MeV) up to a tera-electron-volt (TeV). Particle accelerators employ electric and magnetic fields in various designs and geometries to convert field energy into charged particle kinetic energy, and to steer, transport and focus them [2].

In an accelerator employing radio frequency (RF) electromagnetic fields, such as linear accelerators (linacs), the maximum electric field is limited by the electrical breakdown of the accelerator structure's material to $\sim 100 MV/m$ [3,4]. This sets a minimum length for linacs depending on target energy. For a circular accelerator design, where a charge bunch can circulate many times and gain more energy, the strength of the superconducting bending magnets used for steering the beam, and the synchrotron radiation losses, set the minimum radius for the accelerators; they are larger and more expensive for higher target energies. The top panel of Fig. 1.1 shows an aerial photo of Stanford Linear Accelerator Center (SLAC). The 3.2km long SLAC linac, composed of a sequence of RF cavities fed by klystron RF tubes, can accelerate electrons up to $50 GeV$. Current schemes for linear colliders propose

accelerators tens of kilometers long for electrons/positrons to reach the $\sim TeV$ energy range [5].

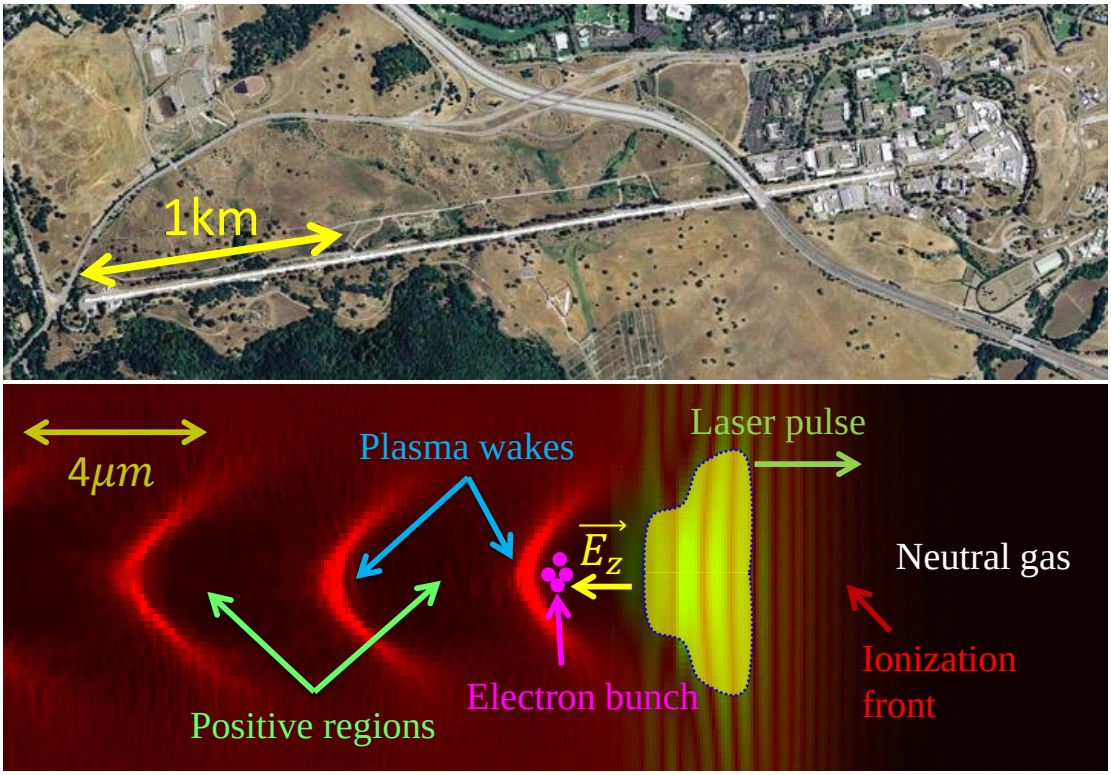

Figure 1.1. Conventional accelerator compared to a laser wakefield accelerator. (Top) aerial photo of Stanford Linear Accelerator Center (SLAC), a 3.2 km long RF accelerator which can accelerate electrons up to ~50GeV. (https://www6.slac.stanford.edu). (Bottom) Particle-in-cell simulation result illustrating laser driven wakefield acceleration of electrons.

With RF accelerators running into cost and physical size limits, developing a new generation of compact, portable, and cost-effective accelerators is necessary and beneficial for many applications. Laser-plasma based acceleration proposed about forty years ago [6], is a leading concept for a new generation of accelerators, using plasma waves formed in the wake of a high intensity laser pulse as the accelerating structure.

Plasmas, being already ionized, avoid the electrical breakdown problem, and can handle accelerating electric fields thousands of times larger than conventional accelerators, exceeding the $100GV/m$ range [7]. This technique could potentially shrink a 50 GeV accelerator size from many kilometers down to a number of room size laser-driven stages (possibly less than 10), and in turn, lower the final costs significantly [8]. The bottom panel of Fig. 1.1 shows a particle-in-cell (PIC) simulation result illustrating laser-driven electron acceleration. The laser pulse ionizes a gas target, ejects many of the electrons out of its path through the ponderomotive force, and drives an electron density wave, or plasma wave, in its wake. The electric field of the plasma wave can accelerate some of the electrons that are injected, by an external source or from the plasma itself, provided that they remain in phase with the wave.

In the last two decades, owing to the development of increasingly intense ultrashort pulses, laser plasma accelerators have generated quasi-monoenergetic electron bunches with low energy spread and low emittance [9–11] reaching to the energies in the GeV range [12], polychromatic bunches of lower quality up to 8 GeV [13], and Gamma rays with MeV range energy [14].

Despite the significant successes of laser wakefield acceleration, depending on the intended application, much more work is needed to improve the electron energy spread, emittance, peak energy, shot to shot stability, energy conversion efficiency, and beam focusability.

Many of the experiments on laser-driven wakefield acceleration are carried out using lasers with very high pulse energies, which are only accessible in large laser

facilities. Such high energy laser pulses are naturally limited to low repetition rates (<10Hz) with current laser technology. However many applications demand higher repetition rate and only require moderate energies.

Laser wakefield acceleration using high repetition rate low energy drive pulses opens the door for multiple applications that do not require accelerated electrons with energies more than a few hundred MeV, an energy range typically necessitating high energy, low repetition rate systems. Proof of concept experiments have already used <10MeV electron beams from laser wakefield acceleration, and the γ rays from Bremsstrahlung conversion of the beams for radiography [15,16]. Lower energy electron bunches, ≤1MeV, can be useful for ultrafast electron diffraction with high temporal resolution [17]. The goal of the research of this dissertation is the generation and optimization of high repetition rate relativistic electron bunches at several MeV energies.

1.2 Dissertation outline

Laser plasma interaction involves complicated evolution of the laser pulse and the plasma. This is especially important for the less explored near-critical plasma density regime, and the broadband laser pulses used for the experiments in this thesis. The rest of this chapter will briefly discuss the basics of intense laser matter interaction and the resulted bandwidth broadening, followed by an introduction to the physics of laser wakefield acceleration. Many of the derivations in this chapter follow those of references [18,19]. In Chapter 2, a detailed description of the experimental

setup is given in addition to a brief introduction to high power ultrashort pulse lasers, generation of few-cycle pulses, and methods used to measure and characterize them.

Lowering the threshold pulse energy required for driving a relativistic plasma wave is done by employing a high density, thin gas jet target. Chapter 3 describes how the use of cryogenically cooled gases leads to the generation of high density targets for laser plasma interaction experiments, and discusses the measurements of gas density and the characterization of clusters (density and average size) formed from isentropic expansion of the gas jet.

In Chapter 4, the kHz repetition rate acceleration of electrons using ~10mJ Ti:sapphire laser pulses and a high density gas target is discussed [20,21] Electron acceleration to ~1MeV range energies at kHz repetition rate from thin, dense gas jet targets was demonstrated for the first time in these experiments, using laser energies as low as ~1mJ. These accelerated electron bunches, however, had a large energy spread and divergence angle. Chapter 5 describes the use of few-cycle laser pulses to improve the energy spread and divergence of the electron beam, leading to quasi-monoenergetic electron bunches up to ~ 5MeV.

Clusters are very interesting targets for laser plasma interaction experiments and the physics of the beam propagation in clusters can be significantly different from unclustered gases. Chapter 6 of this dissertation describes preliminary experiments in the interaction of few-cycle laser pulses with clustered gas jets, where significant self-focusing, energy deposition, and spectral modification of the laser pulses is observed. The dissertation concludes with a short review followed by a brief discussion of future research plans.

1.3 Intense laser matter interaction

1.3.1 Self-focusing

The strong field of a laser pulse is capable of inducing an appreciable, intensity-dependent, refractive index change in a medium as the laser pulse is propagating through it [22]. The physical mechanism responsible for the change in refractive index can be due to an atomic or molecular electronic response, or molecular vibration or rotation. On a much longer timescale, thermal effects can be important [23]. Depending on the physical mechanism responsible for the nonlinear refractive index, the response time can vary from the sub-femtosecond range in case of response to electronic polarization, to the millisecond range for thermal effects [23].

The total refractive index in presence of an intense electromagnetic field, to lowest order in the field, is $n = n_0 + n_2 I(r,t)$, where $n_0$is the linear refractive index at low laser intensity, $I(r,t)$ is the time- and space-dependent intensity of the laser pulse, and n_2 is the nonlinear refractive index, which is related to the 3rd order susceptibility through $n_2 = \frac{3\chi^{(3)}}{4\varepsilon_0 c n_0^2}$. The nonlinear refractive index is usually positive and leads to an increase in the total refractive index [24]. This expression assumes near-instantaneous response of the dipoles (from bound or free electrons) constituting the nonlinear medium.

For the lowest order Gaussian beam, the spatio-temporal intensity dependence at the beam waist is $I(r,t) = I_0(t)\exp\left(-\frac{2r^2}{w_0^2}\right)$, where w_0 is the spot radius ($1/e^2$

intensity), $I_0(t)$ is the intensity envelope, and r is the transverse distance from the beam axis. Near the beam axis ($r \ll w_0$),

$$n(r,t) = n_0 + n_2 I_0(t)(1 - 2r^2/w_0^2) \tag{1.1}$$

leads to a parabolic refractive index, with maximum value on axis.

This radially-dependent index imposes a radially-dependent phase delay and focuses the beam, as would a lens. This effect is called self-focusing, as the effective lens is created by the pulse itself. For a beam with a vacuum wavelength of λ_0 propagating in a medium with nonlinear refractive index n_2, if the peak power of the beam exceeds a critical value [25],

$$P_{cr} \simeq 1.86\lambda_0^2/4\pi n_0 n_2, \tag{1.2}$$

self-focusing can overcome diffraction leading the beam to collapse to a singularity in the absence of other effects that arrest the collapse [26]. Note that in any real system, there is always an arrest mechanism that stops the collapse.

1.3.2 Ionization

The single photon energy in the laser beam used in this thesis (<2eV) is lower than the ionization potential of the atoms (e.g., 13.6eV for hydrogen), so single photon ionization doesn't occur in our experiments. However, as the laser intensity approaches $I \simeq 10^{13} W/cm^2$, other ionization mechanisms such as multiphoton absorption, tunnel ionization, or over-the-barrier ionization can ionize the atoms and molecules.

The relative importance of these mechanisms at different laser intensities and wavelengths is assessed by the Keldysh parameter [27] $\gamma_K = \sqrt{U_i/2U_p}$, where U_i is

the ionization potential of the atom, and $U_p = \frac{e^2E^2}{4m_e\omega^2}$ is the ponderomotive potential energy which is equal to the cycle averaged kinetic energy of an electron in the laser field. In semiclassical terms, γ_K is the ratio of the tunneling time to the laser period.

At low laser intensities and/or high laser frequencies ($\gamma_K \gg 1$) multiphoton ionization (MPI) dominates, where multiple photons are absorbed in one step. At higher intensity ($\gamma_K < 1$) the laser field is strong enough to distort the Coulomb potential significantly so that an electron can tunnel through the distorted potential barrier; this is the tunneling ionization regime. Finally at very high intensities ($\gamma_K \ll 1$) the laser field can suppress the Coulomb potential completely, leading to "over-the-barrier" ionization.

1.3.3 Self-phase modulation

Due to the time dependence of the pulse intensity envelope, the instantaneous refractive index varies through the temporal profile of the pulse. The electronic nonlinearity for both bound and free electrons is nearly instantaneous, where the origin of the bound electronic nonlinearity is atomic potential distortion and the free electron nonlinearity set by the relativistic γ factor. Assuming instantaneous response from the nonlinear medium and a locally near-parallel beam, the total phase shift experienced by the pulse after propagating a distance z in a nonlinear medium is $\phi(z,t) = k(n_0 + n_2 I(t))z - \omega_0 t = \phi_{lin} + kn_2 I(t)z$. Here ω_0 is the center frequency, ϕ_{lin} is the linear phase shift, and $\Delta\phi(z,t) = kn_2 I(t)z$ is the nonlinear phase shift. This leads to an effective modulation in frequency (termed 'self-phase modulation' (SPM)) given by

$$\omega(t) = -\frac{d\phi(z,t)}{dt} = \omega_0 - \frac{\partial \Delta\phi(z,t)}{\partial t} = \omega_0 - kn_2 z \frac{\partial I(t)}{\partial t} \qquad (1.3)$$

This relation shows the addition of new frequency components and an increase in the pulse bandwidth. Increasing intensity($\frac{\partial I(t)}{\partial t} > 0$), such as in the leading portion of the pulse, imposes red shifts, while the trailing section ($\frac{\partial I(t)}{\partial t} < 0$)<0) imposes blue shifts. The propagating pulse can change significantly owing to SPM: (a) material dispersion in the nonlinear medium acting on the newly generated frequencies can impose group velocity dispersion (GVD) and higher order dispersion leading to temporal envelope distortions, and (b) the same process leading to SPM leads to spatial phase front shifts, which can lead to self-focusing and possible filamentation.

For a Gaussian pulse with central frequency ω_0 and pulse length τ_p (FWHM of intensity, $I(t)$) the electric field in the time domain is $E(t) = E_0 \exp\left(-\left(\frac{t}{\tau}\right)^2\right) \exp(-i\omega_0 t)$, where $\tau = \frac{\tau_p}{\sqrt{2\ln 2}}$, and $E_0$is the maximum field amplitude. Accumulation of nonlinear phase modifies the electric field to $E(t) = E_0 \exp(-\left(\frac{t}{\tau}\right)^2) \exp(-i\omega_0 t + ikn_2 I(t)z)$. The spectral intensity of the pulse can then be calculated through the Fourier transform

$$|E(\omega)|^2 = \left|\frac{1}{2\pi}\int_{-\infty}^{\infty} E_0 \exp[-\left(\frac{t}{\tau}\right)^2] \exp[-i\omega_0 t + ikn_2 I(t)z)\, dt\right|^2 \qquad (1.4)$$

Figure 1.2 illustrates the self-phase modulation effect on a short laser pulse, by comparing the electric field, instantaneous frequency, and the power spectrum before and after self-phase modulation. For a Gaussian pulse Eq. 1.3 predicts a

symmetric spectral broadening, which can be approximated by a linear chirp near the peak intensity. Since some newly generated frequency components interfere with frequencies already in the laser bandwidth, the spectrum shows oscillations.

Note that the assumption of instantaneous nonlinear medium response leads to symmetric bandwidth broadening from a symmetric pulse. However, depending on the physical origin of the nonlinearity, there might be a delayed response time. In this situation the leading edge of the pulse could experience a different transient refractive index than the trailing edge, leading to asymmetric spectral broadening [28].

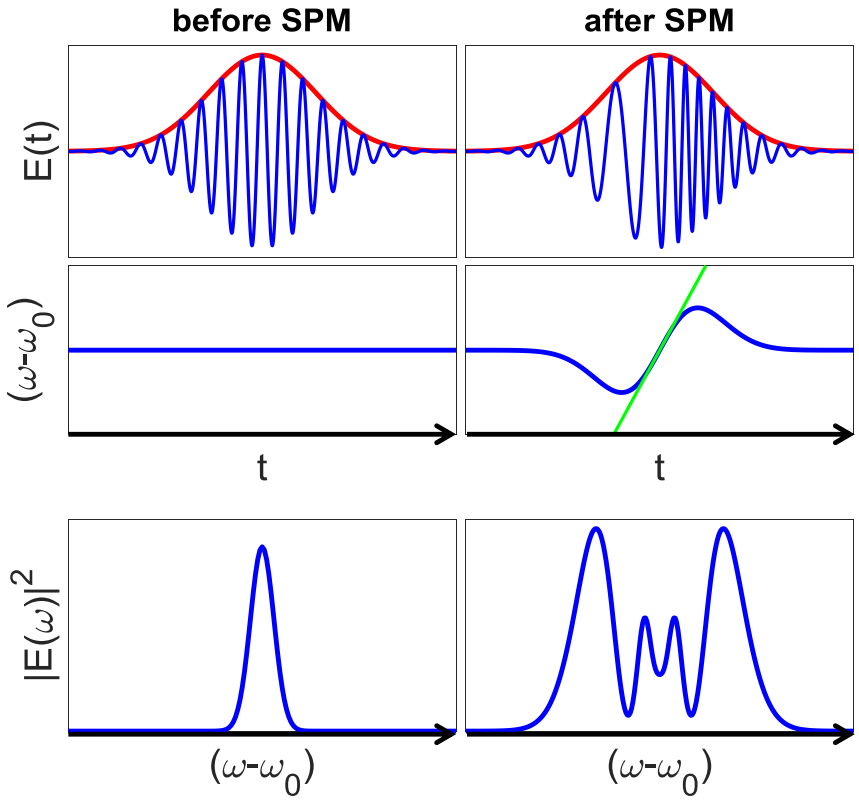

Figure 1.2. Self-phase modulation (SPM) broadens the spectrum of a laser pulse. Before the action of SPM, the pulse carrier frequency is fixed (middle left). After SPM, the bandwidth increases with red frequencies generated at the leading edge and blue frequencies at the trailing edge of the pulse. The frequency increases linearly near the peak of the pulse (green line). Since some newly generated frequency components interfere with frequencies already in the laser bandwidth, the spectrum shows oscillations (bottom right).

Due to the intensity-dependent refractive index, the group velocity at the center of the pulse is lower than at the leading and the trailing edges. This causes pulse steepening at the trailing edge [29] and leads to asymmetric broadening toward blue frequencies.

As the beam intensity increases due to self-focusing, multiphoton ionization and tunneling generate a plasma that reduces the refractive index according to $\Delta n = -\frac{N_e}{2N_{cr}}$, where N_e is the free electron density, and N_{cr} is the critical plasma density. The sudden onset of ionization leads to a quick drop in the refractive index and causes a significant blue shifting of the pulse spectrum through Eq. 1.3: $\Delta\omega(t) = -\frac{\partial\Delta\phi(z,t)}{\partial t} = \frac{\pi n_0}{\lambda_0 N_{cr}}\frac{d}{dt}\int N_e(t)dz$ [30]. Even though this blue shifting can help to increase the bandwidth, when we generate broadband supercontinuum for few-cycle pulses we keep the intensity below the ionization threshold to avoid energy absorption and distortion of the beam profile by plasma.

1.4 Laser wakefield acceleration

1.4.1 Electron motion in an intense electromagnetic field

To understand the motion of a free electron in an electromagnetic field we can start with the relativistic Lorentz force equation [31],

$$\frac{d\mathbf{p}}{dt} = -e(\mathbf{E} + \mathbf{v} \times \mathbf{B}/c) \quad (1.5)$$

where $\mathbf{p} = \gamma m_e \mathbf{v}$ is the electron momentum, written in terms of the electron velocity $\mathbf{v}$, the Lorentz factor $\gamma = (1 - \frac{v^2}{c^2})^{-1/2}$, and the electron mass m_e. The electric and magnetic fields $\mathbf{E}$ and $\mathbf{B}$ can be derived from scalar and vector potentials Φ and $\mathbf{A}$, through $\mathbf{E} = -\nabla\Phi - \frac{1}{c}\frac{\partial \mathbf{A}}{\partial t}$, and $\mathbf{B} = \nabla \times \mathbf{A}$. Using the normalized vector potential $\mathbf{a} = \frac{e\mathbf{A}}{m_e c^2}$, normalized scalar potential $\phi = \frac{e\Phi}{m_e c^2}$, and the normalized momentum $\mathbf{u} = \frac{\gamma \mathbf{v}}{c} = \frac{\mathbf{p}}{m_e c}$, the Lorentz force equation becomes $\frac{1}{c}\frac{d\mathbf{u}}{dt} = \nabla\phi + \frac{1}{c}\frac{\partial \mathbf{a}}{\partial t} - \frac{\mathbf{u}}{\gamma} \times (\nabla \times \mathbf{a})$. This equation can be further simplified using $\frac{1}{c}\frac{d}{dt} = (\frac{1}{c}\frac{\partial}{\partial t} + \frac{\mathbf{u}}{\gamma}.\nabla)$ and rearranging the terms to get

$$\frac{1}{c}\frac{\partial \mathbf{u}}{\partial t} - \frac{1}{c}\frac{\partial \mathbf{a}}{\partial t} + \left(\frac{\mathbf{u}}{\gamma}.\nabla\right)\mathbf{u} = \nabla\phi - \frac{\mathbf{u}}{\gamma} \times (\nabla \times \mathbf{a}) \qquad (1.6)$$

Perturbative expansion of Eq. 1.6 and retention of the leading order normalized momentum term leads to $\mathbf{u}_\perp = \mathbf{a}_\perp$. This term describes the quiver motion of the electron and it is an exact solution in the 1D case, illustrating the conservation of canonical momentum. For the 3D case, and a laser pulse with a sufficiently large spot size $w_0 \gg \lambda$, the quiver motion is still the leading order of electron motion in the transverse direction [18,19].

For the next order term, defining $\delta\mathbf{u} = \mathbf{u} - \mathbf{a}$, using the vector identity $\frac{1}{2}\nabla u^2 = (\mathbf{u}.\nabla)\mathbf{u} + \mathbf{u} \times (\nabla \times \mathbf{u})$ and the Lorentz factor in terms of the normalized momentum, $\gamma = \sqrt{1 + u^2}$, leads to

$$\frac{1}{c}\frac{\partial}{\partial t}(\delta\mathbf{u}) = \nabla(\phi - \gamma) + \frac{\mathbf{u}}{\gamma} \times (\nabla \times \delta\mathbf{u}). \qquad (1.7)$$

The last term on the right hand side of Eq. 1.7 can be neglected assuming electrons have zero momentum before the arrival of the laser pulse [32,33]. The $\nabla\phi$ term is

responsible for space charge force, and the $\nabla\gamma$ terms leads to the nonlinear ponderomotive force $\mathbf{F}_p = -m_e c^2 \nabla\gamma$.

The peak laser intensity can be expressed in terms of the normalized vector potential as

$$a_0 = \sqrt{\frac{2e^2\lambda^2 I_0}{\pi m_e^2 c^5}} \simeq 8.5 \times 10^{-10}\lambda[\mu m]\sqrt{I_0[\frac{W}{cm^2}]} \tag{1.8}$$

where λ is the laser wavelength in μm units, and I_0 is the peak intensity in $\frac{W}{cm^2}$. The normalized vector potential a_0 is the ratio of an electron's cycle average quiver energy to its rest energy, and it is typically used to distinguish between relativistic $a_0 \geq 1$ and nonrelativistic $a_0 < 1$ regimes.

Figure 1.3 depicts the motion of a free electron in an intense plane electromagnetic wave $\mathbf{a} = a_0 \cos(kz - \omega t)\mathbf{e}_x$ for two different values of a_0. The motion in the lab frame consists of a transverse oscillation and a drift with the velocity of $\frac{v_D}{c} = \frac{a_0^2}{4+a_0^2}$ which becomes more important for relativistic intensities [34]. The right panel of Fig. 1.3 shows electron trajectories as seen in a frame moving at two values of v_D (which depends on a_0). If we consider the effect of the temporal profile of the laser pulse on the trajectory, the electron starts from rest, oscillates with increasing amplitude as the laser intensity increases, and eventually comes back to rest once the laser pulse has passed, with no net energy gain [34–36].

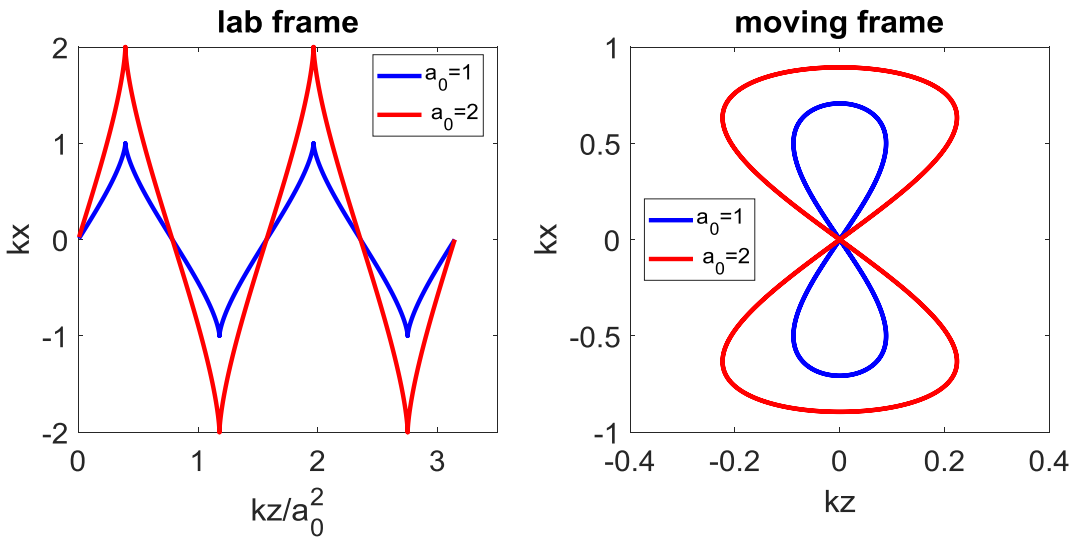

Figure 1.3. Electron motion in a plane wave in the lab frame (left plot) and in frames moving with the drift velocity $\frac{v_D}{c} = \frac{a_0^2}{4+a_0^2}$ along the beam propagation direction (right plot) for two different beam intensities. The laser is linearly polarized along x.

1.4.2 Ponderomotive force and plasma waves

In the linear limit $(a \ll 1)$ the ponderomotive force can be written in the form $\mathbf{F}_p = -m_e c^2 \nabla \left(\frac{a^2}{2}\right)$. In the 3D case with the finite transverse extent of the pulse, the transverse gradient of the intensity ejects plasma electrons from the focal region. Figure 1.4 compares the motion of electrons starting at different transverse distances from the beam axis. The intensity gradient near the beam axis is smaller compared to the regions near the intensity FWHM, reducing the ponderomotive drift there, while those electrons very close to the beam axis experience larger laser fields. These electrons undergo a higher amplitude quiver motion superimposed on a $\mathbf{E} \times \mathbf{B}$ drift, and persist longer in front of the pulse [37,38].

The direction of the ponderomotive force is the same for electrons and ions, always away from the higher intensity sections of the beam. However, the

ponderomotive force is inversely proportional to the particle mass (note the mass factor in $\mathbf{a} = \frac{e\mathbf{A}}{m_e c^2}$), making the acceleration proportional to the inverse square of the particle mass. Since the ions are much more massive than electrons, e.g., for the proton, $\frac{M_p}{m_e} \sim 1836$, ion acceleration from the ponderomotive force is ignorable.

In a plasma, as the electrons are pushed out of the high laser intensity region due to the ponderomotive force, the $\nabla\phi$ term in Eq. 1.7 comes into play by pulling the electrons back and making them oscillate back and forth through the positive region left behind the laser pulse.

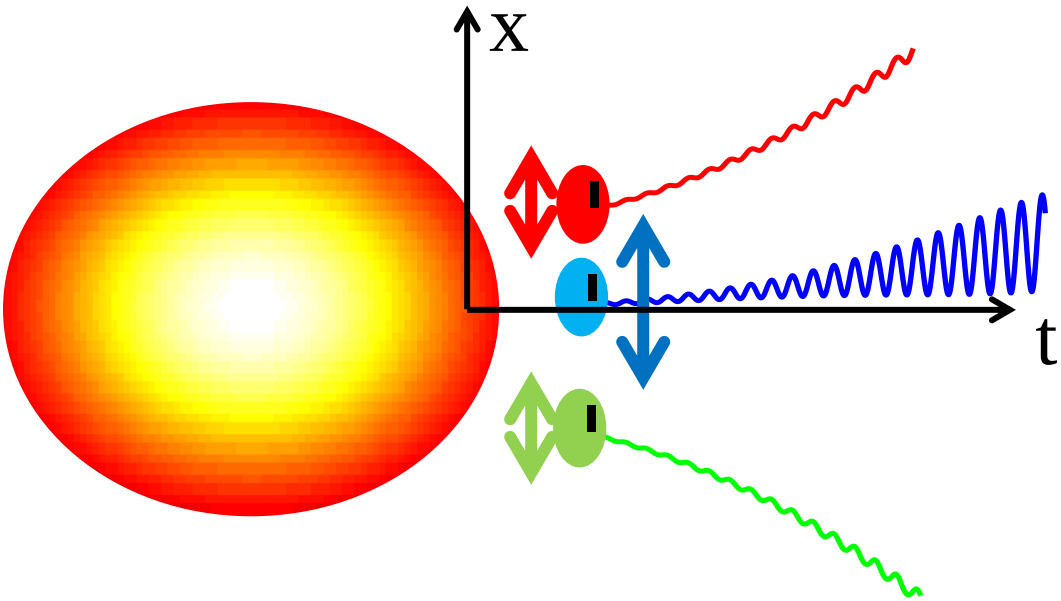

Figure 1.4. Electron trajectory along polarization direction (x). The fast oscillation is the quiver motion at the driver frequency, and the drift is due to ponderomotive force ejecting electrons out of the focal region. The electrons very close to the beam axis experience less intensity gradient, gain $\mathbf{E} \times \mathbf{B}$ drift and persist longer in front of the pulse. The sharp cusps of the trajectory are not shown here.

The plasma frequency,

$$\omega_p = \sqrt{\frac{4\pi N e^2}{m_e}} \tag{1.9}$$

describes the collective oscillation of electrons in response to perturbations in an initially neutral plasma, where N is the electron number density. We can also define a plasma frequency for ions $\omega_{pi} = \sqrt{\frac{4\pi N_i q^2}{M}}$, where N_i is the number density, and q and M are the ion's charge and mass. Given the much heavier mass of ions compared to the electrons, they have much smaller plasma frequency, making their response time much slower compared to electrons. Thus, we will ignore the motion of the ions throughout this dissertation

Using relativistic cold fluid equations for plasma, the normalized wave equation can be written $\left(\nabla^2 - \frac{1}{c^2}\frac{\partial^2}{\partial t^2}\right)\mathbf{a} = k_p^2 \frac{N}{\gamma N_0}\mathbf{u} + \frac{1}{c}\frac{\partial}{\partial t}\nabla\phi$ [33], where N_0 is the ambient electron number density, and $k_p = \frac{\omega_p}{c}$. From the second order terms of Eq. 1.7 we have

$$\frac{1}{c}\frac{\partial}{\partial t}(\delta\mathbf{u}) = \nabla\phi - \nabla(a^2/2). \tag{1.10}$$

These equations along with the continuity equation can be used to derive an equation for the plasma waves in the linear regime ($a \ll 1$).

Keeping the first order terms of the continuity equation, $\frac{\partial N}{\partial t} + \nabla.(\mathbf{v}N) = 0$, gives $\frac{\partial}{\partial t}\frac{\delta N}{N_0} + c\nabla.(\delta\mathbf{u}) = 0$. Taking the time derivative and substituting Eq. 1.10 instead of the second term the continuity equation becomes

$$\frac{\partial}{\partial t}\left(\frac{\partial}{\partial t}\frac{\delta N}{N_0} + c\nabla.(\delta\mathbf{u})\right) = \frac{\partial^2}{\partial t^2}\frac{\delta N}{N_0} + c^2\nabla.\left(\nabla\phi - \nabla\left(\frac{a^2}{2}\right)\right). \tag{1.11}$$

Using the normalized density perturbation $\frac{\delta N}{N_0} = \frac{N}{N_0} - 1$, Poisson's equation $\nabla^2\phi = k_p^2\left(\frac{N}{N_0} - 1\right)$ can be written as $\nabla^2\phi = k_p^2\frac{\delta N}{N_0} = \frac{\omega_p^2}{c^2}\frac{\delta N}{N_0}$, which is used to simplify Eq. 1.11 to

$$\left(\frac{\partial^2}{\partial t^2} + \omega_p^2\right)\frac{\delta N}{N_0} = c^2\nabla^2\left(\frac{a^2}{2}\right). \tag{1.12}$$

Similar calculations give $\left(\frac{\partial^2}{\partial t^2} + \omega_p^2\right)\phi = \omega_p^2\left(\frac{a^2}{2}\right)$, which along with Eq. 1.12 describe the plasma wave generated in an initially uniform plasma in the linear regime ($a \ll 1$). Solving these equations results in [18,19]

$$\frac{\delta N}{N_0} = \frac{c^2}{\omega_p}\int_0^t dt' \sin[\omega_p(t-t')]\nabla^2 a^2(\mathbf{r}, t')/2 \tag{1.13}$$

for the density wave when the perturbation $|\frac{\delta n}{n_0}| \ll 1$, and

$$\frac{\mathbf{E}}{E_0} = -c\int_0^t dt' \sin[\omega_p(t-t')]\ \nabla\ a^2(\mathbf{r}, t')/2 \tag{1.14}$$

for the plasma electric field, where $E_0 = \frac{m_e c\omega_p}{e}$, is the nonrelativistic wavebreaking field [39]. These equations indicate that wakefield generation is most efficient when the laser envelope scale length is in order of plasma wavelength $\lambda_p = \frac{2\pi c}{\omega_p}$.

In the linear regime, $\mathbf{E} \ll E_0$, the solution for the plasma wave is a sinusoidal oscillation with the plasma frequency ω_p. The phase velocity of the plasma wave is given by $v_p \simeq v_g$ where $v_g = c\sqrt{1 - \omega_p^2/\omega^2}$ is the group velocity of the driver laser pulse.

Nonlinear wakefield generation in 1D can be studied in the quasi-static approximation, where the drive laser beam and the plasma fluid quantities are considered to only depend on $\xi = z - v_p t$, in a frame defined by independent

variables ξ and $\tau = t$ [40,41]. Under the quasi-static approximation, the operator $\frac{\partial}{\partial \tau}$ is ignored in the fluid momentum and continuity equations. Integrating these equations gives three constants of motion $\mathbf{u}_\perp = \mathbf{a}_\perp$, $N(1-\beta) = N_0$, and $\gamma(1-\beta) - \phi = 1$, which along with the Poisson equation, $\frac{\partial^2 \phi}{\partial \xi^2} = k_p^2 \left(\frac{N}{N_0} - 1\right)$, lead to

$$k_p^{-2} \frac{\partial^2 \phi}{\partial \xi^2} = \gamma_p^2 \left\{ \beta_p \left[1 - \frac{\gamma_\perp^2}{\gamma_p^2 (1+\phi)^2} \right]^{-1/2} - 1 \right\}. \tag{1.15}$$

Here $\gamma_\perp^2 = 1 + \mathrm{u}_\perp^2 = 1 + a^2$, $\gamma_p = (1 - \beta_p^2)^{-1/2}$, and $\beta_p = v_p/c$. In the $\gamma_p \gg 1$ limit, Eq. 1.15 can be simplified to $k_p^{-2} \frac{\partial^2 \phi}{\partial \xi^2} = \frac{1+a^2}{2(1+\phi)^2} - \frac{1}{2}$ [42].

The axial electric field is found using $E_z = -\frac{E_0 \partial \phi}{\partial \xi}$, and the simplified equations for the plasma fluid density, momentum and the Lorentz factor for $\gamma_p \gg 1$ are as follows [18]

$$\frac{N}{N_0} = \frac{\gamma_\perp^2 + (1+\phi)^2}{2(1+\phi)^2} \quad (a)$$

$$u_z = \frac{\gamma_\perp^2 - (1+\phi)^2}{2(1+\phi)^2} \quad (b) \tag{1.16}$$

$$\gamma = \frac{\gamma_\perp^2 + (1+\phi)^2}{2(1+\phi)} \quad (c)$$

Figure 1.5 compares the wakefield for a linearly polarized Gaussian pulse $a(\zeta) = a_0 \exp(-\zeta^2/4L_{rms}^2)\cos(k\zeta)$, with $\zeta = z - ct$, and $k_p L_{rms} = 1$, at the mildly relativistic case of $a_0 = 0.5$, and the more relativistic case of $a_0 = 2$. For $a_0 = 0.5$, the normalized density perturbation and the normalized axial electric field are both sinusoidal, oscillating at the plasma frequency. In the highly nonlinear regime case of $a_0 = 2$, the electric field is no longer a simple sinusoid and has a sawtooth

profile, the density oscillations become highly peaked, and the period of nonlinear plasma oscillations increases to $\lambda_{Np} \simeq \frac{2}{\pi}\frac{E_{\max}}{E_0}\lambda_p$, where $E_{\max}$is the peak electric field of the plasma wave [18].

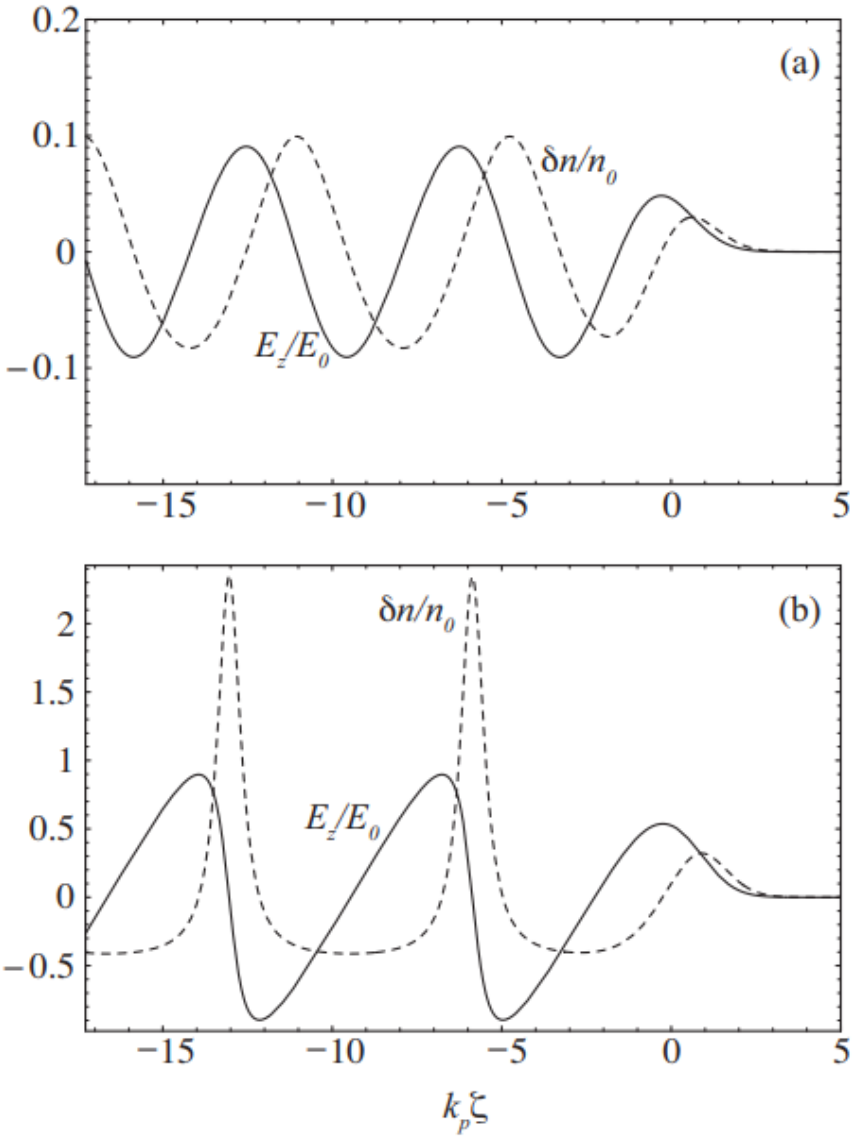

Figure 1.5. Comparison of time averaged density variations (dashed curve) and the axial electric field (solid curve) in a wakefield driven by a Gaussian pulse $a(\zeta) = a_0\exp(-\zeta^2/4L_{rms}^2)\cos(k\zeta)$ with $k_pL_{rms} = 1$ for (a) mildly relativistic $a_0 = 0.5$, and (b) highly relativistic $a_0 = 2$ regime. Figure is taken from Reference [18].

These analytic solutions and approximations only work for the 1D case and the linear 3D case. Best understanding of the 3D nonlinear regime ($a_0 > 1$) is achieved using particle-in-cell (PIC) simulations [43,44]. In these simulations, the fields and particles are defined for a discrete grid using a Yee lattice [45]. At each time step, the updated fields get calculated from the particle positions and in turn, the updated particle positions are calculated from the force applied to them by the fields, using a leapfrog method. The experiments carried out in this thesis are performed in near critical plasma density where a sharply focused broadband laser pulse experiences a very complex evolution. The complicated dynamics originating from the nonlinear 3D nature of the experiments makes it impossible to analyze the interaction without the help of extensive simulations. We have performed 2D and 3D simulations using the PIC codes TurboWAVE [46] and EPOCH [47] for a better understanding of the laser plasma interaction in our experiments.

1.4.3 Wavebreaking and dephasing

Plasma can sustain large amplitude electron density waves with phase velocities near the speed of light. In the linear regime, the electric field of the plasma wave can be written as $E_z = E_{\max}\sin\left[\omega_p\left(\frac{z}{v_p} - t\right)\right]$. Assuming all electrons oscillate at the plasma frequency and using the Poisson equation $\nabla.\mathbf{E} = 4\pi e(N_0 - N_e)$, the maximum field amplitude $E_{\max}$ is estimated to be $\left(\frac{\omega_p}{c}\right)E_{\max} = 4\pi e N_0$, giving $E_{\max} = E_0 = \frac{m_e c\omega_p}{e}$. This value of E_0 is the cold nonrelativistic wavebreaking

field. The amplitude of a nonlinear plasma wave, however, can exceed E_0. Using 1D nonlinear cold fluid equations, the cold relativistic wavebreaking field is [48]

$$E_{WB} = \sqrt{2}(\gamma_p - 1)^{1/2} E_0, \tag{1.17}$$

where $\gamma_p$is the Lorentz factor for the phase velocity of the plasma wave.

As the velocity of an accelerating electron approaches the speed of the light, it can outrun the plasma wave, which has a phase velocity close to the group velocity of the driver pulse and enters the decelerating region of the plasma wave. So there is a limit for the energy gain of an electron in the plasma wave. The distance that the electron must travel before it moves from an accelerating to decelerating phase of the plasma wave is called the dephasing length L_d.

In the linear regime, assuming the electron velocity is $v_z \simeq c$ leads to $L_d(1 - v_p/c) = \lambda_p/2$, giving $L_d = \gamma_p^2 \lambda_p$ for $\gamma_p \gg 1$. The maximum energy gain is estimated as $W_{\max} = eE_{\max} L_d = eE_{\max} \gamma_p^2 \lambda_p = 2\pi\gamma_p^2 \left(\frac{E_{\max}}{E_0}\right) m_e c^2$.

1.4.4 Beam propagation in plasma

Using the plasma dispersion relation $\omega^2 = c^2 k^2 + \omega_p^2$ the plasma refractive index is $n = (1 - \omega_p^2/\omega^2)^{1/2}$. The relativistic mass- and electron density-dependent plasma frequency is $\omega_p^2 = \frac{\omega_{p0}^2}{\gamma}\left(\frac{N}{N_0}\right)$ [49]. For plasmas well below the critical density, $\frac{\omega_p^2}{\omega^2} \ll 1$ we can expand the refractive index relation to get $n \cong 1 - \frac{\omega_p^2}{2\omega^2}\frac{N}{N_0\gamma}$ [40]. Keeping only the quiver motion in calculating the relativistic factor $\gamma = (1 + \mathbf{a}^2)^{1/2}$, and writing the electron density profile as $N = N_0 + \Delta N_p + \delta N$, where $\Delta N_p$is the

contribution from a preformed density channel and δN is the plasma wave contribution, the refractive index can be written for $a^2 \ll 1$ as

$$n = \left(1 - \frac{1}{2}\frac{\omega_{p0}^2}{\omega^2}\left(1 - \frac{\mathbf{a}^2}{2} + \frac{\Delta N_p}{N_0} + \frac{\delta N}{N_0}\right)\right). \quad (1.18)$$

Here, the $\frac{\Delta N_p}{N_0}$ term is responsible for beam propagation in preformed density channel, $\frac{a^2}{2}$ represents the relativistic guiding, and $\frac{\delta N}{N_0}$ is responsible for self-modulation of long laser pulses. For broadband few-cycle pulses, as we will discuss in Chapter 5, a new term ($\frac{\omega_p^2}{\omega^2}(\frac{\delta\omega}{\omega})$) is added to Eq. 1.18 to model dispersion, and changes the refractive index to $n = \left(1 - \frac{1}{2}\frac{\omega_{p0}^2}{\omega^2}\left(1 - \frac{\mathbf{a}^2}{2} + \frac{\Delta N_p}{N_0} + \frac{\delta N}{N_0} - 2\frac{\delta\omega}{\omega}\right)\right)$ [50]. For typical experiments, this term is small compared to other terms in Equation 1.18 and it can be neglected.

Ignoring the effect of spatially varying density, we have $n = 1 - \frac{1}{2}\frac{\omega_{p0}^2}{\omega^2}(1 - \frac{a^2}{2})$; this relation has the form of $n = n_0 + n_2 I$ which resembles the Kerr index in self-focusing discussed earlier in this chapter. The intensity is higher at the center of the beam and produces a refractive index profile which peaks at beam center, enabling focusing of the laser beam [49].

For a Gaussian beam, the evolution of the spot size under the effects of diffraction and relativistic self-focusing is characterized through [18]

$$\frac{d^2R}{dz^2} = \frac{1}{Z_R^2 R^3}\left(1 - \frac{P}{P_{cr}}\right) \quad (1.19)$$

Here $R = \frac{w}{w_0}$ is the normalized spot size, $w_0$is the vacuum spot radius, $Z_R = \frac{\pi w_0^2}{\lambda}$ is the vacuum Rayleigh length, and P_{cr} is the critical power for relativistic self-focusing

$$P_{cr} = 2c(\frac{m_e c^2}{e})^2 \frac{\omega^2}{\omega_{p0}^2} \simeq 17.4 \frac{\omega^2}{\omega_{p0}^2}(GW). \quad (1.20)$$

Solving Equation 1.19 for the beam size, when the waist is at $z = 0$, leads to $R^2 = 1 + \frac{\left(1-\frac{P}{P_{cr}}\right)z^2}{Z_R^2}$; when $P > P_{cr}$ the formula suggests self-focusing [18,19]. The ponderomotive force can lower the on axis electron density and enhance the effect of relativistic self-focusing, but it doesn't change the threshold critical power for self-focusing significantly [51].

The density compression in front of the pulse acts against the effect of the relativistic increase of mass in modifying the refractive index. As a result, relativistic self-focusing doesn't happen for a length of $\sim\lambda_p$ in front of the pulse, and this portion of the pulse gets eroded due to diffraction [40,41]. When the laser pulse is significantly shorter than the plasma wavelength $c\tau_L \ll \lambda_p$, and $P \gg P_{cr}$, the leading edge of the pulse gets depleted before it diffracts [52].

1.4.5 Self-modulation instability

We first consider a laser pulse satisfying $c\tau_L \gg \lambda_p$. In order to understand the effect of the $\frac{\delta N}{N_0}$ term in the refractive index, we consider a plasma wave $\delta N = \delta N_m \sin(k_p \zeta)$, where δN_m is the amplitude of the plasma wave density oscillations. The plasma wave enhances trapping in low density regions (local density channels) and beam spreading in high density regions; the laser pulse envelope gets longitudinally modulated at $\lambda_p = 2\pi/k_p$, the plasma wavelength. The modulated

laser pulse resonantly excites the wakefield and the process grows as a stimulated Raman instability, resulting in a series of laser pulselets of length $\lambda_p/2$ [33,53].

In the self-modulated regime, the accelerated electron bunches have a broad energy spread because the electrons injected into the plasma wave are launched with a range of phases and velocities through continuous trapping, and are repeatedly accelerated and decelerated owing to the short dephasing length. The experiments described in Chapter 4 of the dissertation are carried out in the self-modulated regime.

1.4.6 Resonant regime

Maximum plasma wave amplitude is achieved when the laser pulse drives the plasma resonantly. For long pulses $c\tau_L \gg \lambda_p$, the resonance can be achieved by beating two laser beams [54] to generate a beat wave with plasma frequency, or by using self-modulation instability to modulate the amplitude of the laser pulse with the period $\tau \simeq 2\pi c/\omega_p$ [55]. A short laser pulse drives the plasma resonantly if the pulse has the same length scale as the plasma wavelength $c\tau_L \sim \lambda_p$ [56].

For a very high intensity laser pulse, the ponderomotive force can expel all of the plasma electrons out of its path, forming an ion cavity. This regime is called the bubble or blow out regime [57]. We discussed earlier, based on a weakly relativistic analytic model, that relativistic self-focusing is not effective for laser pulses with $c\tau_L \ll \lambda_p$ owing to the density compression at the leading edge of the pulse [40,41]

For high intensities $a_0 > 1$ weakly relativistic analytic expressions are not appropriate and the wakefield, which now must be modeled in 3D, is studied

numerically. However, balancing the electrostatic force from an electron-evacuated spherical cavity of radius R, formed by the pulse (bubble) ($\sim k_pR$), and the ponderomotive force ($\frac{k_p\nabla a_0^2}{\gamma} \sim \frac{a_0}{k_pR}$), leads to an approximation for the bubble radius $k_pR \sim \sqrt{a_0}$. Results of 3D PIC simulations give the commonly used expression [52]

$$k_pR \simeq k_pw_0 = 2\sqrt{a_0} \tag{1.21}$$

If the laser pulse is short enough that its intensity is negligible toward the backside of the bubble, the axial electric field from the plasma wake can be found by assuming a spherical electron cavity moving at the laser pulse velocity. For $R^2 = r^2 + \xi^2$, where r and ξ are the transverse and longitudinal (moving frame) dimensions, the fields inside the cavity are [57,58]

$$E_z = \left(\frac{k_p\xi}{2}\right)E_0 \quad (a)$$

$$E_r = \left(\frac{k_pr}{4}\right)E_0 \quad (b) \tag{1.22}$$

$$B_\theta = -\left(\frac{k_pr}{4}\right)E_0 \quad (c)$$

The maximum amplitude of the axial electric field $E_{\max} = (k_pR/2)E_0 = \sqrt{a_0}E_0$, occurs at the back side of the bubble and it drops linearly as the center of the bubble is approached. Using this electric field in nonlinear plasma wavelength formula for 1D case $\lambda_{Np} \simeq \frac{2}{\pi}\frac{E_{\max}}{E_0}\lambda_p = \frac{2\sqrt{a_0}}{\pi}\lambda_p$shows that the bubble diameter is almost equal to the plasma wavelength in the nonlinear 1D regime [18].

Figure 1.6 shows simulation results illustrating the shape of the cavity (bubble) formed in the wake a short laser pulse, and a lineout of the normalized

electric field along the propagation axis. The electron beam is injected near the end of the bubble and gets accelerated as the laser pulse propagates further in the plasma.

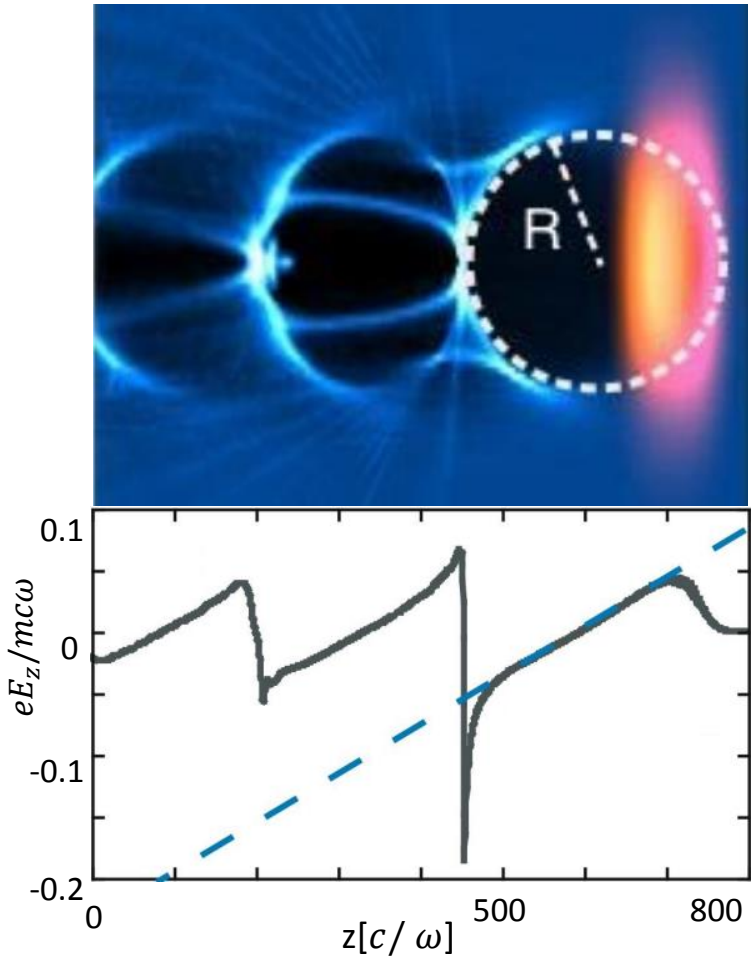

Figure 1.6. Simulation result showing (top) the cavity formed in wake of a short laser pulse and (b) a lineout of the normalized electric field along the propagation axis. The slope of the field is nearly constant. Figure is taken from Reference [52] and modified.

The radial electric field E_r, and the azimuthal magnetic field B_θ, apply a radial focusing force on off-axis electrons, making them undergo transverse betatron oscillations [59]. The experiments at Chapter 5 of the dissertation use the few-cycle laser pulses to operate in the bubble regime in near-critical plasma densities.

1.4.7 Electron injection

In order for an electron to be trapped and accelerated in the plasma wave, its initial axial velocity should be at least equal to the phase velocity of the plasma wave, $v_z \gtrsim v_p$; otherwise, it will slip backward through the plasma wave and it will not be accelerated [18].

For cold plasmas in 1D, the injection condition for plasma background electrons is for the wakefield amplitude to reach the wavebreaking threshold. Thermal effects and other effects associated with higher dimensions such as transverse wavebreaking due to the increase in wake front curvature [60] can lower this threshold. In self modulated LWFA at higher plasma densities, the lower phase velocity of the plasma wave ensures that a large amount of charge can be injected; however, as discussed earlier, due to the short dephasing length and continuous trapping the accelerated electron bunches have a broad energy spread.

Self-injection of the background electrons can also occur in the bubble regime [61]. Continuous bubble expansion causes continuous injection of the electrons into the wake and limits the energy spectrum quality in this case [62].

A downward density transition (‘density downramp’) in an inhomogeneous plasma, can cause electron self-trapping in the plasma wave [63]. The decrease in plasma density increases λ_p and increases the laser group velocity. The local phase velocity of the plasma wake decreases in the density transition and leads to local trapping of electrons in the wake at the point where the electron velocity is equal to the local phase velocity.

Another method for injecting electrons in the wave is ionization injection [64,65]. Helium or hydrogen gas targets can be locally fully ionized by laser pulses with peak intensities $\sim 10^{16} \frac{W}{cm^2}$, which can be achieved at the leading edge of the much more intense pulses used in LWFA experiments. On the other hand, liberating the inner shell electrons of gases like nitrogen or argon requires much higher intensity. In the ionization injection regime, the inner shell electrons of high atomic number gases are liberated inside the wake once the high amplitude electric field of the wake is formed; these electrons are then injected in the wake. This injection process is continuous through the wake so that electrons can be injected into a range of phases of the plasma wave; thus this injection mechanism is also limited by excessive energy spread in accelerated bunches.

For both of the acceleration regimes of this dissertation, self-modulated and bubble regimes, hydrogen and helium gas targets are mainly used and wavebreaking is the dominant injection mechanism. In the case of a nitrogen gas jet, we observe wavebreaking and ionization injection acting simultaneously.

Chapter 2: Laser systems

2.1 Introduction to high power lasers

2.1.1 Chirped Pulse Amplification

The peak power of laser pulses has increased many orders of magnitude since the invention of lasers. This increase in peak power is owed to the invention of methods for generating ever shorter pulses and amplifying them. Techniques such as Q-switching and mode-locking [66], invented not very long after laser itself, have lowered the pulse duration from the microsecond range down to a few femtoseconds. Recent techniques have led to the generation of pulses in the attosecond regime [67].

Another invention that has led to a significant increase in peak pulse power is Chirped Pulse Amplification (CPA) [68]. Before the invention of CPA, the accumulation of nonlinear phase $B = \frac{2\pi}{\lambda}\int_0^L n_2 I dx$, and subsequent self-focusing filamentation and damage in the gain medium, had limited the maximum achievable power density to the $\sim 1\ GW\ cm^{-2}$ range [69]. In the CPA technique, the initial pulse from the mode-locked laser oscillator is stretched in time by a factor of ~10^4; this lowers the intensity, keeping $B \ll 1$ as the stretched oscillator pulse is amplified in the amplifier laser rods. After amplification, the pulse is compressed back to its initial duration. CPA will be discussed in more detail in this chapter after a short introduction to spectral phase and dispersion manipulation in high power lasers.

2.1.2 Spectral phase and dispersion

The spectral phase of a pulse $\phi(\omega)$ can be expanded around its central frequency $\omega_0$in a Taylor series as

$$\phi(\omega) = \phi_0 + \phi_1(\omega - \omega_0) + \frac{\phi_2(\omega - \omega_0)}{2} \ldots. \quad (2.1)$$

where $\phi_1 = \partial\phi/\partial\omega|_{\omega_0}$, is the group delay and $\phi_2 = \partial^2\phi/\partial\omega^2|_{\omega_0}$, is the group delay dispersion (GDD). As the pulse propagates a distance L in the medium its phase shift is

$$\Delta\phi(\omega) = k(\omega)L = k(\omega_0)L + k'(\omega_0)(\omega - \omega_0) + \frac{1}{2}k"(\omega_0)(\omega - \omega_0)^2L + \ldots \quad (2.2)$$

Here, $v_p(\omega_0) = \omega_0/k(\omega_0)$ is the phase velocity, $k'(\omega_0) = 1/v_g(\omega_0)$ is the group delay per unit length, and $k"(\omega_0) = \frac{d}{d\omega}(\frac{1}{v_g})$ is the group velocity dispersion (GVD). The shortest pulse duration is achieved when the spectral phase terms of the 2nd and higher orders are zero. GDD is the lowest order term manipulated for stretching or compressing the pulse. Higher order terms ($\phi_3$etc.) can distort the pulse shape and add wings to it, and they should be compensated for in order to generate transform limited pulses.

For a Gaussian pulse, the electric field in the time domain can be written as $E(t) = E_0\exp\left(-\frac{t^2}{\tau^2}\right)\exp(-i\phi(t))$, where $\tau = \tau_p/\sqrt{2\ln 2}$, τ_p is the pulse FWHM, and $\phi(t)$ is the temporal phase of the pulse. By expanding $\phi(t)$ up to second order (lowest order effecting the pulse duration), the electric field is rewritten as $E(t) = E_0\exp\left(-\frac{t^2}{\tau^2}\right)\exp\left(i\left(\omega_0 t + \frac{bt^2}{\tau^2}\right)\right)$, where b is the chirp parameter. The

effective instantaneous frequency, in this case, is given by $\omega(t) = -\frac{d\phi(t)}{dt} = \omega_0 + 2bt/\tau^2$, showing a linear frequency chirp in time. For $b = 0$ the pulse is transform limited. It is positively chirped for $b > 0$ and negatively chirped for $b < 0$.

The Fourier transform of a chirped Gaussian function, here the above representation for $E(t)$, is also a Gaussian function. Fourier transform of $E(t)$ gives

$$\tilde{E}(\omega) = \tilde{E}_0 \exp\left(-\frac{\tau^2}{4(b^2+1)}(\omega-\omega_0)^2\right)\exp\left(-i\frac{b\tau^2}{4(b^2+1)}(\omega-\omega_0)^2\right) \quad (2.3)$$

where $\tilde{E}_0$ is the field amplitude at the spectral peak. The time-bandwidth product for this chirped pulse is given by $\Delta t \Delta\omega/2\pi \geq 0.44\sqrt{1+b^2}$, which is a factor of $\sqrt{1+b^2}$ larger than the transform limited pulse [70] as the linear chirp due to GDD increases the pulse duration.

The spectral phase shift due to propagation in a medium changes the pulse shape and duration. Noting that the GDD from most materials is positive for visible and near-IR wavelengths ($\lambda \sim 0.4 - 1.4\mu m$), the wavelength range for most lasers used in laser-driven accelerators, one can use this dependence to temporally stretch transform limited or positively chirped pulses, or compress negatively chirped pulses.

Imposing effective GDD<0 using materials with intrinsic GDD>0 is accomplished by angularly dispersing the pulse using prisms or diffraction gratings. In either case, the dispersive element should be used in pairs to re-collimate the beam after adding negative GDD. In the case of a prism pair, total GDD is given by [71] $GDD = \phi_2 = \frac{\lambda^3}{2\pi c^2}\left(L_p\frac{d^2n}{d\lambda^2} - 4L_s\left(\frac{dn}{d\lambda}\right)^2\right)$, where L_s is the distance between the two prisms, and L_p is the path length inside the prism. The positive GDD term is due to

propagation inside the prism while the negative GDD term comes from angular dispersion, and is proportional to the separation of the prisms [71,72].

Using a pair of parallel diffraction gratings is the most common method for compressing of high power beams. Typically, gratings yield more compression than prism pairs and avoid accumulating nonlinear phase due to high power beam propagation in solid material. The GDD, in this case, is $GDD = \phi_2 = -\frac{\lambda^3}{2\pi c^2 d^2 cos^2\theta} L_s$, where d is the grating groove spacing, θ is the angle of incidence with respect to the grating normal, and L_s is the distance between the two gratings. Similar to the case of the prism pair, the GDD is proportional to the separation of the grating pair [73–75].

For more effective pulse compression (especially for broader bandwidths) one should consider higher order spectral phase too. The sum of the spectral phase introduced by the stretcher, amplifiers, and the compressor should be zero for best compression (i.e.,$\phi_{2_{stretcher}} + \phi_{2_{amplifier}} + \phi_{2_{compressor}} = 0$, and same for ϕ_3, ϕ_4 ...). The 2nd order phase is compensated by adjusting the separation of prisms or grating pairs as discussed above. However, the 3rd and higher order phase can add wings to the pulse and distort its shape. The introduce 3rd order spectral phase for grating and prism pairs have opposite signs, so schemes using both prisms and gratings in a compressor can lead to 3rd order phase compensation, generating shorter pulses [76]. Adjusting the beam incident angle on the compressor grating pair and inserting a specific length of optical material (e.g., glass) in the beam path, it is possible to compensate for up to the 4th order phase [77].

Another method for introducing negative GDD is using chirped mirrors where different wavelengths in a beam penetrate different depths into the mirror layers before reflection. A simple chirped mirror [78], can consist of ~50 alternating layers of SiO_2 (with refractive index $n = 1.45$) and TiO_2 with ($n = 2.3$) with quarter wavelength optical thickness. Having higher layer thickness near the substrate, and lower thickness at the air-coating interface leads to larger group delay from larger wavelengths and hence negative GDD.

Simple designs with a linear chirp in layer thickness typically lead to strong oscillations in group delay and GDD. In newer designs, double angle dispersed mirror pairs have the GDD oscillation versus spectrum shifted properly for two specific incidence angles such that the oscillations cancel each other out, resulting in a constant GDD across the spectrum [79].

The negative GDD due to the anomalous dispersion of some crystals at mid-IR wavelengths ($\lambda \sim 3 - 8\mu m$) [80,81], as well as in plasma for all frequencies below plasma frequency [82] can also be used for pulse compression, but maintaining a good beam quality in the latter case can be challenging.

2.2 Titanium doped Sapphire (Ti:Sapphire) laser

The laser gain medium Titanium-doped Sapphire ($Ti: Al_2O_3$, Ti:Sapphire) has a very large gain bandwidth covering the spectral range from 650nm to 1100nm, high thermal conductivity, and high saturation power, making it especially useful for high peak power, short pulse laser systems. Ti:Sapphire is the dominant gain medium used for modern ultrashort pulse laser systems, and has replaced prior gain media such as

dyes and Nd:glass rapidly after its introduction [83]. Nd:glass is still used in very high energy laser systems [84]

Due to the large the nonlinear refractive index of Ti:Sapphire, Kerr lensing is typically used for mode-locking of Ti:Sapphire oscillators. This technique [85] takes advantage of nonlinear self-focusing in the gain medium. Oscillators are designed such that pulses nonlinearly lensed in the Ti:Sapphire crystal (which are the shortest pulses) experience the lowest cavity losses [86]. Figure 2.1 (a) illustrates Kerr lens mode-locking in a laser cavity. The highest intensity (shortest) pulse has better overlap with the pump spot on the gain crystal and experiences higher gain and less loss per round trip than lower intensity pulses. This process grows from noise, where shorter noise spikes (comprising more of the medium bandwidth) begin to be dominantly amplified. After a few round trips, only the shortest pulse survives the losses and forms the mode locked pulse train.

A typical design for a high power Ti:Sapphire laser includes an oscillator, a stretcher, a regenerative amplifier, multipass amplifiers, and a compressor. Panels (b) and (c) of Fig. 2.1 depict the CPA steps. In the first step, a pulse from the oscillator is stretched in a grating stretcher. In the stretcher, longer wavelengths (red colors) have less delay than shorter wavelengths (blue colors), producing GDD>0. Sending the beam through dispersive material with spherical aberration in the stretcher leads to higher order spectral phase and in turn poor pulse compression [75]. Modern stretchers reduce the aberrations, and higher order dispersion, by use of concave mirrors instead of the spherical lenses, and use a single grating in a more compact design. After the stretcher, the pulse is sent to a sequence of amplifiers which increase

its energy by a factor of ~ 10^6 -10^8 (for the various CPA-based lasers in our lab), followed by the final step of compression to approximately its initial duration. The grating compressor imposes a negative GDD: the longer wavelength rays have a greater path length than the shorter wavelength rays. The optimal separation distance L_s of the gratings is set to compensate for 2nd order phase imposed by the stretcher and amplifiers; by fine tuning L_s one can get positively or negatively chirped pulses.

The Ti:Sapphire laser used for most of the experiments described in this thesis starts with a Kerr lens mode-locked oscillator (Coherent Vitara) generating pulses with ~65nm bandwidth, corresponding to ~15fs transform limited duration. The pulse energy out of the oscillator is ~5nJ at a repetition rate of 80 MHz. The oscillator pulses are stretched to ~200ps in a single grating stretcher before being sent to the regenerative amplifier.

Two electro-optic Pockels cells triggered at 1kHz are used to trap a seed pulse from the oscillator in the regenerative amplifier and eject it after amplification. A Brewster-cut Ti:Sapphire crystal with a 25.4mm optical path length is the gain medium in the regenerative amplifier. This crystal is cooled to $-10°C$ and is pumped by a ~20W average power, frequency doubled Nd:YLF laser (Coherent Evolution). After ~10-15 round trips in the regenerative amplifier cavity, the pulse energy increases by a factor of ~10^6, reaching ~6.5mJ. At the next amplification stage, the pulse passes through a 12.7mm long crystal cooled to $-10°C$ and pumped by a ~30W frequency doubled Nd:YLF laser (Coherent Revolution). The pulse energy at this single pass amplifier increases by a factor of ~2, reaching ~12.5mJ. After

amplification, the beam is collimated using a reflective telescope and then sent to the grating compressor.

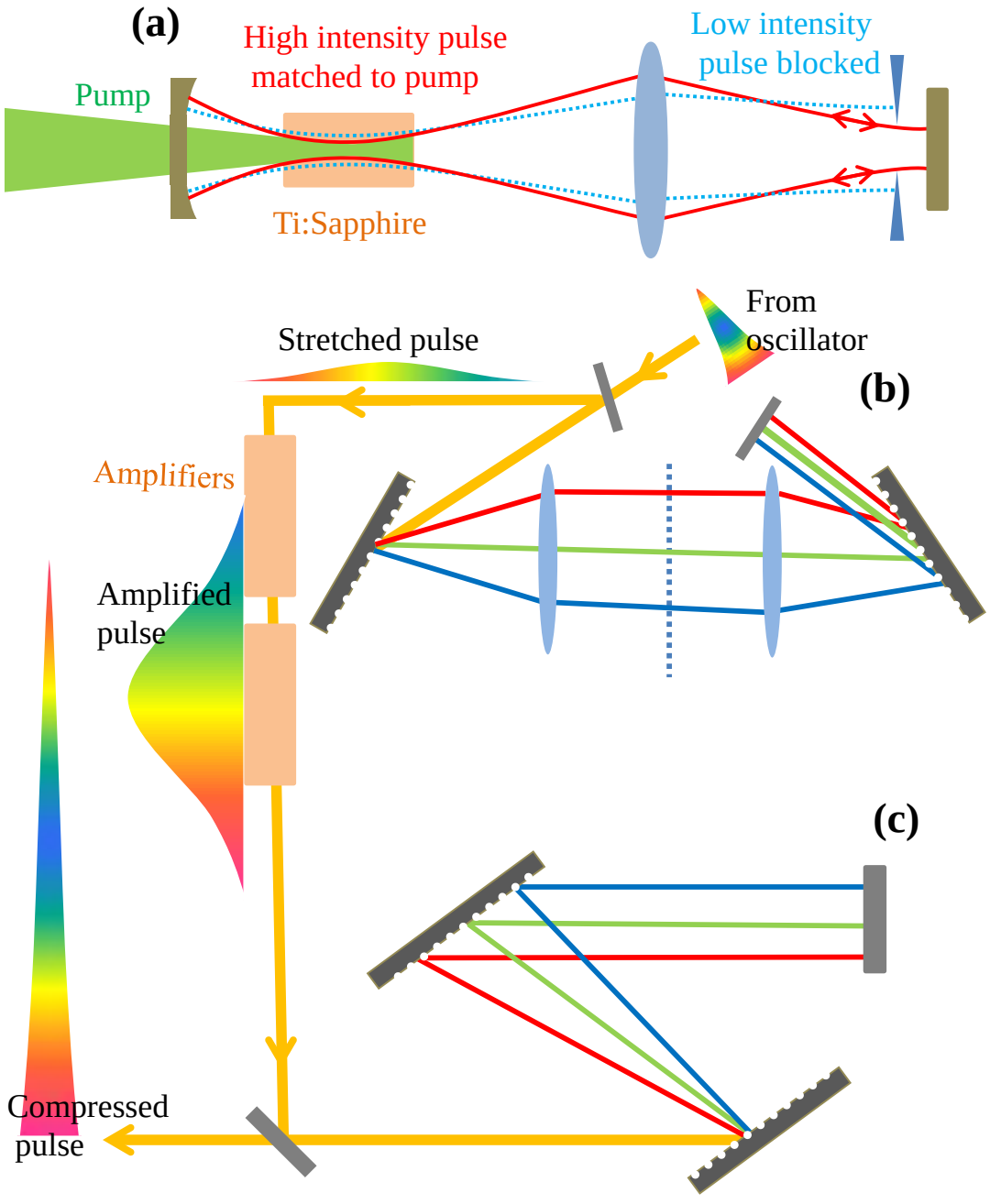

Figure 2.1. Schematic drawing showing the (a) Kerr-lens mode-locking, (b) grating stretcher design, and (c) a grating compressor.

The compressor consists of two parallel holographic gratings (1500 grooves/mm). and compresses the pulse to ~35fs. The throughput efficiency of the compressor is ~80%, reducing the final output pulse energy to ~10mJ. Figure 2.2 is a block diagram showing the laser components as described above. Part of the laser energy is coupled into a hollow core fiber compressor that will be discussed later in this chapter. The components related to few-cycle pulse generation are enclosed by the dashed line.

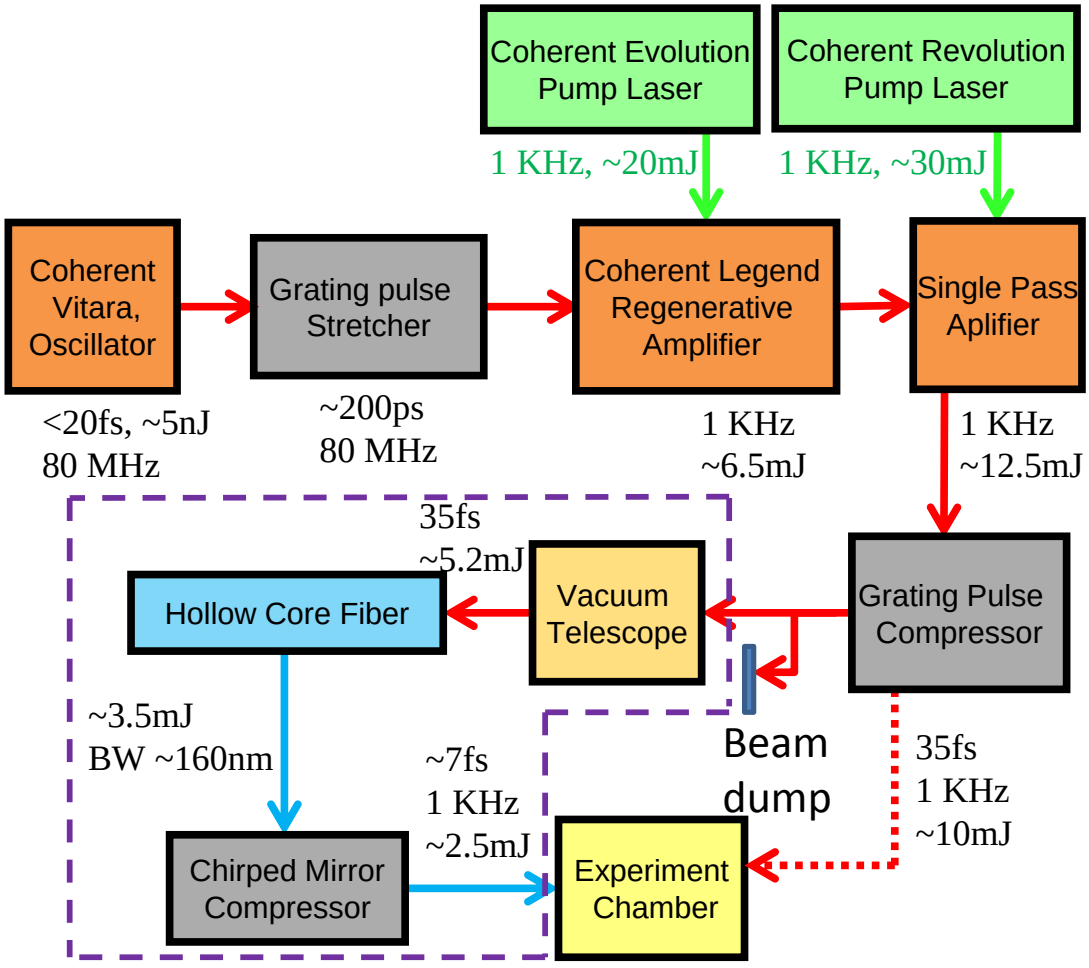

Figure 2.2. Block diagram of Ti:Sapphire laser system used in the experiments of this dissertation. The dashed line encloses the components used for few-cycle pulse generation.

2.3 *Few-cycle laser pulses*

The theoretical minimum pulse duration from a pulse with a given spectrum is determined by the Fourier transform limit. For a Gaussian pulse with Δt and $\Delta\omega$ as the FWHM duration and bandwidth, we have $\Delta t \Delta\omega/2\pi \geq 0.44$. For extremely short pulses with durations of only a few times longer than the cycle period corresponding to the central frequency, the spectral bandwidth must be on the order of an octave. For such few-cycle pulses, the carrier envelope phase (CEP) takes on more importance than it does in longer pulses, as a varying CEP may result in the cycle peak of the E-field being temporally shifted with respect to the envelope peak ("CEP offset"). Using the "f-2f interferometry" method, interfering a low frequency component of the second harmonic of the octave spanning pulse and a high frequency component of the original spectrum enables detection of the CEP offset and then its control through a feedback loop [87].

Few-cycle laser pulses are central to our experiments in resonant LWFA in near-critical plasmas. To achieve few-cycle pulses, one has to greatly increase the spectral bandwidth. The gain bandwidth limits the duration of the shortest pulse that can be generated by an oscillator. No known laser gain medium can amplify a bandwidth large enough to support high energy pulses of $\lesssim 2$ cycles duration. For Ti:Sapphire oscillators, proper control of dispersion can lead to <10fs ($\gtrsim 3$ cycle) pulses [88,89]. However, as the pulse is amplified, its spectrum narrows ("gain narrowing") and its bandwidth is reduced. In addition, uncompensatable higher order spectral phase is introduced. Compression of these amplified pulses does not deliver the original pulsewidth (potentially as short as 10 fs). Owing to gain narrowing and

higher order spectral phase, typical Ti:Sapphire lasers have amplified and compressed pulses no shorter than FWHM > ~20fs.

The very large bandwidths necessary for few-cycle pulses are generated by self-phase modulation (SPM). The SPM process plus material dispersion produce pulses with $GDD > 0$. To achieve the shortest pulses consistent with the SPM-widened bandwidth, optical elements are then introduced to impose $GDD < 0$. At low pulse energies, and with gain media that support large bandwidths, this can be done in an oscillator [89]. However, higher energy (> ~10 nJ scale) few-cycle pulses cannot be generated by an oscillator owing to catastrophic pulse collapse and optical filamentation and damage in the gain medium; for higher energy few-cycle pulses, the interplay between SPM and GDD is managed outside of a cavity.

2.3.1 Generation of few-cycle pulses

Many groups have used experimental setups involving gas cells, Herriot cells, thin solid plates, hollow core fibers, and OPCPAs to generate few-cycle pulses in different energy and wavelength regimes.

For pulses of peak power P that are multiple times the critical power for self-focusing ($P_{cr} = \frac{3.77\lambda^2}{8\pi n_0 n_2}$), the pulse can break up into multiple filaments if the propagation distance is long enough. P_{cr} ~10 GW for atmospheric pressure gases (P_{cr} is approximately 20× higher for helium [90,91]); for solids, with atomic densities 10^3 × higher, P_{cr}~ a few MW. SPM-induced spectral broadening in solids requires either operation at low pulse energies or with extremely thin samples to avoid self-focusing pulse collapse and material damage. At low pulse energies, broadening and

compression in bulk media within a Herriot cell [92] has been demonstrated, with 220 fs pulses compressed to 18fs with 2 μJ energy [93].

Starting with $\frac{P}{P_{cr}} > 1000$, and by focusing Ti:Sapphire pulses at $\sim 10^{13}\ W/cm^2$ through a series of $\sim 100 \mu m$ thick fused silica plates placed at Brewster's angle to the beam axis, broadband supercontinuum (SC) is generated [94]. Compression of the SC from such setups in a chirped mirror compressor has led to pulses with ~5fs duration and up to 0.7mJ energy [95]. However, scaling up the energy is very difficult because of multiphoton absorption and ionization in the plates, as well as filamentation in the air between the plates. This completely deteriorates the spectral phase of the pulse, making recompression (that is, imposing $GDD < 0$) ineffective.

Using a gas cell and starting with $\frac{P}{P_{cr}} \gtrsim 1$ leads to filament formation and only slight absorption of the pulse energy [96], but the output beam maintains good spectral phase coherence. Pulses with ~6fs duration and ~400 μJ energy have been generated using filamentation followed by compression with chirped mirrors (which impose $GDD < 0$) [97]. At mid-IR wavelengths ($\lambda \sim 3 - 8 \mu m$), the pulse can be compressed through propagation in a crystal (e.g., YAG crystal) with negative GDD instead of using chirped mirrors [80,81].

In many of the above few-cycle pulse generation setups, the compression is not uniform across the beam profile. In some cases, only a small section at the central region of the beam can be effectively compressed down to few-cycle duration. Also, the phase front quality of the beam profile is not always good enough for focusing to a diffraction-limited spot.

2.4 Hollow core fibers (HCFs)

The most common method for generating few-cycle pulses is the use of gas-filled hollow core fibers (HCF) for SPM-induced spectral broadening of an optically-guided high energy input pulse. The use of noble gases guarantees an electronic near-instantaneous nonlinear response for a wide range of pressures; changing the gas type and gas pressure can be used to control the size of the nonlinearity [98].

Use of solid core fibers for bandwidth broadening [76], limits the maximum achievable energy to below the μJ level due to the low damage threshold and higher order nonlinear effects deteriorating the pulse quality. Gas-filled hollow core photonic crystal fibers (HC-PCF) can be used to achieve broadband pulse energies up to ~100 μJ [99,100], but HC-PCFs typically have small core diameter and scaling up the pulse energy to the mJ level can be challenging and it has not been done yet. For multi-mJ pulse energies, the use of HCFs is the best practical option. In a much more complicated system using a broadband seed pulse from an HCF and amplification through optical parametric chirped pulse amplifier (OPCPA), it is possible to generate ~100 mJ few-cycle pulses [101,102].

In simple terms, guiding in HCFs is due to grazing incidence reflection of the beam from the inner surface of the fiber; this is fundamentally different from guiding in the usual solid core fibers, where there is a higher refractive index on axis. HCF guiding is also different from the HC-PCF case, where the existence of a bandgap in the photonic crystal cladding enables guiding [103].

In terms of modes, guiding in HCFs is primarily by the EH_{11} hybrid mode, which has the minimum loss. The radial intensity dependence of this mode is

$I(r)/I_0 = J_0^2\left(\frac{2.4r}{a}\right)$ where a is the inner radius of the fiber, J_0 is the zeroth order Bessel function, and I_0 is the peak on-axis intensity. Higher order modes have significantly greater leakage loss and only the fundamental EH_{11} mode can survive long propagation distances. The attenuation coefficient (in dB/m unit) due to propagation in the HCF is proportional to the square of the wavelength and the inverse cube of the inner radius of the fiber. The attenuation also depends on fiber bending: this portion is proportional to R_{fiber}^{-2} , where R_{fiber} is the local bending radius of curvature [104].

The overall attenuation constant is written as $\alpha = \alpha_0 + \alpha_R$ where $\alpha_0 \propto \frac{\lambda^2}{a^3}$ is the attenuation for a straight fiber, and $\alpha_R \propto \frac{1}{R_{fiber}^2}\frac{a^3}{\lambda^2}$ is responsible for attenuation due to fiber curvature [105].

The best coupling of a TEM_{00}free space Gaussian mode to an EH_{11}fiber mode happens when the beam waist is placed at the fiber entrance and $w_0/a = 0.64$ [106]. The SPM-broadened EH_{11}mode launched at the fiber exit can be approximated by a Gaussian beam with $w_0/a \simeq 0.59$ in the far field region [107].

Stretching a flexible fiber from two ends increases R_{fiber} significantly and lowers the fiber losses [108]. HCFs are usually very sensitive and brittle, but having a Polyamide coating on fused silica fibers increases their strength and flexibility, enabling fiber stretching (and making fibers easier to handle and store).

For a given HCF inner radius a, the maximum guided pulse energy is limited by self-focusing of the pulse at the entrance of the fiber and ionization of the fill gas (which flows out the end), which can degrade beam coupling and the spatial and

spectral beam quality of the pulse exiting the fiber. Slight ionization at the entrance from multiphoton absorption is tolerable as long as the contribution of plasma formation to the change in the refractive index is much smaller than the nonlinear Kerr index. The ionization threshold limits the maximum intensity at the fiber entrance and determines the minimum fiber inner radius a. Another limit is imposed by the critical self-focusing power $P_{cr} = \frac{3.77\lambda^2}{8\pi n_0 n_2}$ which can lead to pulse collapse and plasma formation [109]. For pulse durations <50fs, where the electronic response is the dominant mechanism determining the nonlinear refractive index, $n_2 \simeq 8 \times 10^{20}\, cm^2/W$ for the main air constituents [110] leading to $P_{cr} \simeq 12GW$. For a 35fs pulse, this corresponds to a $\sim 400\mu J$ pulse energy, which precludes the use of air as the HCF fill gas for compression of mJ-scale pulses. The maximum power and intensity conditions set above imply that using gases with high ionization potential and low nonlinear index is the key for increasing the maximum energy of the injected pulse. This leads to noble gases such as helium and neon as the best HCF fill gas candidates.

Given the pressure dependence of the nonlinear refractive index [111], it is desirable to generate a gas density gradient along the fiber with low density at the beam entrance and high density at the exit. This is accomplished by differentially pumping the gas through the fiber, with the pump port located near the HCF entrance and the gas fill located near the exit. Using this method, filamentation at the entrance is avoided, and as dispersion lowers the pulse intensity (and losses lower the energy) towards the end of the fiber, the higher gas density near the exit increases the nonlinearity and the spectral broadening [112].

Starting with a positively chirped pulse [113] or using a circularly polarized beam [114] can also help to increase the maximum achievable pulse energy by lowering the peak laser field amplitude at the HCF entrance.

For mid-IR wavelengths, the larger wavelength and lower nonlinear refractive index lead to higher P_{cr}. This leads to a higher maximum achievable injection power, leaving ionization in the tunneling regime as the main constraint [115].

The spectral broadening factor from SPM is calculated as $\frac{\Delta\omega_{out}}{\Delta\omega_{in}} = (1+\frac{4}{3\sqrt{3}}B^2)^{1/2}$ where $B = \frac{2\pi}{\lambda}\int_0^L n_2 I dx$, the so-called B-integral introduced earlier, is the nonlinear phase accumulated due to propagation in the gas [116]. It is clear that for keeping the intensity I moderate to avoid self-focusing or excessive ionization, the use of longer fibers is the best way to increase the broadening factor.

2.5 Few-cycle HCF setup

The HCF used for experiments in this thesis is a polymer coated fused silica fiber with ~500um ID and ~2.5 meter length (from Few-Cycle, LLC). The fiber holders are designed so that the tension on the fiber, the position of the fiber tip, and the tilt angle of the tip for alignment are all easily adjusted. The fiber tension and fiber tip position and tilt are adjusted as the fiber is being optically aligned with a long input pulse, such that the maximum output energy and highest quality mode are achieved. The fiber is initially aligned with an unseeded beam from the regenerative amplifier at low energy ($250\mu J$,~$10ns$). For regular operation, injection of $5.2mJ$ pulses at the HCF entrance leads to $3.5mJ$ SPM-broadened pulses at the exit with ~67% energy throughput.

For HCF injection, the input beam is prepared as follows. Output pulses from the Ti:Sapphire laser system are $\sim 35 fs$ pulse with a $1/e^2$ intensity beam diameter $2w_0 \sim 12mm$. The beam is focused through a folded reflective telescope with a 3.3m focal length to a $2w_0 \sim 320\mu m$ spot diameter ($1/e^2$ intensity) at the HCF entrance. The telescope is located inside a vacuum chamber with a thin entrance window (1mm), connected to the fiber tip holder through KF vacuum tubes. This design helps to minimize the nonlinear phase accumulation from the air and window. The exit side of the fiber is also connected to a KF tube extending ~1.5m beyond the fiber exit before the beam exits through a 1mm thick window. The long length of the chamber at the exit side allows the spot size to expand to avoid deleterious nonlinear phase shifts or self-focusing in the exit window.

Depending on the desired output pulse energy, the system can be filled with different noble gases (typically He, Ne or Ar) under either a static gas fill (pressure uniform along the fiber) or under differentially pumped conditions (pressure gradient along the fiber, with the highest pressure at the HCF exit). For the highest energy output, the best results are for helium gas fill under differential pumping. In this configuration, helium gas at $\sim 160 KPa$ (0.6atm above ambient) is injected into the exit side chamber and is pumped through the HCF towards the laser beam input, where a dry scroll pump (pumping speed $\sim 6.8 \frac{m^3}{h} \sim 4$CFM) is connected to the reflective telescope chamber. Under these conditions, the pressure at the telescope chamber is $\sim 1 KPa$.

Under optimum conditions (post-compression pulsewidth = 7 fs and energy =2.5 mJ), the FWHM bandwidth of the beam after exiting the fiber is $\geq 160nm$,

which corresponds to a $\sim 4fs$ duration if compressed to the transform limit. The beam is collimated using a f=2.5m concave mirror located a focal length away from the fiber exit tip. The beam's measured $2w_0$ beam diameter at the mirror point is $\sim 8.4mm$ for the low energy, long pulse alignment beam, and $\sim 8mm$ for the high energy broadened pulse. These numbers are close to the beam diameter expected from the diffraction of a Gaussian beam from the fiber exit. The smaller spot size at high power is probably due to weak self-focusing of the beam in helium after it exits the fiber.

At the final stage of the setup, the beam is sent to a chirped mirror compressor consisting of custom double angle dispersive mirrors (Ultrafast Innovation PC70) [79], and a pair of thin fused silica wedges for fine tuning the GDD. The compressor has 8-12 reflections from the chirped mirrors with an equal number of reflections at incident angles of $5°$ and $19°$. The mirrors cover a large bandwidth (500nm to 1050nm) and on average compensate for a GDD of $-40fs^2$ per reflection. The adjustable wedge pair fine tunes the GDD by changing the amount of fused silica in the beam path. It is important to have a small separation between the two wedges and to keep this separation fixed as the amount of glass is adjusted to avoid introducing spatial chirp to the beam. Figure 2.3 shows images of the fiber and chirped mirror compressor, as well as the scanning TG-FROG used for characterizing the few-cycle pulses (Sec. 2.6).

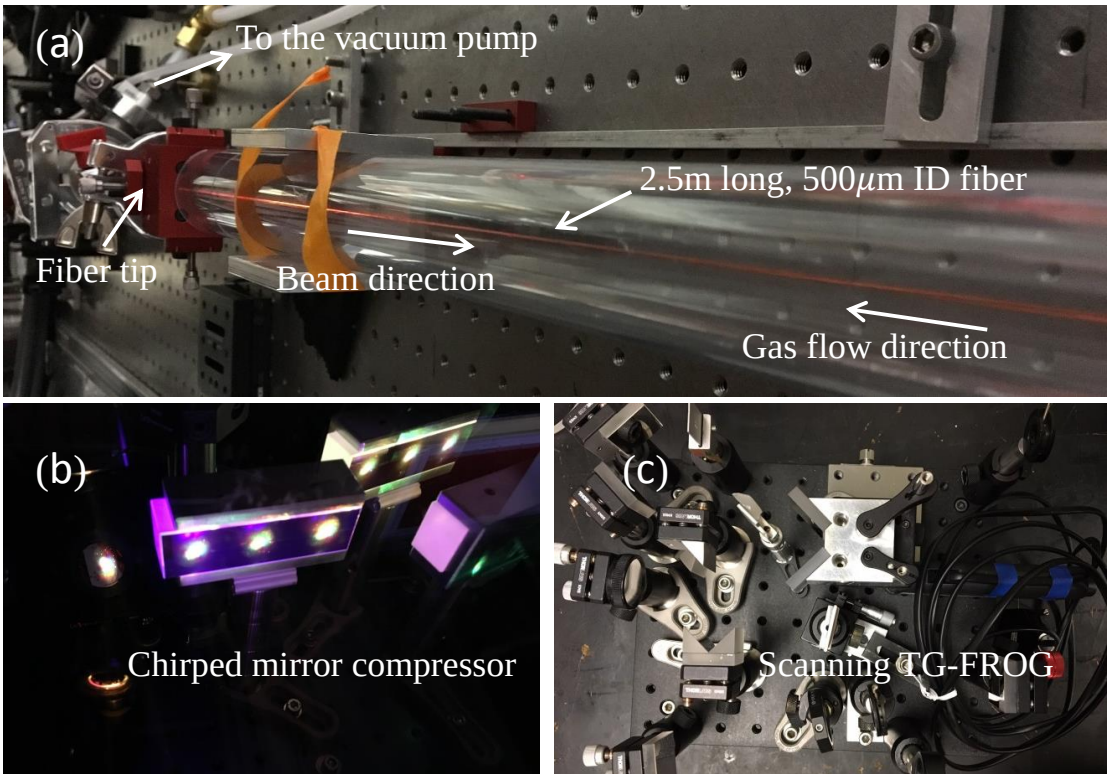

Figure 2.3. Hollow core fiber setup. (a) fiber protected in an acrylic tube (rotated view) (b) chirped mirrors in a 12-reflection configuration, (c) the scanning TG-FROG used for pulse characterization (Sec. 2.6)

2.6 Pulse length measurement-FROG

Various techniques such as frequency resolved optical gating (FROG) [117], spectral phase interferometry for direct electric-field reconstruction (SPIDER) [118], dispersion scan (d-scan) [119,120], and time domain ptychography [121] can be used to characterize few-cycle pulses. Among the FROG family of diagnostics, second harmonic generation (SHG) and transient grating (TG) FROGs are best suited for few-cycle pulse measurement. SHG-FROG is a spectrally resolved pulse autocorrelation, yielding a trace that is symmetric in time and hence leaves the time direction ambiguous. Since SHG requires only a 2nd order nonlinear effect, it is the

FROG diagnostic sensitive to the lowest pulse energies. In the case of few-cycle pulses with very broadband spectra, satisfying the phase matching condition for SHG across the whole bandwidth requires a very thin nonlinear crystal. For pulses generated from the HCF setup, a $\sim 10 \mu m$ thick BBO crystal cut at the proper angle can support the full ~160 nm bandwidth.

TG-FROG uses the 3rd order nonlinearity and requires 3 identical copies of the pulse that is being measured. Two of the beams are overlapped in time and in space in a nonlinear medium (e.g., a fused silica plate), producing a transient grating [122]. The 3rd pulse spatially overlaps the other pulses; it is variably delayed in time with respect to the induced grating to produce the signal pulse. Figure 2.4 shows a scanning TG-FROG where three distinct beams are sampled from the main beam using an input mask and are focused on a thin fused silica plate. The generated signal should be separated from the leftover pump beams and higher order diffractions, using the conjugate of the input mask at the output side. The TG-FROG device is built using all reflective optics and does not require transmission through any material other than the thin fused silica plate used for nonlinear wave mixing. The avoidance of material dispersion makes TG-FROG ideal for measurement of few-cycle pulses [123]. It is possible to switch the fused silica with a thin BBO crystal, block one of the beams so that a stationary and a delayed arm beam are left, (block beam #2 or #3 in Fig. 2.4), and convert this TG-FROG to a scanning SHG-FROG.

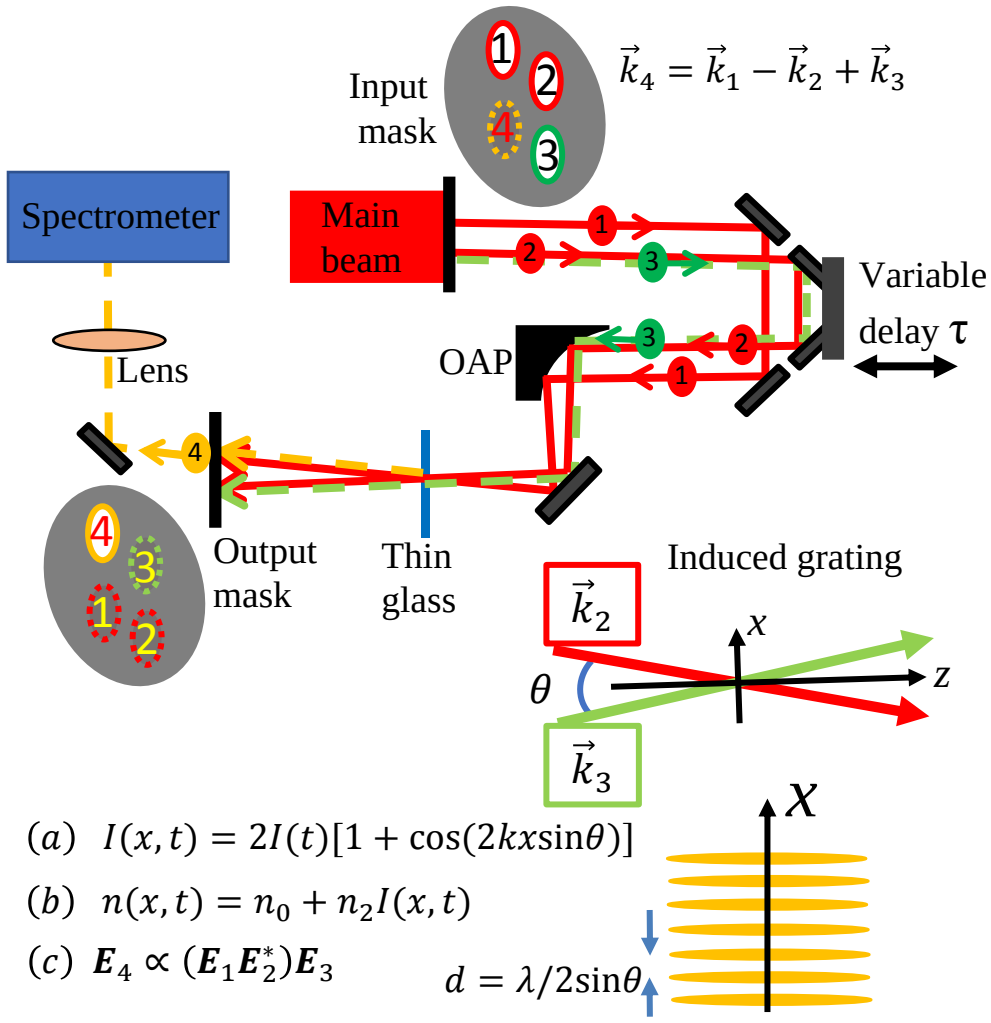

Figure 2.4. The optical design of a TG-FROG. Three beams are sampled from the main beam using a mask. Two of them (# 2 and 3) form an induced grating and the third (#1) is diffracted from the induced grating for a sequence of scanned delays. The TG signal (#4) is isolated using the conjugate of the input mask at the output side. The equations underlying TG-FROG are also shown (a) the intensity where the delay arm beams interfere, (b) the resulting induced refractive index, and (c) the signal dependence on the input beams. Here d is the fringe spacing and $\boldsymbol{E}_i$ is the electric field for beam number i.

The TG-FROG signal is $E_{sig}^{TG}(t,\tau) = E_1(t)E_2^*(t-\tau)E_3(t-\tau)$, and since all three pulses are identical, the signal field and recorded trace can be simplified to [124,125]:

$$E_{sig}^{TG}(t,\tau) = |E(t-\tau)|^2 E(t) \quad \text{(a)}$$
$$I_{FROG}^{TG}(\omega,\tau) = \left|\int_{-\infty}^{\infty} |E(t-\tau)|^2 E(t)\exp(-i\omega t)\,dt\right|^2 \quad \text{(b)} \tag{2.4}$$

The goal of retrieving a FROG trace is to find a signal field that satisfies the above equations. The algorithms used for the reconstruction of the phase and amplitude of the pulse involves iterative Fourier transforming the signal field back and forth between the time and frequency domains [126]. Following the generalized projections algorithm [127], we can start with an initial guess for the field in the spectral domain. Replacing the guessed field's amplitude with the square root of the measured trace leads to

$$\tilde{E}'_{sig}(\omega,\tau) = \frac{\tilde{E}_{sig}(\omega,\tau)}{|\tilde{E}_{sig}(\omega,\tau)|}\sqrt{I_{FROG}^{TG}(\omega,\tau)}\,, \tag{2.5}$$

which satisfies Equation 2.4.b. Now finding the field in the time domain using the inverse Fourier transform $\tilde{E}'_{sig}(\omega,\tau) \rightarrow E'_{sig}(t,\tau)$, and using the field in the time domain to minimize the following "distance" metric

$$Z = \sum_{i,j=1}^{N} \left|E'_{sig}(t_i,\tau_j) - E(t_i-\tau_j)|E(t_i)|^2\right| \tag{2.6}$$

leads to a time domain signal that satisfies equation 2.4.a [127]. The Fourier transform $E_{sig}(t,\tau) \rightarrow \tilde{E}_{sig}(\omega,\tau)$ gives the new field in the frequency domain used in the next iteration.

At each iteration, a comparison between the experimentally measured trace $I_{meas}(\omega,\tau)$ and the retrieved trace $I_{ret}(\omega,\tau)$, based on the current iteration for the electric field, serves as a measure of retrieval convergence. The comparison is made using the FROG error G, defined by

$$G = \left(\frac{1}{N^2} \sum_{i,j=1}^{N} \left[I_{meas}(\omega_i, \tau_j) - I_{ret}(\omega_i, \tau_j) \right]^2 \right)^{1/2} . \quad (2.7)$$

In general, an error $G = 0.01$ or less for a 64×64 grid indicates acceptable convergence [127].

2.7 Characterization of the HCF output pulse

We used a scanning TG-FROG (Fig. 2.3(c)) for characterization of the HCF output pulse. Figure 2.5 shows the spectrum and intensity of the output pulse. In general, based on the output spectrum, the measured pulse duration is longer than the transform-limit due to higher order phase introduced in various components that is not compensated in the chirped mirror compressor. By comparing the input and output spectra it is clear, as explained in Chapter 1, that pulse self-steepening has resulted in a very asymmetric SC spectrum, shifting the spectral peak intensity from ~800 nm to ~680nm.

In practice, the input pulse energy and duration, and the helium pressure are carefully scanned for largest bandwidth with quadratic spectral phase. At higher gas pressures or pulse energies, plasma formation at the HCF input increases the bandwidth by adding a shoulder to the blue side of the spectrum. The larger bandwidth in this case, however, does not reduce the pulse length as the newly introduced higher order spectral phase terms make the pulse longer. Furthermore, part of this blue side bandwidth is outside the range covered by the chirped mirrors and other optics in the setup.

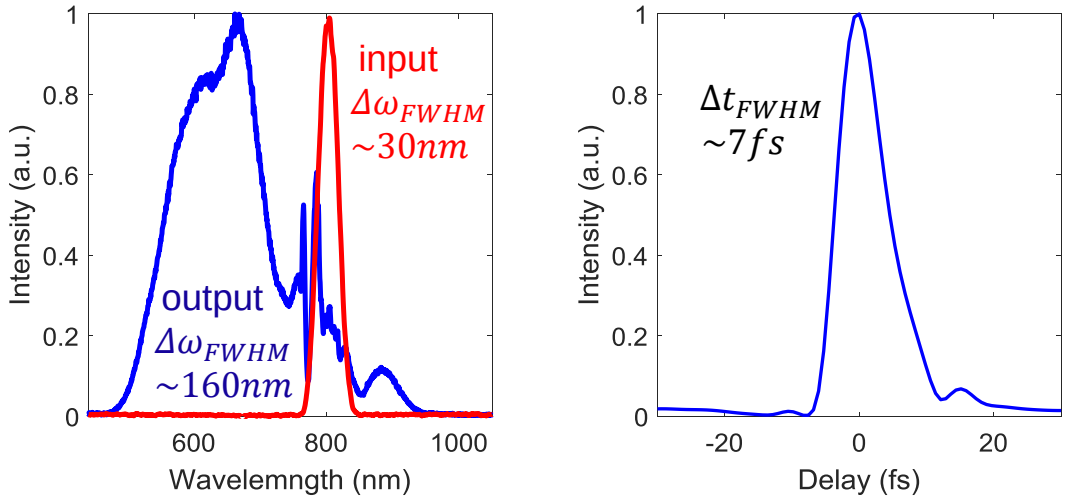

Figure 2.5. Characterization of the HCF output pulse. The central spectrum has a significant blue shift and the bandwidth has increased by more than factor of 5. (left) comparison of input (red curve) and output spectrum (blue curve) of the fiber, (right) compressed few-cycle pulse intensity envelope retrieved from TG-FROG trace.

At lower energies and gas pressures the spectral broadening is more symmetric and even though the bandwidth is smaller, the quadratic spectral phase helps to compress the beam to durations close to transform limit. Part of the higher order spectral phase originates from the chirped mirrors and the fused silica wedges used to compress the pulse, by minimizing the number of reflections from the mirrors and transmission length in windows we expect to reduce the pulse duration to ~5fs.

Chapter 3: Micrometer-scale cryogenically cooled gas jet for near-critical density laser-plasma interaction experiments

3.1 Introduction

Gas jets have been employed as targets in high intensity laser-matter interaction studies for decades. These experiments span a wide variety of applications including electron and ion acceleration [10,128–130], high harmonic generation [131,132], x-ray lasers [133], and even generation of fusion neutrons [134]. The main advantages of gas jets, compared to solid targets or static gas fills, are that they are a well-controlled, automatically replenishing target that can be used at high laser pulse repetition rates without requiring target rasterization schemes, and they allow the laser to propagate through vacuum before reaching the interaction volume. Fine control of the gas density and profile has been demonstrated by multiple groups through engineering of the valve design [135–137], nozzle geometry [138–141], and through external shaping of the resulting gas flow [142–145].

In prior experiments with gas jets, the gas density has generally been limited to less than $\sim 10^{20}\ cm^{-3}$, with interaction lengths on the millimeter scale. For typical hydrogen or helium gas jets, this density limitation precludes the study of near critical laser plasma interactions using Ti:Sapphire laser systems ($\lambda = 800\ nm$, critical density $N_{cr} \approx 1.7 \times 10^{21} cm^{-3}$) which is of interest for laser driven electron [21,130] and ion [146,147] acceleration experiments. Two notable exceptions to this limitation are the schemes presented by Sylla *et al*. [136] and Kaganovich *et al*. [142]

for achieving thin, high density plasmas suitable for the study of near critical phenomena. Sylla *et al*. achieved a critical density plasma by implementing a novel valve design which boosts the pressure above 4000 psi behind a 400 μm nozzle. Kaganovich *et al*. generated a shockwave in a standard gas jet by ablating a nearby metal surface with a nanosecond laser pulse a controlled time before arrival of the main interacting pulse. The density in the thin shock can be many times higher than the ambient gas density, boosting the target density into the near critical regime.

Here, we present a method for generating thin, near critical density plasmas which avoids pressure boosting schemes or secondary lasers. The technique uses a cryogenically cooled high pressure solenoid valve coupled to a variety of thin nozzles with inner diameter as small as 50 μm. Cryogenic cooling increases the density of atoms or molecules inside the gas valve reservoir for a fixed valve backing pressure which, in turn, increases the gas density at the nozzle exit plane. The jet can be operated in pulsed or continuous flow modes. Because near-critical plasma densities significantly reduce the threshold for relativistic self-focusing, this method of high density jet generation has made possible our recent results in accelerating MeV-scale electron bunches using peak laser powers well below 1 TW at high repetition rates, currently up to 1 kHz [20,21].

3.2 High density valve design

The high density jet design consists of a homemade nozzle, and a high speed solenoid valve (Parker series 99 miniature valve) controlled through a commercial valve driver (Parker IOTA One). The solenoid valve and the high pressure gas feed

tube are held in a custom cooling jacket which uses a combination of liquid nitrogen and electrically driven heating elements to control the valve reservoir temperature. The reservoir temperature can be controlled to within 1 degree Celsius between room temperature and −160º C. The valve seal is formed by a Teflon poppet on a 1 mm diameter orifice. The valve body is modified for mounting of a 3mm thick adaptor plate in a way that the poppet seat orifice transitions directly to a straight 1 cm long stainless steel capillary (the "needle nozzle") with an inner diameter ranging from 50 μm to 150 μm soldered to the adaptor plate. The needle nozzle length is set by the accessibility of small *f*-number laser focusing, in our laser interaction experiments. Upon opening of the poppet, the gas is forced through the needle nozzle into the vacuum chamber. The volume of the gas exiting the nozzle is negligible compared to the volume in the valve and feed tube, where the gas is effectively under stagnation conditions. As is well known, the nozzle shape has a significant effect on the gas density profile [148]. As discussed below, our use of straight nozzles and sonic flow give different profiles than supersonic nozzles employing a converging-diverging design to achieve high Mach number flows [135,149–151].

Controlling the reservoir temperature, T_0, and pressure, P_0, along with the nozzle diameter allowed us to access peak molecular densities in the range 10^{19}-10^{21} cm^{-3} while maintaining a ~200 μm target thickness. The radial density profile of the gas flow was nearly Gaussian with full width at half maximum (FWHM) of 150-250 μm at a height 150 μm above the nozzle, depending on the nozzle inner diameter. Depending on the gas species used, when ionized this covers underdense through

overdense plasma regimes for a λ=800 nm Ti:Sapphire laser ($N_{cr} \approx 1.7 \times 10^{21} cm^{-3}$).

The flow of gas from the jet can be modeled as the steady, one-dimensional isentropic flow of an ideal gas into a low pressure reservoir [152]. Gas from the reservoir is forced through the needle nozzle by the pressure gradient between the reservoir and vacuum chamber which is held at a pressure $P_b \sim 10\ mTorr$. In an ideal 1D isentropic flow the gas density N can be expressed in terms of the gas specific heat ratio, $\gamma = \frac{C_P}{C_V} > 1$and the local Mach number, $M = v/c_s$where v is the gas velocity, c_s is the sound speed, and N_0 is the gas density at the reservoir [153] :

$$N = N_0(1 + \frac{\gamma - 1}{2} M^2)^{-\frac{1}{\gamma - 1}} \tag{3.1}$$

Equation 3.1 indicates the gas density drops rapidly as the Mach number increases ($(\gamma - 1)^{-1} = 2.5$, using $\gamma = 1.4$for H_2). Therefore, to reach the highest density possible at the nozzle exit, the Mach number should be minimized. This is in contrast to supersonic nozzles used for those laser-plasma interaction experiments where a flat top transverse density profile is desirable. For both sonic and supersonic nozzles, the mass flow rate and the peak density are limited by sonic choking, which limits the flow velocity to M = 1 at the minimum orifice diameter [153].

For an ideal diatomic gas ($\gamma = 1.4$) under 1D isentropic flow conditions, the molecular density at the choke point (M = 1) is

$$N^* = N_0(\frac{2}{\gamma + 1})^{\frac{1}{\gamma - 1}} \cong 0.63 N_0 = 0.63 \frac{P_0}{k_b T_0} \tag{3.2}$$

Equation 3.2 shows that increasing the gas density at the nozzle exit is achieved simply by increasing the gas density in the reservoir. Increasing the reservoir density

is achieved by increasing the nozzle backing pressure, P_0, or by decreasing the reservoir temperature, T_0. Cryogenic cooling of the reservoir thus serves to increase the jet output density proportional toT_0^{-1}. It should be noted that this relation holds regardless of the sonic (M = 1) versus supersonic (M > 1) nature of the nozzle, so cryogenic cooling is an effective method for increasing the density of supersonic nozzles such as those designed in references [135,136,149].

3.3 Experimental setup

The output density of the gas jet as a function of temperature, pressure, and nozzle geometry was characterized by transverse interferometry with a 70 fs, 400 nm probe pulse derived from our 25 TW Ti:Sapphire laser system [154,155]. Figure 3.1 shows a diagram of the experimental setup. The probe pulse passes through the gas jet and enters a folded wave front interferometer, with the phase shift $\Delta\phi(x,z)$ extracted using Fourier techniques [156], where x is the coordinate transverse to the gas jet flow direction and z is the distance from the jet orifice along the flow. The extracted 2D phase profile is related to the radial refractive index profile $n(r,z)$ through the inverse Abel transform

$$n(r,z) - 1 = -\frac{1}{k\pi}\int_r^{r_0}\left(\frac{d\Delta\phi(x,z)}{dx}\right)\frac{dx}{\sqrt{x^2-r^2}} \tag{3.3}$$

giving the gas density profile

$$N(r,z) = \frac{n(r,z)-1}{2\pi\alpha}$$

Here, $k = 2\pi/\lambda$ is the probe wavenumber, r is the radial coordinate, r_0 is a radius at which the gas density goes to zero, and α is the gas molecular polarizability. The

integral transform of Eq. 3.3 can be solved numerically or, with a suitable analytic profile fit to $\Delta\phi(x,z)$, analytically.

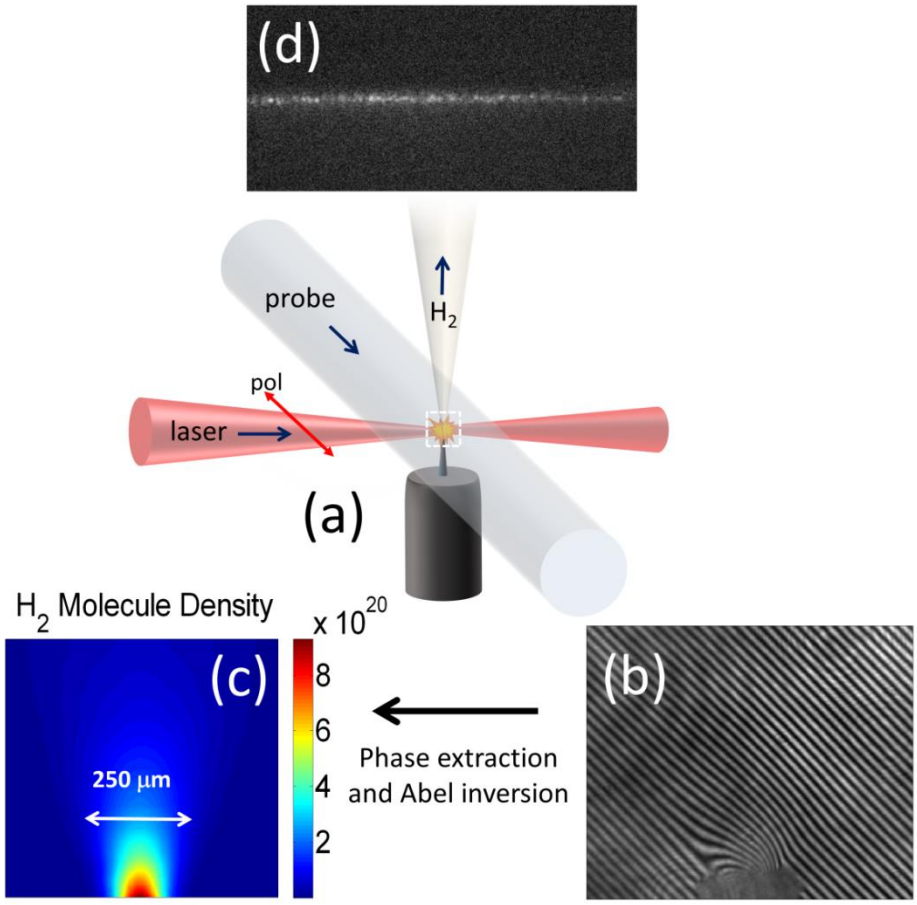

Figure 3.1. Experimental setup for characterizing the high density gas jet (a). Density measurements were made using transverse interferometry. A raw interferogram (b) and Abel inverted density profile (c) are shown along with a raw image of Rayleigh scattering (d) used to measure the cluster size and density in the jet.

In all measurements, $\Delta\phi(x, z = z_0)$ was well fit by a Gaussian function at heights $z_0 = 50$ μm or more above the nozzle orifice. Taking $\Delta\phi(x, z_0) = \Delta\phi_0 \exp(-\frac{x^2}{\sigma^2})$, the index profile is calculated from Eq. 3.3 to be

$$n(r, z_0) - 1 = \frac{1}{k}\frac{\Delta\phi_0}{\sqrt{\pi}\sigma}\exp(-\frac{r^2}{\sigma^2})$$

A numerical Abel inversion routine based on the fast Fourier transform was also implemented [157]. Numerical Abel inversion generally agreed with the Gaussian fit-based analytical Abel inversion to within ~10%. The panels in Fig. 3.1 show a sample raw interferogram (b), Abel inverted density profile $N(r, z)$ (c), and a sample image of Rayleigh scattering (d) used to measure cluster size in the high density jet.

3.4 Hydrogen jet density measurements

Hydrogen gas is commonly used in laser plasma interaction experiments because of the ease with which it is fully ionized by the leading temporal edge of a suitably intense femtosecond laser pulse. Complete ionization mitigates ionization-induced refraction of the main interacting pulse. However, since each hydrogen molecule can only contribute two electrons, high plasma densities have been very difficult to reach without the use of some higher Z gas such as nitrogen or argon. Figure 3.2(a) shows a sample Abel-inverted density profile $N(r, z)$ of the hydrogen gas jet (100 μm needle nozzle, 1000 psi backing pressure, and −160º C reservoir temperature). The lineouts in Fig. 3.2(b), taken 70, 100, and 200 μm above the nozzle, show a near-Gaussian radial density profile. The peak molecule density 70 μm above the nozzle is $9 \times 10^{20} cm^{-3}$ which, when fully ionized, gives a peak plasma density of $1.8 \times 10^{21} cm^{-3}$ or $1.03 \times N_{cr}$ for $\lambda = 800nm$. Figure 3.2(c) shows the exponential decay of the peak gas density as a function of height above the

nozzle for a series of backing pressures. The decay length is approximately 67 µm, independent of the valve backing pressure. The exponential decay of the peak density is driven by the gas expansion, and the profile FWHM increases linearly as a function of height above the nozzle, as shown in Fig. 3.2(d).

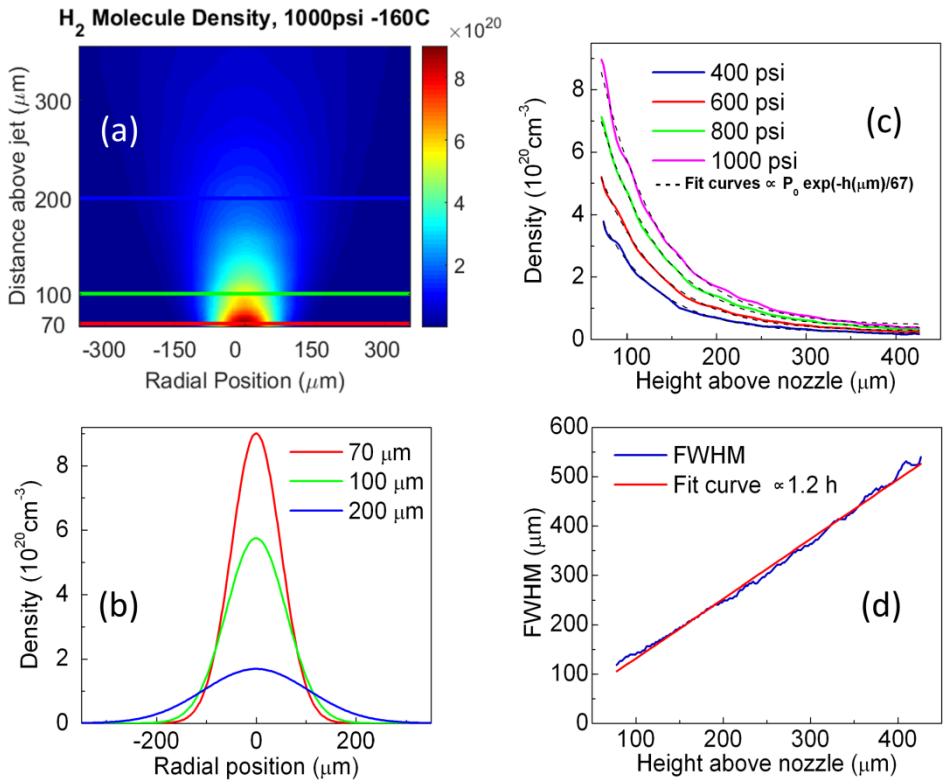

Figure 3.2. Sample 2D hydrogen molecule density profile (a) with 1000 psi backing pressure and $-160°C$ reservoir temperature and lineouts 70, 100, and 200 µm above the nozzle (b). The peak density as a function of height decays exponentially (c) and the FWHM increases linearly with height above the jet (d).

To minimize gas loading of the experimental chamber, the solenoid valve should have a fast rise time, reaching the desired stable output quickly. Figure 3.3 shows the measured temporal evolution of the helium gas output from a 150 µm diameter needle nozzle with the valve reservoir held at 1100 psi and -140º C for four different durations of the solenoid current pulse which drives the valve poppet. Each

point in Fig. 3.3 represents the maximum measured gas density at 200 µm above the needle nozzle. The 10% to 90% rise time of the gas density is approximately 400 µs, after which the measured output stabilizes for all four current pulse durations. The rise time was found to be relatively independent of pressure, temperature, and gas species. To minimize gas load, a current pulse duration of $700\mu s$ was used for all subsequent results in this paper. For high repetition rate applications, such as in our recent demonstration of MeV electron acceleration at 1 kHz repetition rate, the current pulse can be set at arbitrarily long durations [20]. Also where the gas load is not an issue, it is possible to switch to continuous flow mode by removing the poppet.

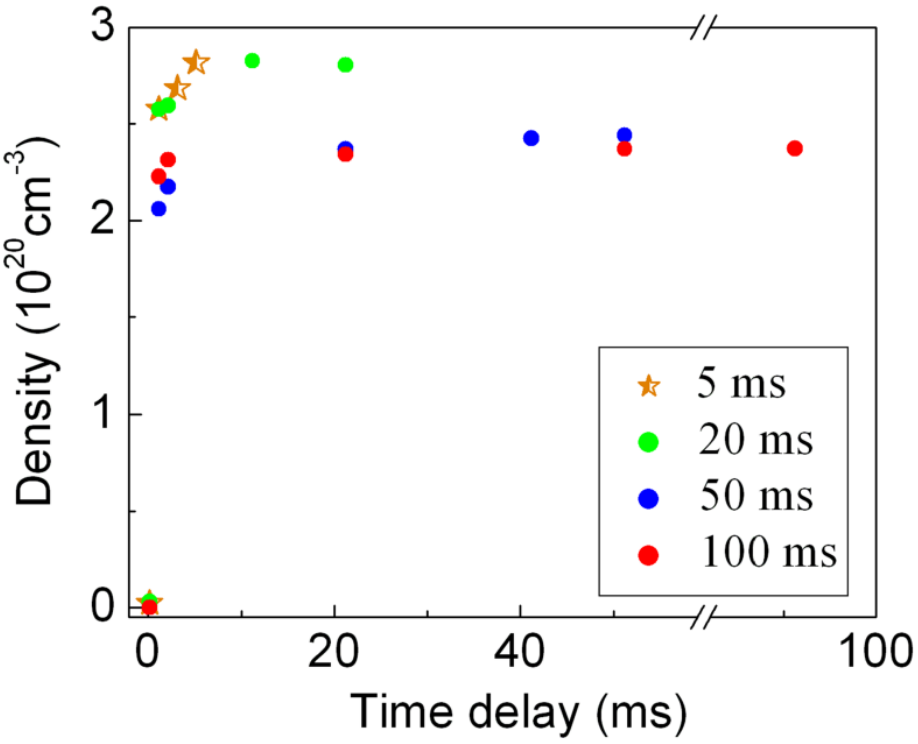

Figure 3.3. Helium density versus time delay at 200 µm above the 150 µm nozzle with the jet reservoir held at 1100 psi and -140° C for 5 ms, 20 ms, 50 ms, and 100 ms current pulse durations.

Figure 3.4(a) shows the peak hydrogen molecule density 200 µm above the 150 µm diameter needle nozzle as a function of backing pressure with a fixed temperature of –160º C. In agreement with the isentropic flow model, the measured density varies linearly with pressure. Figure 3.4(b) shows the dependence of the peak gas density at the same location for a fixed pressure of 1000 psi as a function of temperature. The peak density at –160º C is enhanced by a factor of ~2.4 compared to the peak density at room temperature, highlighting the effectiveness of cryogenic cooling for increasing gas jet density output. The measured density as a function of temperature is roughly proportional to $T_0{}^{-0.87}$. Departure from the $1/T_0$ dependence is possibly caused by viscous effects in the flow, as the dynamic fluid viscosity is a function of the fluid temperature [158].

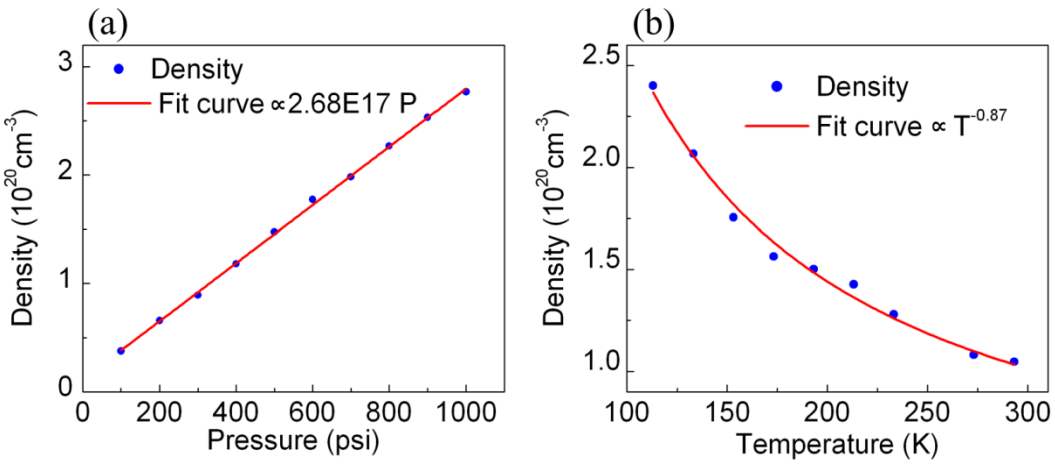

Figure 3.4. Peak hydrogen molecule density 200 µm above the 150 µm needle nozzle (a) as a function of valve backing pressure at a fixed reservoir temperature -160º C (113 K) and (b) as a function of reservoir temperature at a fixed backing pressure 1000psi.

Finally, the density of hydrogen gas was measured for a series of nozzles with inner diameters of 50, 100, and 150 µm. Viscous forces cause significant pressure

drop and therefore lower peak densities for smaller diameter nozzles. Figure 3.5 shows the output density as a function of height for a fixed reservoir temperature and pressure of −160º C and 1000 psi for all three nozzle designs.

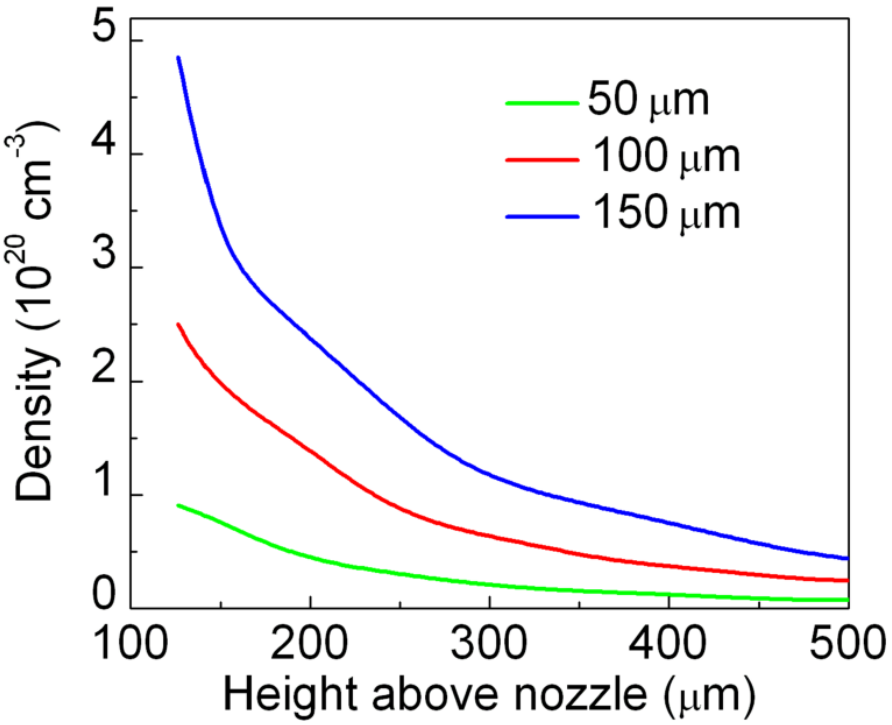

Figure 3.5. Hydrogen molecule density as a function of height above needle nozzles with 50 μm (green), 100 μm (red), and 150 μm (blue) inner diameter, all at −160º C and 1000 psi

3.5 Characterization of clusters from high density jet

In many experiments involving high pressure gas jets, clustering of molecules can play an important role. Collisional ionization within the solid density clusters can greatly enhance ionization and increase laser-plasma coupling [159,160]. The laser

cluster interaction has been demonstrated as a source of fast ions [128,161], electrons [162,163], x-rays [160,164], and even neutrons [134,165]. Ballistic cluster flows can also be used to make shaped plasma density profiles using obstructions smaller than the cluster mean free path [145].

3.5.1 Cluster formation

Due to the rapid expansion of the flow out of the nozzle, under certain conditions, the fluid can reach a metastable supersaturated state without condensation [166]. If a threshold value of supersaturation is passed, sudden nucleation forms clusters throughout the fluid [167]. The onset of the supersaturation threshold required for this spontaneous nucleation depends on the initial thermodynamic state and the kinetics and time scale of the expansion [168].

The size and density of the clusters can be characterized using Hagena's empirical parameter

$$\Gamma^* = \frac{k d^{0.85} P_0}{T_0^{2.29}} \tag{3.4}$$

Where k is a gas dependent constant, d is the orifice diameter in μm, P_0 is the backing pressure in mbar, and T_0 is the stagnation temperature [169]. The value of $k$varies widely for different gases and it is generally higher for gases with higher polarizability. For example $k = 1650$ for argon and $k = 180$ for hydrogen while for helium $k = 3.85$ where there is negligible clustering [170].

Clustering starts to be observed for Γ^* in the range of 200-1000. The average number of molecules in the cluster is empirically given by $\langle n_c \rangle = 33(\frac{\Gamma^*}{1000})^{2.35}$ [168],

which can be used along with the Wigner-Seitz radius r_{WS}, to find the average cluster radius $a = r_{WS} {n_c}^{1/3}$. The dependence $\langle n_c \rangle \propto \Gamma^{*2.35}$ shows that higher pressure, lower temperature, and higher nozzle diameter leads to larger cluster size.

3.5.2 Cluster size and density measurement

The mean size and density of clusters in the high density gas jet can be estimated through an all optical technique combining transverse interferometry and collection of Rayleigh scattered light from the clusters [155]. When the cluster size is comparable to the laser wavelength, the scattering from the clusters should be treated by Mie scattering formulas [171]. The Rayleigh scattered energy into a collection lens by a laser propagating from point x to $x + \Delta x$ through a cluster jet is given by $\Delta E_{lens}(x) \approx E_{in} \bar{\sigma}_{lens}(x) N_c(x) \Delta x$ where E_{in} is the incident laser energy on the scattering volume, $\bar{\sigma}_{lens}$ is the cross section for scattering into the lens averaged over the cluster size distribution, and N_c is the average cluster density. For 90° scattering and cluster sizes much less than the laser wavelength $\sigma_{lens} = \pi k^4 |\Gamma|^2 (\alpha^2 - \alpha^4/4)$ where $k = 2\pi/\lambda$ is the laser wavenumber, $\Gamma = a^3(\varepsilon - 1)(\varepsilon - 2)^{-1}$ is the cluster polarizability assuming a spherical cluster of radius a and dielectric constant ε, and α is the collection half angle of the imaging lens [155]. Using this cross section in the equation for the scattered energy gives

$$\overline{a^6} N_c = \frac{1}{\pi k^4} \left| \frac{\varepsilon + 2}{\varepsilon - 1} \right|^2 \frac{\Delta E_{lens}}{E_{in} \Delta x} \left(\frac{1}{\alpha^2 - \alpha^4/4} \right) \tag{3.5}$$

Where $\overline{a^6}$is an average of a^6 over the cluster size distribution [155]. Transverse interferometry allows measurements of the real part of the refractive index $n_r(x) = 1 + 2\pi N_c \Gamma_r$ where $\Gamma_r = Re(\Gamma)$. Rearranging gives

$$\overline{a^3} N_c = \frac{n_r(x)-1}{2\pi} \left(\frac{\varepsilon+2}{\varepsilon-1}\right) \tag{3.6}$$

Combining Eqs. 3.5 and 3.6 yields an effective cluster radius $a_{eff} \equiv (\overline{a^6}/\overline{a^3})^{1/3}$ and number density $N_{c,eff} \equiv \overline{a^3} N_c / a_{eff}^3$ [155].

The above model assumes complete clustering. If the jet contains a monomer fraction $\delta_m = N_m/(N_m + N_C\overline{n_c})$ where N_m is the monomer density and $\overline{n_c}$ is the average number of atoms in the cluster, the assumption of complete clustering causes an underestimation of a_{eff} by a factor $(1-\delta_m)^{-1/3}$ [155]. The underestimation arises from the additional contribution of the monomers to the measured phase shift while contributing negligibly to the Rayleigh scattered signal. The cube root dependence greatly reduces the effect of the uncertainty in δ_m since even an assumption of 95% monomers only increases the calculated a_{eff} by a factor of 2.7. Further, the effect of the cluster size distribution on a_{eff}can be calculated by comparing $a_{eff} \equiv (\overline{a^6}/\overline{a^3})^{1/3}$ to $\bar{a}$ for various cluster size distributions, $f(a)$, where $\overline{a^n} = \int_0^\infty a^n f(n_c) dn_c$ and $a = r_{WS} n_c^{1/3}$with r_{WS} the intra-cluster Wigner-Seitz radius. Using a log normal distribution for the number of molecules per cluster, we find that this method will tend to overestimate the cluster size. However, if the distribution is sufficiently narrow that the standard deviation is within 40% of the mean, then the retrieved cluster size, a_{eff}, will be correct to within a factor of 2.

Rayleigh scattering is collected from the cluster jet by focusing a 25 mJ, ~10 ns beam derived from our Ti:Sapphire system ($\lambda = 800nm$) into the thin jet at f/9.5. A calibrated imaging system collects the scattered signal in a plane perpendicular to the pump polarization and images the signal onto a CCD camera. The experimental setup and a raw image of the Rayleigh scattered light are shown in Fig. 3.1. The same transverse interferometry diagnostic described in section 3.3 was used to measure the clustered gas refractive index.

The hydrogen cluster size and density are found to vary as a function of the beam height above the nozzle orifice. Near the orifice, where the hydrogen molecule density is highest, negligible Rayleigh scattering was detected. A stronger Rayleigh scatter signal was observed farther from the nozzle, consistent with cooling-induced clustering as the gas expands into the vacuum. Figure 3.6 shows the cluster size and density as a function of radial position at various heights above the 150 μm diameter nozzle with a jet backing pressure of 1000 psi and reservoir temperature −160° C. The minimum average cluster radius measured for any conditions was approximately 0.5 nm limited by the sensitivity of the Rayleigh scatter diagnostic.

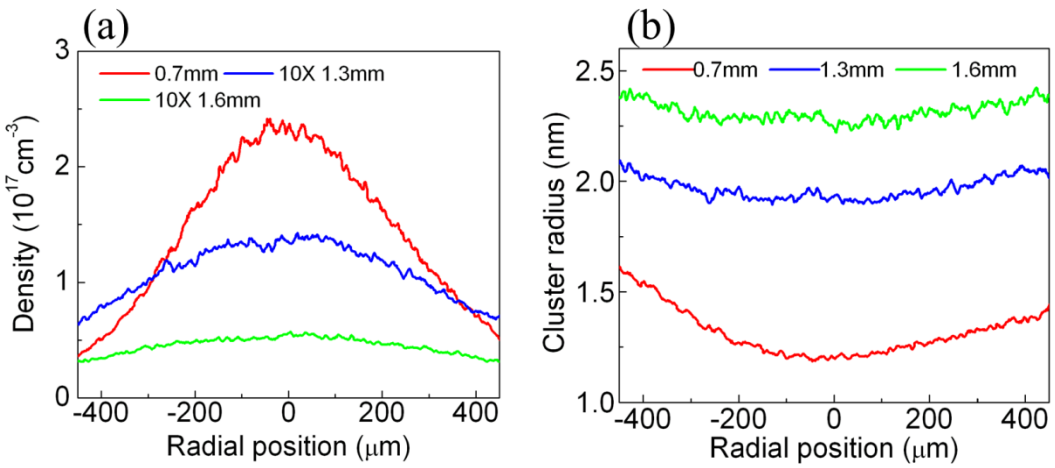

Figure 3.6. Average cluster density (a) and average cluster size (b) as a function of radial position at various heights above the 150 μm diameter nozzle orifice at jet backing pressure and temperature 1000 psi and -160° C.

At positions greater than approximately 500 μm above the orifice, the cluster size is measurable and the dependence of clustering on jet backing pressure and reservoir temperature can be determined. Figure 3.7(a) shows the nonlinear dependence of the spatially integrated Rayleigh scatter signal on jet backing pressure at a height 1 mm above the 150 μm nozzle when the jet reservoir temperature is held at –160° C. Figure 3.7(b) shows the cluster size (dotted line) and density (solid line) at the same position as a function of backing pressure. The effective cluster radius dropped rapidly as the valve temperature was increased. For 1050 psi backing pressure and –160° C valve temperature, the average cluster radius 1 mm above the 150 μm orifice was ~1.8 nm. At –140° C the cluster radius dropped to ~0.5 nm for the same backing pressure. Above –140° C the cluster size was below the 0.5 nm measurement threshold.

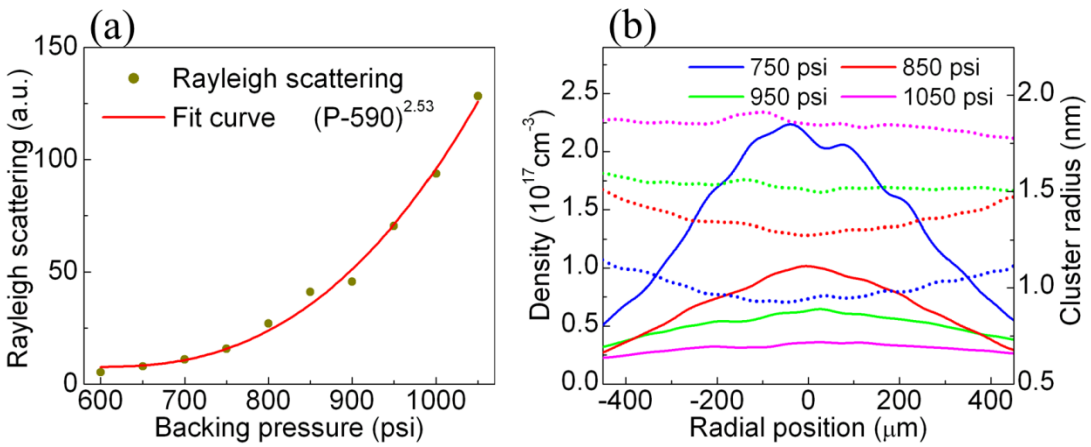

Figure 3.7. Rayleigh scattered signal versus backing pressure (a) and cluster density (solid line) and size (dotted line) at a height ~1 mm above the 150 μm nozzle (b) with the jet reservoir held at −160° C.

3.6 Nozzle geometry

For the isentropic flow discussed in section 3.2 one can drive the relation between the nozzle area and the local Mach number

$$\frac{A}{A_{th}} = \frac{1}{M}\left(\frac{2}{\gamma+1}\left(1+\frac{\gamma-1}{2}M^2\right)\right)^{\frac{\gamma+1}{2(\gamma-1)}} \tag{3.7}$$

Here A_{th} is the nozzle diameter at the throat where $M = 1$. Assuming isentropic flow, for a prescribed nozzle profile, Eq. 3.7 yields the Mach number along the flow direction which in turn determines the other local thermodynamic properties of the flow including the density [172]. For an increasing cross sectional area A after the throat, the Mach number along the flow direction increases, resulting in a supersonic flow with lower density. Supersonic nozzles generate sharper flow boundaries than sonic nozzles, a feature of interest for many laser plasma interaction experiments.

In addition to straight capillary nozzles, we have employed precision tapered nozzles in newer versions of the high density gas jet. For a converging nozzle with

~12 degree taper angle and $100\mu m$ throat diameter at the nozzle tip, the resulting density profile is very similar to the density from a straight nozzle with the same inner diameter as the throat size. This is expected as the Mach number cannot exceed $M = 1$ in a converging nozzle. However, in the case of diverging geometry, Eqs. 3.1 and 3.7, result in supersonic flow with lower density at the nozzle exit than a sonic nozzle. Figure 3.8 compares the flow from a straight capillary and a diverging nozzle with ~7 degrees diverging angle, both with 100μm throat diameter and similar stagnation condition. The diverging nozzle has a smaller density near the tip, but it expands much slower in the transverse direction and has sharper boundaries.

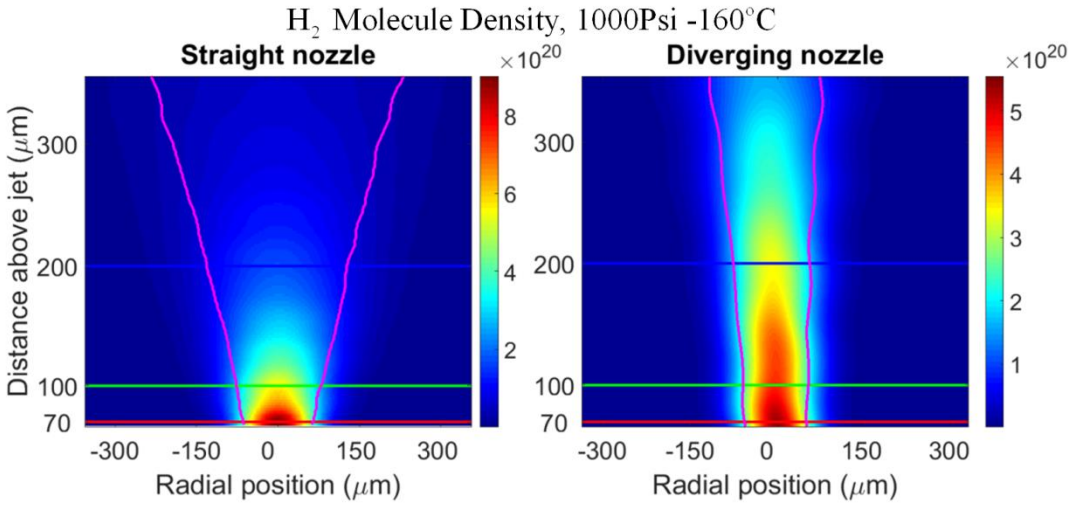

Figure 3.8. Comparison of straight (left) and diverging nozzle (right). The magenta lines show the FWHM density region, illustrating slower transverse expansion for the diverging nozzle.

3.7 Conclusions

In this chapter, a jet design based on a cryogenically cooled pulsed solenoid valve was described. The jet was shown to be capable of reaching hydrogen

molecule densities as high as $9 \times 10^{20} cm^{-3}$ in a ~200 μm FWHM Gaussian density profile when the jet was backed with 1000 psi and cooled to −160° C. When fully ionized, this brings the peak plasma density above the (non-relativistic) critical density for Ti:Sapphire lasers, making this jet an interesting target for electron and ion acceleration experiments.

Estimates of the output density scaling with valve backing pressure and temperature were made by modeling the gas flow through the nozzle as steady and isentropic. Reaching the highest density output possible was found to require a sonic nozzle design, with the output molecular density directly proportional to the density within the valve reservoir. The equation of state prediction, that gas density at the nozzle exit scales as T_0^{-1}, is borne out by our measurements of cryogenically cooled jets, which yield a density scaling of $T_0^{-0.87}$.

Rayleigh scattering measurements showed that clustering of the high density gas occurs at distances ~500 μm and greater above the nozzle orifice. Average hydrogen cluster radii of >~1 nm were measured approximately 1 mm above the nozzle for the highest backing pressures and coldest reservoir temperatures. The cluster size measurements show that clustering is negligible in experiments operating near the nozzle exit plane where the gas density is highest.

Chapter 4: MeV electron acceleration at 1 kHz with 30fs, <10mJ laser pulses

4.1 Introduction

Laser-driven electron acceleration in plasma has become a well-established field since it was proposed several decades ago [6]. In recent years, significant experimental successes have been achieved, including the acceleration of quasi-monoenergetic electron bunches to ~4 GeV [12] and the generation of MeV range gamma rays [14]. Typically, these experiments, demand laser pulse energies of at least several joules, and consequently existing laser technology limits them to low repetition rates (≤10 Hz).

There are numerous applications for MeV-scale electron beams where a compact and portable high-repetition-rate source is beneficial, especially for potential scanning purposes and improved data collection statistics. At low pulse repetition rates of ≤10 Hz, radiography using broadband, moderately divergent laser-plasma-accelerated electron beams from gas jets [16,173], or γ rays from Bremsstrahlung conversion of the beam [15,174] has been demonstrated. Prior work at 0.5kHz using a continuous flow gas jet has produced ~100 keV, 10 fC electron bunches [175] and demonstrated their application to electron diffraction experiments [176]. While high repetition rate acceleration of ~pC electron bunches to MeV-scale using solid and liquid targets has been reported counter propagating to the laser [177,178], gas jet-based laser-plasma electron sources had yet to simultaneously achieve high repetition rate and forward directed MeV-scale energies.

In non-plasma based work, time-resolved electron diffraction using laser-driven photocathodes and conventional MeV accelerator structures such as LINACs is an established research area [179], where low emittance and narrow energy spreads are achieved. For <100 fs temporal resolution, this technique requires compensation for space charge effects and timing jitter [12].

The most common and successful laser-plasma-based acceleration scheme is laser wakefield acceleration (LWFA), which can be initiated by relativistic self-focusing of the laser pulse in the plasma. LWFA electron pulses can be ultrashort and are precisely timed to their driving optical pulses [18]. Relativistic self-focusing has a critical power [51] of $P_{cr} = 17.4(N_{cr}/N_e)$ GW, where N_e is the plasma density and N_{cr} is the critical density. As $N_{cr} = 1.74 \times 10^{21}\text{cm}^{-3}$ for the Ti:Sapphire laser wavelength of λ=800nm, a very high N_e is needed to keep P_{cr} well below 1 TW and enable operation with current commercial laser technology for millijoule-scale pulses at 1 kHz. In previous experiments, we showed using a high density gas jet (at $N_e/N_{cr} <$ 0.25) lowers P_{cr} sufficiently to promote relativistic self-focusing and SM-LWFA with sub-terawatt laser pulses [21]. In those experiments, electron beams with ~0.5nC charge per bunch at >1 MeV energies were accelerated using <50mJ laser pulses from a 10 Hz laser system. The electron acceleration from the high density target is accompanied by a broadband radiation flash emitted from the electrons injected into the accelerating phase of the plasma wave by the laser field [180]. Figure 4.1 shows a shadowgraph of a laser pulse interaction with the high density jet target, along with a forward and a sideways collected spectrum from the interaction region. The bright spot in panel (a) shows the sideways-collected injection radiation flash, and panel (c)

shows the spectrum of the flash from a target region with maximum electron density of $N_e = 3.4 \times 10^{20} cm^{-3}$. The forward collected spectrum of a laser pulse with vacuum normalized vector potential $a_0 \simeq 0.8$, focused on a region of the jet target with peak electron density of $N_e = 1.8 \times 10^{20} cm^{-3}$is depicted in Fig. 4.1(b). The broadband redshifted Raman Stokes radiation peak at $\lambda_s = 2\pi c/\omega_s \simeq 1030nm$ is evidence for self-modulation, and implies strong self-focusing of the laser pulse. Using the plasma frequency $\omega_p$for the measured electron density, and $\omega_s = \omega - \frac{\omega_p}{\gamma^{1/2}}$, where ω is the laser frequency, and $\gamma = (1 + a_0^2/2)^{1/2}$ is the relativistic factor, the estimated self-focused normalized vector potential is $a_0 \simeq 2.7$, which is in good agreement with the peak a_0 from 3D PIC simulations.

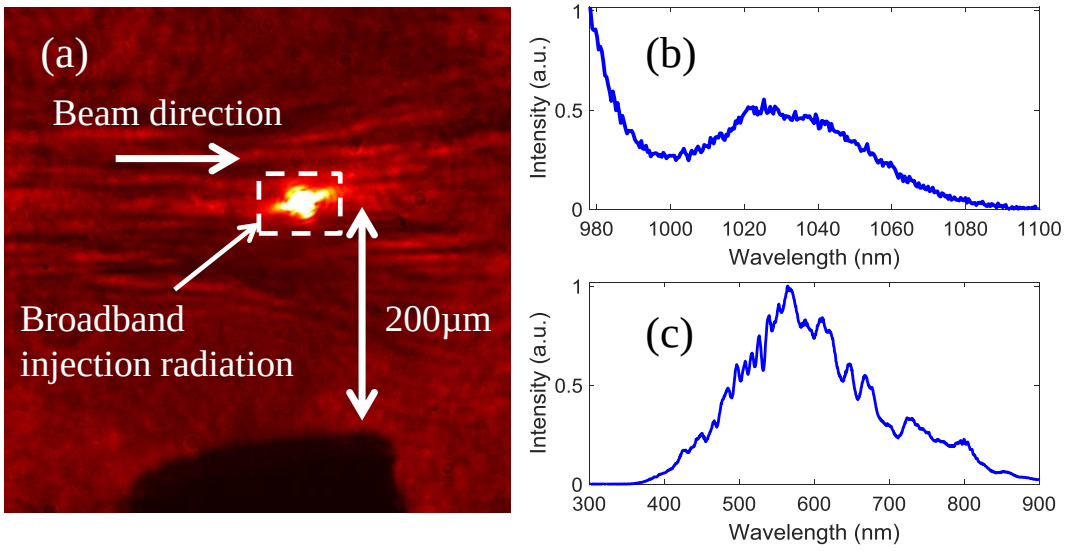

Figure 4.1. (a) Shadowgraphic image of the laser pulse interaction with high density jet target, along with a (b) forward collected spectrum showing Raman Stokes radiation, confirming self-modulation of the laser pulse, and (c) the spectrum of sideways-collected broadband radiation from laser assisted injection.

Here, we show that using gas jets approaching even closer to critical density ($N_e/N_{cr} < 0.69$) makes possible electron acceleration to relativistic energies with pulse energies as low as 1.3 mJ, delivered at 1 kHz. We note that for pulse propagation near $N_e/N_{cr} = 0.25$, the stimulated Raman scattering associated with SM-LWF generation can compete with the two-plasmon decay instability [181]. To help understand the details of acceleration in this regime, we present particle-in-cell (PIC) simulations in this chapter.

Driving laser plasma accelerators at high repetition rate using a gas jet target demands a nearly continuous flow out of a high-pressure nozzle. This leads to high background chamber pressure, which can enhance the deleterious effects of laser-induced ionization and defocusing well before the pulse encounters the gas jet. Our experiments demonstrate electron acceleration at chamber background pressures as high as 20 Torr, enabling the use of continuous flow nozzles and even higher repetition rate laser systems for LWFA.

4.2 Experimental setup

We used $\lambda = 800$ nm, 30 fs, < 12 mJ pulses from a 1 kHz Ti:Sapphire laser to drive LWFA in the dense jets. The pulses were tightly focused with an f/8.5 off-axis paraboloid to a 9 μm intensity FWHM spot size. Given the risk of high accumulated gamma radiation dose from running the experiment at 1 kHz (mainly from the beam dump), we used a solenoid valve before the nozzle to control the gas flow duration from less than 1 ms up to several minutes. The interaction of the laser pulse with the high density jet generates strong supercontinuum. Figure 4.2 (left panel) shows the

laser interaction with the gas jet, also showing the solenoid valve and the cooling assembly used to bring the backing gas temperature down to $-160^{\circ}C$. The right panel shows the bright, forward directed supercontinuum on a screen.

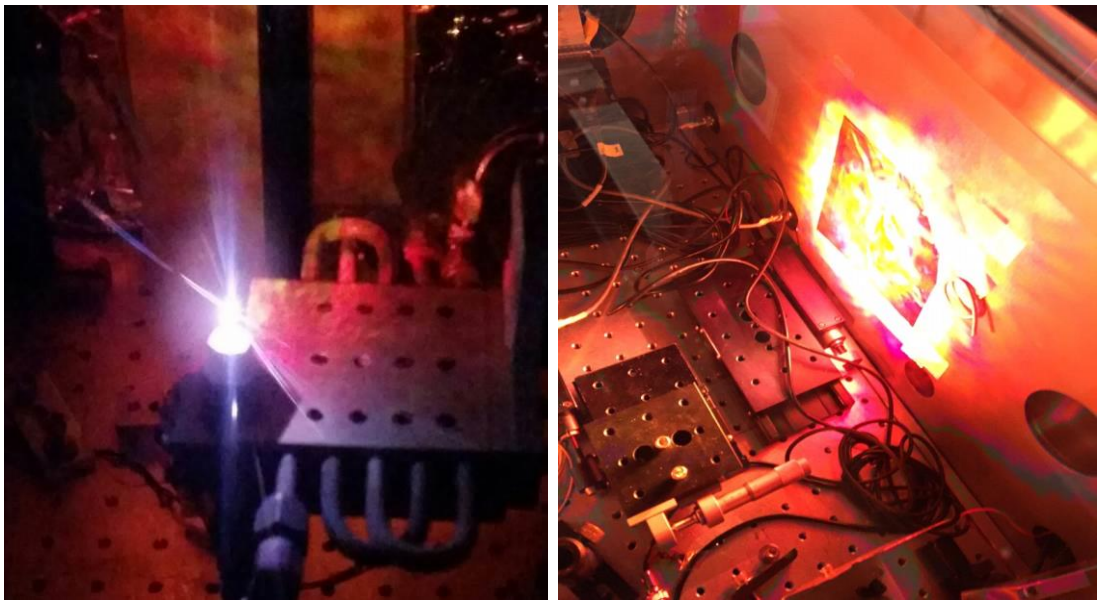

Figure 4.2. Solenoid valve and the cooling assembly (left) at the moment laser interacts with high density jet, and the resulting bright supercontinuum (right).

A schematic drawing of the experimental setup along with a measured He gas density profile, an accelerated electron beam profile, and its corresponding electron energy spectrum is shown in Fig. 4.3.

Gas jet density and plasma profiles were measured using folded wavefront interferometry [182] with a λ = 800 nm probe split from the main pulse. High density H_2 and He gas jets were produced by cooling the gas to −150˚C at 1100 psi, and flowing the gas through a 150 μm nozzle into a vacuum chamber pumped by a 220CFM roots blower. The gas jet density encountered by the laser pulse was controlled by changing the backing pressure, temperature, and the location of the laser focus on the jet. As determined from interferometry, the jet density has a

Gaussian transverse profile of FWHM 150-250 μm depending on the laser focus position. Within ~60 μm of the nozzle exit, we achieve $N_e/N_{cr} \sim 1$ at full ionization.

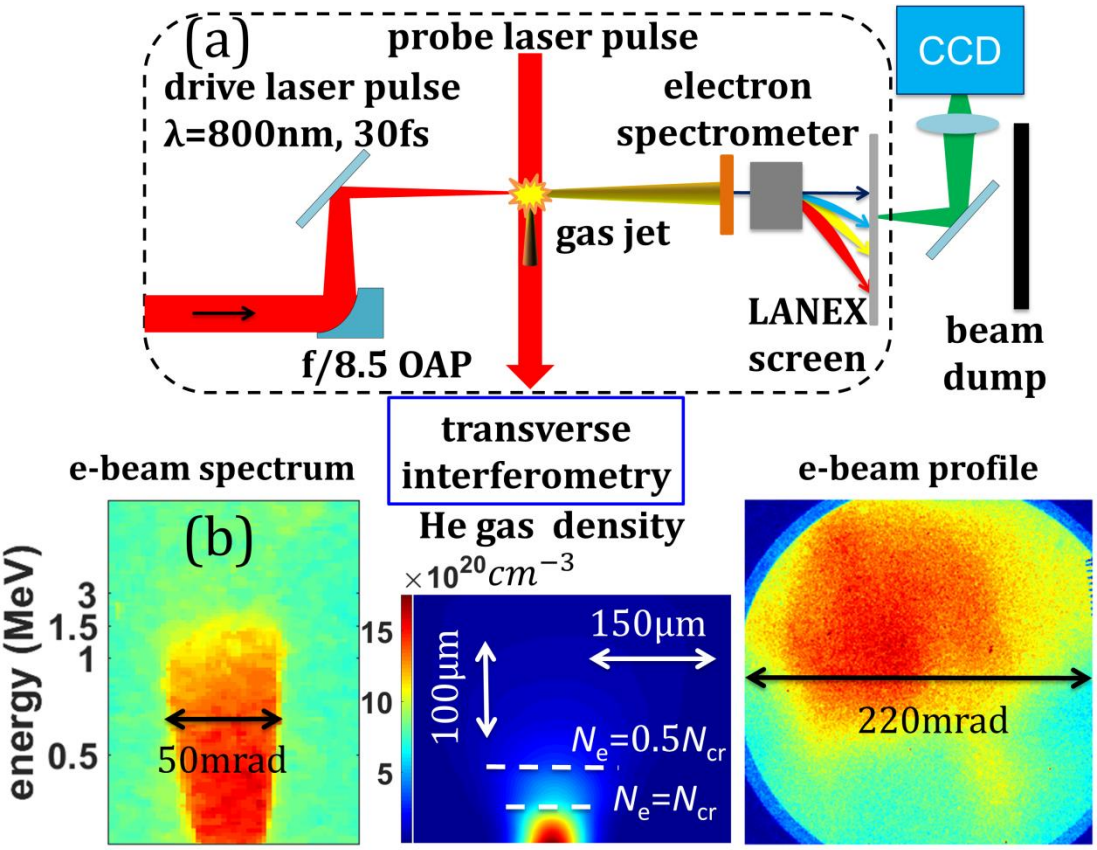

Figure 4.3. (a) Experimental setup for high-repetition-rate electron acceleration. The dashed line depicts the vacuum chamber boundary. (b) Measured density profile for He gas jet (center), electron beam profile from He jet (right), and corresponding electron energy spectrum (left). The sharp left-right edges on the spectrum are from electron beam clipping on the spectrometer magnet.

To avoid nozzle damage, the laser was focused at least 110 μm above the nozzle orifice, where $N_e/N_{cr} \sim 0.5$. Accelerated electron spectra were collected 35 cm beyond the jet by a magnetic spectrometer consisting of a compact permanent 0.08 T magnet located behind a 1.7 mm wide copper slit, followed by a LANEX scintillating screen imaged onto a low noise CCD camera. Day-to-day experimental runs for

similar jet opening times gave slightly varying electron bunch energies and charges owing to gas jet nozzle tip erosion from plasma ablation. Nozzles were replaced after approximately 2×10^5 laser shots.

4.3 Experiment results

Figure 4.4 shows accelerated electron spectra from the H_2 jet for several values of laser pulse energy and with 10 ms valve open time. The inset shows the total charge per shot accelerated to >1 MeV energy versus laser pulse energy. Each point is the average of 10 consecutive shots. The exponential electron spectra and the moderately collimated beams are evidence of SM-LWFA, reflecting acceleration from strongly curved plasma wave buckets and wave-breaking electron injection into a range of accelerating phases [21]. Lowering the laser pulse energy requires increasing the electron density to maintain $P > P_{\mathrm{cr}}$. The minimum electron density required to observe electron acceleration with 9 mJ pulses was $4.0 \times 10^{20}\ cm^{-3}$($N_e/N_{cr}$= 0.23). To observe acceleration for 1.3 mJ pulses, it was necessary to increase the electron density to $1.2 \times 10^{21}\ cm^{-3}$($N_e/N_{cr}$= 0.69).

At low laser pulse energies (< 3mJ) with H_2 jets, most of the electrons are at energies below our spectrometer range. Moving the spectrometer out of the electron beam path allows the full beam to impact the LANEX (shielded by 25 μm aluminum foil). Using the electron transmission data for aluminum [183] and the LANEX response [184,185], we estimate electron bunches of ~10 fC charge with up to ~0.5 MeV energy for laser pulse energies as low as 1.3 mJ.

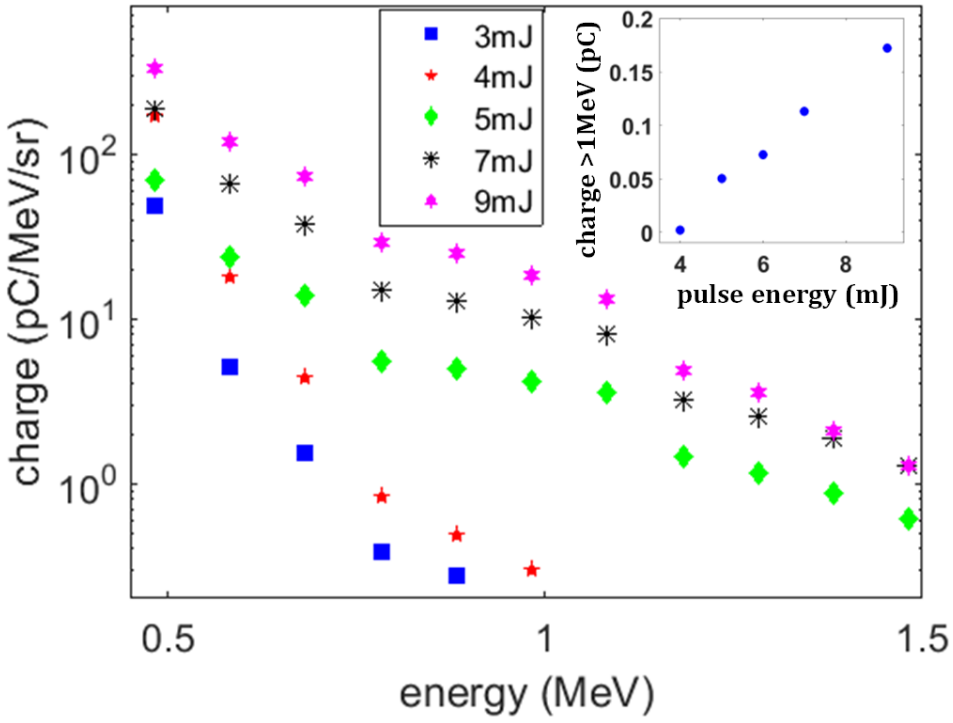

Figure 4.4. Accelerated electron energy spectra from H_2 jets for varying laser pulse energy and 10 ms gas jet open time. The inset shows total charge with > 1MeV energy versus laser pulse energy. The ±0.05 MeV energy bins correspond to the magnetic spectrometer's coarsest energy resolution (at 1.5 MeV).

Using He jets no electron beams were detected for laser pulses <5 mJ. For both H_2 and He jets, increasing the pulse energy to ~10 mJ increased the bunch charge with >1 MeV energy to ~ 1pC. We attribute these observations to ionization-induced defocusing in He at low laser pulse energy. The transverse electron density profile in the H_2 jet is flatter than in the He jet owing to lower threshold for full ionization in H_2 [186], resulting in less defocusing in H_2 and larger amplitude plasma waves. This is borne out by interferograms in Fig. 4.5(a), showing the residual plasma ~1 ps after interaction of a 5 mJ pulse with the He and H_2 jets. The associated 2D PIC simulations using the code TurboWave [46] show the electron density

profiles just before and 250 fs after plasma wavebreaking in the H_2 and He jets in Fig. 4.5(b). It is seen that the hydrogen plasma profile is fully ionized over a wider region than in He, and that post-wavebreaking scatter of the laser pulse and electron heating in hydrogen gives a wider profile at the jet exit.

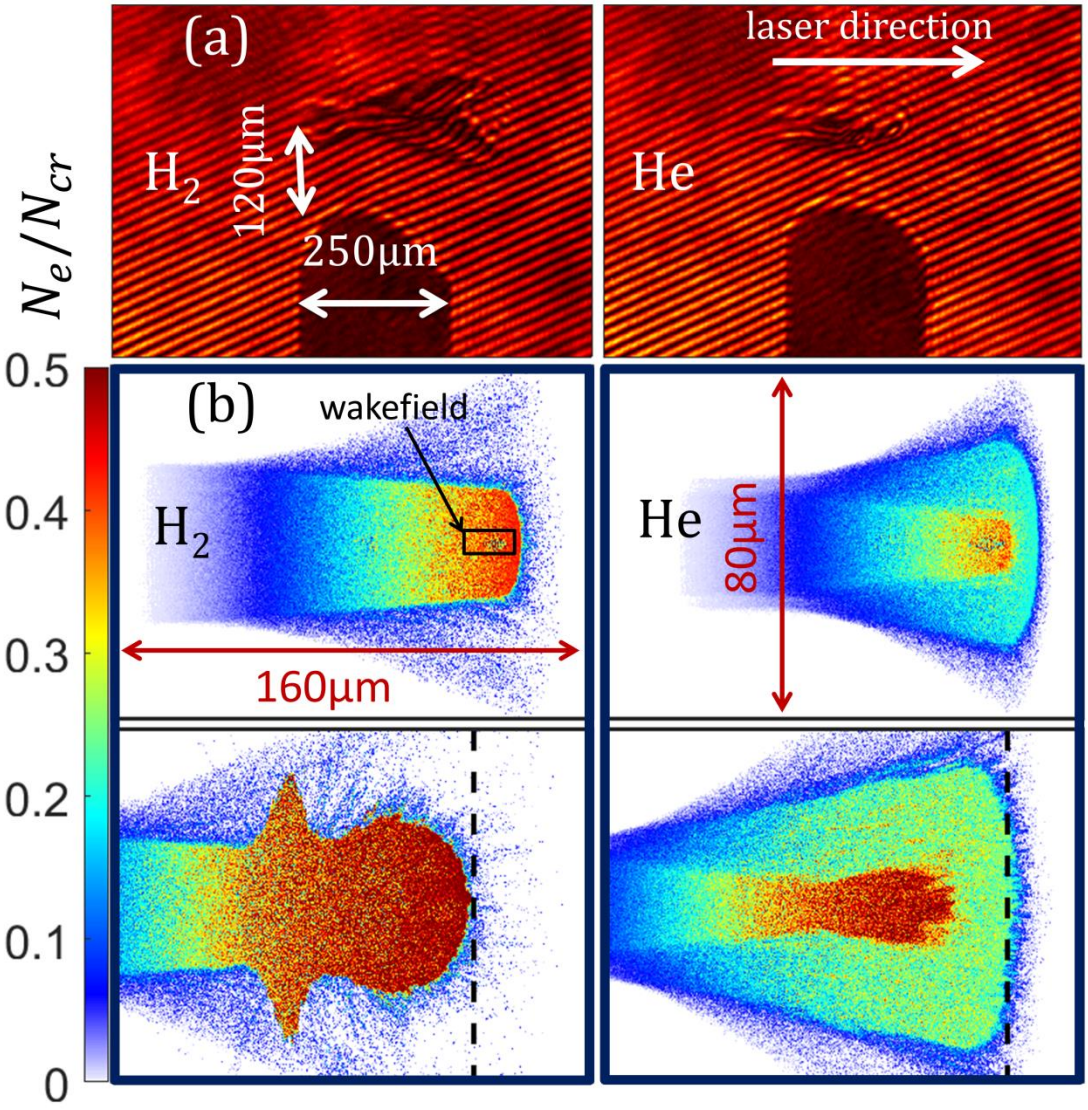

Figure 4.5. (a) Interferograms showing residual plasma ~1 ps after interaction of 5 mJ pulses with H_2 and He gas jets. The dark shadow is the gas nozzle. (b) Electron density profiles before (top) and 250 fs after wavebreaking (bottom) from 2D PIC simulations of the interaction of 5 mJ, 30 fs laser pulses with 200 μm FWHM H_2 and He jets at peak neutral density 4.35 $\times 10^{20}$ molecules or atoms per cm^3. The dashed vertical lines indicate the center of the gas jet.

Figure 4.6 shows accelerated electron spectra for varying peak electron density from the He jet using 9.5 mJ pulses and a 20 ms valve open time. Corresponding total charge accelerated to > 1 MeV is shown in the inset.

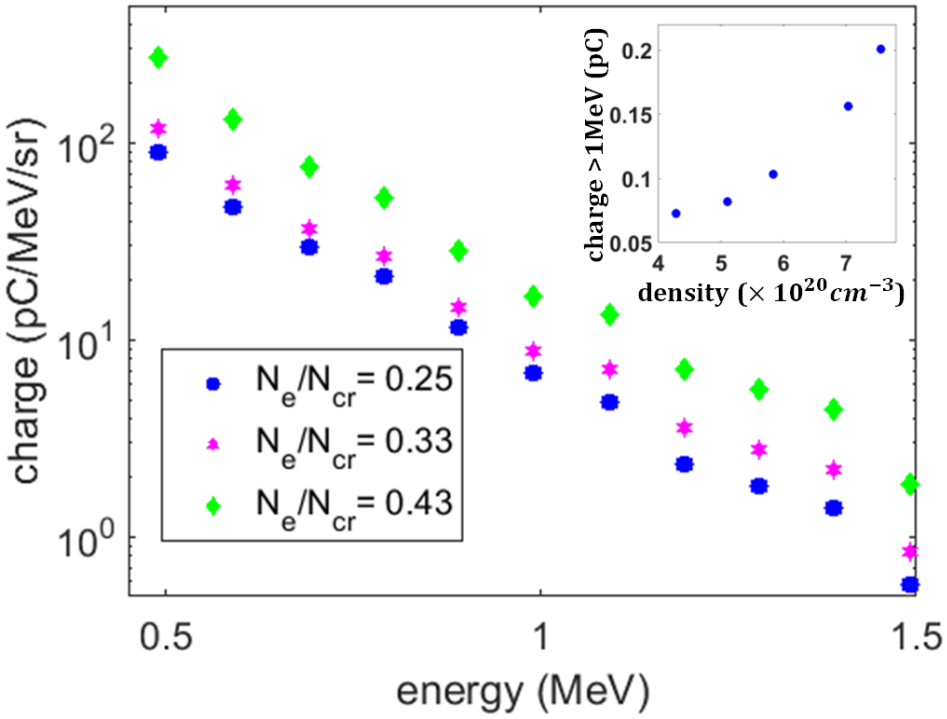

Figure 4.6. Electron energy spectrum for varying plasma density from He jet using 9.5 mJ laser pulses and 20 ms gas jet open time. The inset shows the total charge per shot with > 1MeV energy.

Figure 4.7 shows electron beam profiles on LANEX for selected He plasma densities of Fig. 4.6, showing the sensitivity to plasma density. While the total accelerated charge increases significantly with peak electron density, the normalized electron spectrum does not change noticeably. The beam divergence angle (estimated from an average around the 50% beam intensity contour) is ~150 mrad at N_e/N_{cr} = 0.25 and increases to ~260 mrad as the electron density is increased to N_e/N_{cr}= 0.43.

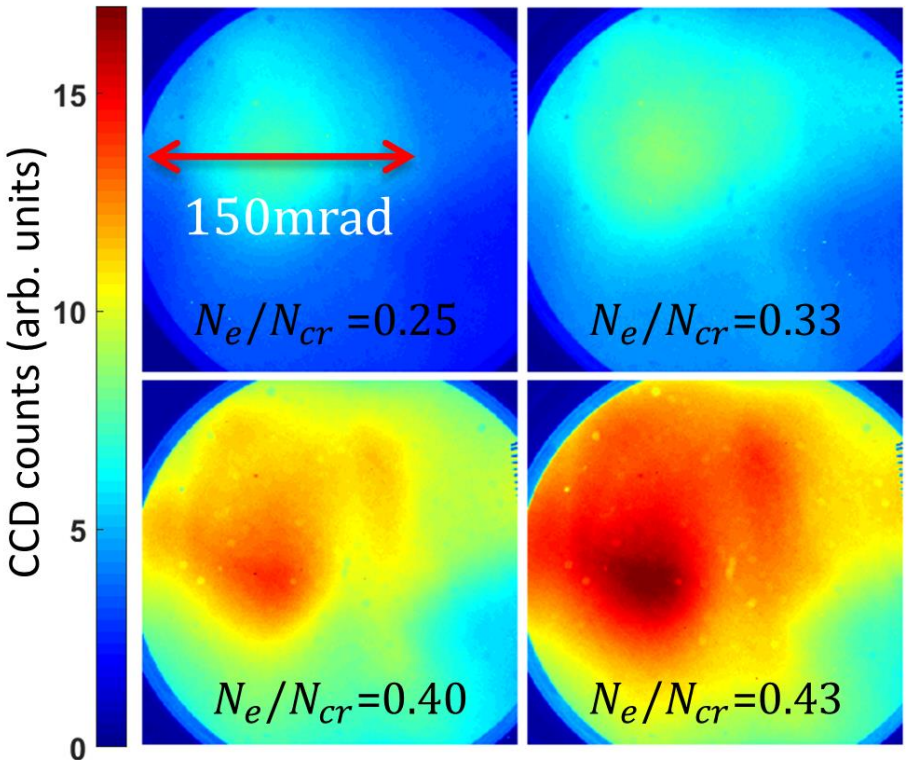

Figure 4.7. Electron beam profiles on LANEX screen, illustrating sensitivity to plasma density. The outside circle is the outline of the vacuum port, through which the LANEX surface was imaged.

A major concern using a high density continuous flow gas jet is the background pressure buildup inside the target chamber, which can lead to ionization-induced defocusing of the pulse. In order to study the effect of background pressure buildup, we first measured accelerated electron spectra for increasing valve open times (with the laser at 1 kHz and the jet repetition rate at 0.5 Hz), as shown in Fig. 4.8, where a He gas jet at N_e/N_{cr} = 0.54 is driven by 10 mJ laser pulses. It is seen that increasing the valve open time lowers the charge per shot while keeping the normalized spectra similar. The charge per shot at > 1 MeV decreases from ~1.6pC to ~0.2pC as the opening time increases from 1 to100 ms, over which the corresponding background pressure increases from < 0.1 to ~ 3.5 Torr.

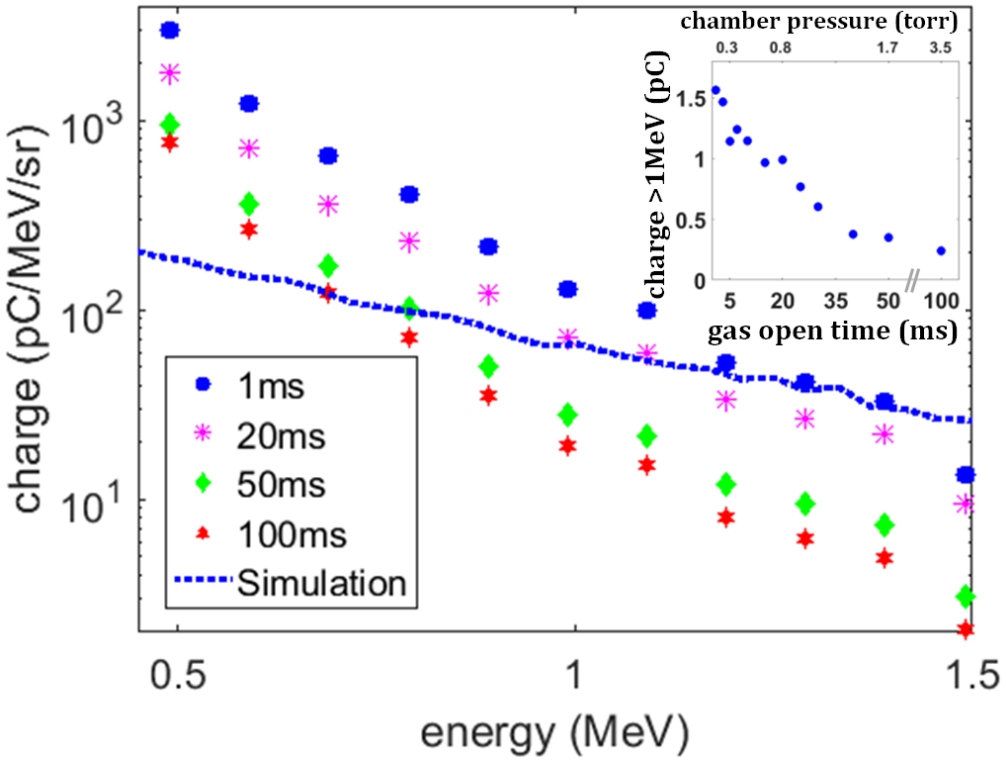

Figure 4.8. Electron energy spectrum per shot from He gas jet (N_e/N_{cr}= 0.54) for different valve open times for 10 mJ laser pulses at 1 kHz. Inset: total charge per shot accelerated to > 1MeV and corresponding background pressure. The dashed blue line shows the spectrum (×0.1) from a 3D PIC simulation of one shot for N_e/N_{cr}= 0.5 and 10 mJ.

Increasing the valve open time to 1s, with a repetition rate of 0.5 Hz, increases the background pressure to a constant ~20 Torr. Scanning a 50 ms window (containing a 50 shot burst of 10 mJ pulses) over the 1 s valve opening of the He jet gives a nearly unchanging LANEX signal. This shows that the valve could be open continuously if the accumulation of gamma-ray dose from our beam stop was not a constraint.

4.4 PIC simulations

To better understand SM-LWF generation and acceleration in our jet at N_e/N_{cr} > 0.25, we performed 2D PIC simulations for 4 mJ laser pulses interacting with a 200 μm FWHM preionized H_2 target with peak N_e/N_{cr} = 0.5. Figure 4.9 shows the simulated plasma wake before and after wavebreaking (top) and corresponding central lineouts (bottom) of electron density and normalized laser vector potential a_0. The wakefield is generated at ambient plasma density above quarter critical (dashed line), where the Raman Stokes line is suppressed and the anti-Stokes line dominates, as seen in the forward directed optical spectrum shown. Two-plasmon decay is not evident over the full laser propagation, possibly due to the strongly nonlinearly steepened density in the plasma wake [187].

For our prior experiments at high density, PIC simulations showed that both LWFA and direct laser acceleration (DLA) contributed to electron energy gain, with LWFA dominating at lower laser pulse energies [15]. For the current experiments with ≤ 10 mJ pulses, PIC simulations show that LWFA dominates DLA up to the highest plasma densities used. The simulations also show that the leading part of electron bunch is 30-60 fs FWHM for our range of laser and plasma conditions, followed by a longer (>100 fs) low energy tail. The simulated spectrum, shown in Fig. 4.8, indicates approximately 10 × more charge than measured, along with a higher effective temperature than in the experimental spectra, differences we are currently trying to resolve.

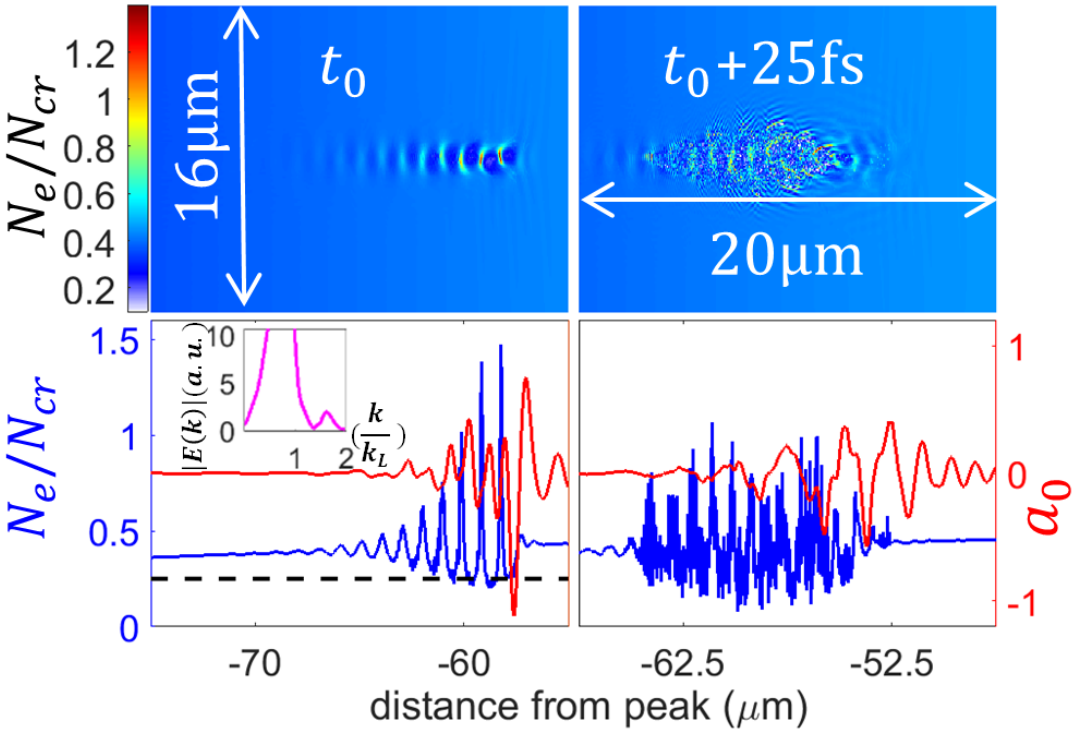

Figure 4.9. Simulated plasma wake just before and after wavebreaking (top) and corresponding central lineouts (bottom) of density and normalized laser vector potential, for 4 mJ pulse interacting with 200 μm FWHM preionized H_2 target of peak N_e/N_{cr} = 0.5. Dashed line: N_e/N_{cr} = 0.25. Inset: Pre-wavebreaking spectrum of self-modulated laser showing anti-Stokes line, with Stokes line suppressed.

4.5 Pulse shape and chirp effect

Studies on the effect of chirp sign of the driving laser pulse on wakefield acceleration suggest laser pulses with positive chirp lead to higher bunch charge than a negative chirp with the same energy and pulse duration [188–190]. The asymmetry in the charge, for pulses with equal energy and duration and opposite chirp sign, is mainly attributed to the asymmetry in the pulse shape (skewness) originating from uncompressed higher order phase. The skewness of the pulse from higher order phase results in faster rise time for a positively chirped pulse, which enhances the forward

Raman scattering and self-modulation, and in turn, leads to larger electron yield [191]. At near critical plasma densities, the group velocity dispersion in plasma becomes more important, stretching the pulses with negative chirp, and compressing the pulses with a positive chirp. In our experiments at near critical densities, stretching the pulse length to ~100fs with positive chirp generates electron beams comparable to the shortest pulse case (30fs), whereas the electron beams from negatively chirped laser pulses vanishes at these pulse durations. Figure 4.10 compares the electron beam profile for three different pulse duration and chirp signs. As we will discuss in Chapter 5 the plasma GVD effect becomes significantly more important when opposite sign chirp is introduced to few-cycle driver pulses [192].

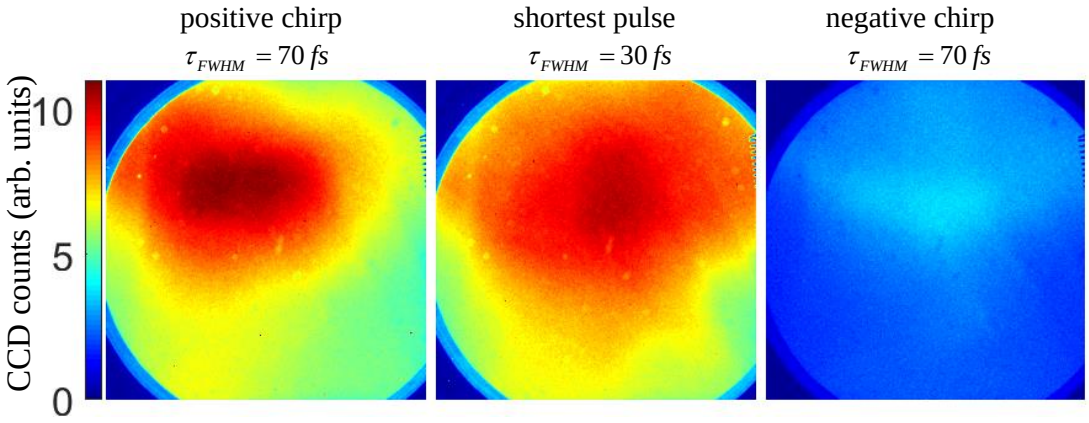

Figure 4.10. Electron beam dependence on initial pulse duration and chirp of the pulse. Positively chirped pulses lead to significantly higher charge than negatively chirped pulses with the same duration.

4.6 Conclusion

In summary, we have demonstrated for the first time, to our knowledge, laser-driven electron acceleration to > 1MeV in a gas jet using a 1 kHz repetition rate mJ-

scale laser, with bunch charge to the pC level. This result was made possible by the use of a thin, dense, gas jet target enabling near-critical density laser interaction. The energy spread and the beam divergence of these electron bunches are rather large, and further improvement in beam quality is required for many applications. In Chapter 5 we will discuss how the use of few-cycle pulses in near critical density targets helps to generate higher quality electron bunches.

Chapter 5: Acceleration of quasi-monoenergetic electron bunches to 5 MeV at 1 kHz with few-cycle laser pulses

5.1 Introduction

As we discussed in Chapter 4, our experiments with 30fs laser pulses showed that use of a near-critical density gas jet target lowers the critical power for relativistic self-focusing sufficiently to enable MeV-scale electron acceleration with ~1mJ energy scale driver pulses from high repetition rate laser systems [20]. However, those electron bunches, accelerated in the SM-LWFA regime [55], had an exponential (thermal-like) energy distribution and a rather large divergence angle.

In this chapter we show that using ~7fs FWHM duration, ~2.5mJ energy drive pulses generated through a hollow core fiber (HCF)-based compressor, we can access the "bubble" regime and accelerate MeV scale quasi-monoenergetic electron bunches with low divergence from near-critical density gas targets. To show these results in advance, Fig. 5.1 compares the electron bunch energy spectra and beam profiles from the bubble and SM-LWFA regime experiments. Even though the drive laser pulse has ~4× lower energy in the bubble regime, its accelerated electron bunch has significantly higher energy than in the SM-LWFA experiments and a ~10× smaller divergence.

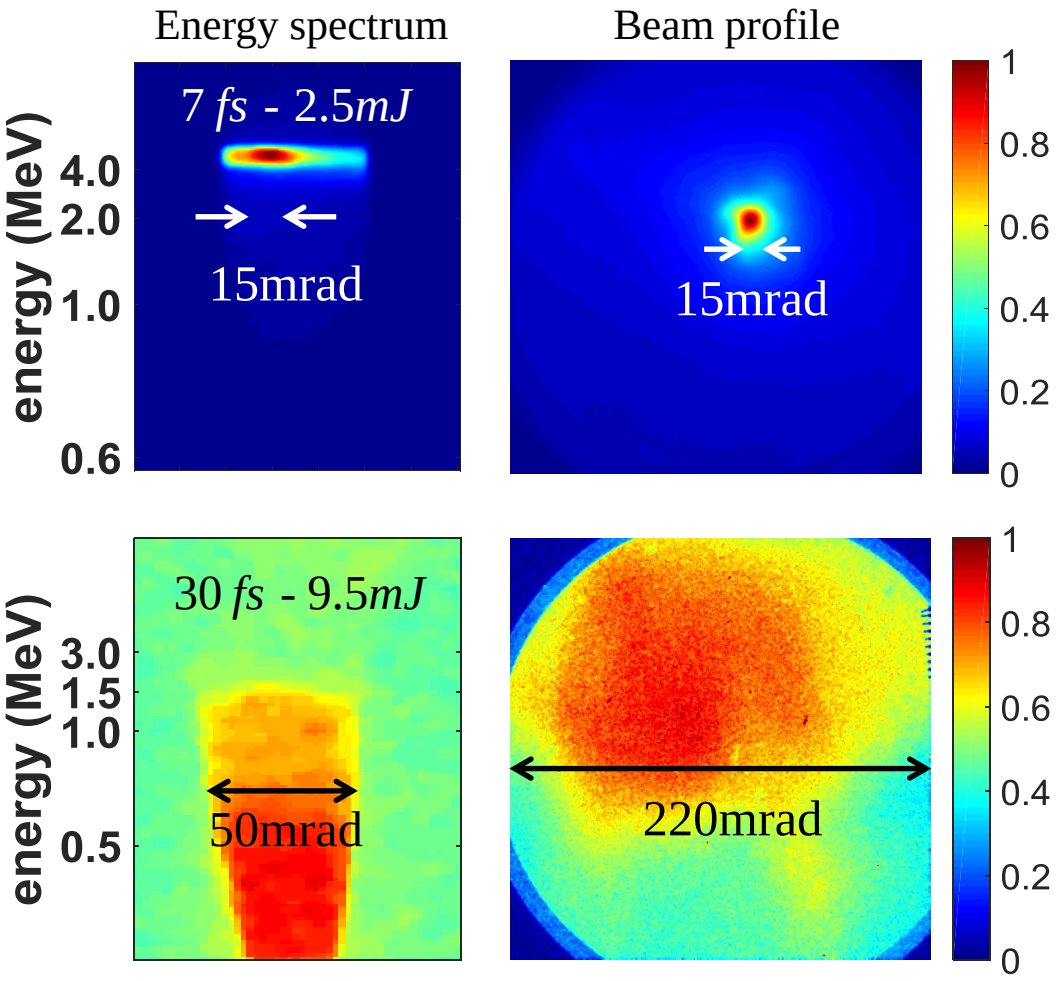

Figure 5.1. Electron bunch energy spectrum and beam profile for LWFA operated in the bubble regime (top), and in the SM-LWFA regime (bottom). The bubble regime leads to significantly higher electron beam quality in terms of peak energy, energy spread, and beam divergence angle.

Our SM-LWFA experiments described in Chapter 4 are similar, in principle, to the initial high laser pulse energy LWFA experiments of more than two decades ago [193–196]; our recent advance is that we enabled the use of mJ-scale lasers drivers by using near-critical gas jets. High density gas targets reduce the plasma wavelength and lower the critical power for relativistic self-focusing, making possible

the relativistic acceleration of electrons in the SM-LWFA regime with far lower energy laser pulses [20,21,197].

A significant breakthrough in laser wakefield acceleration occurred more than a decade ago when quasi-monoenergetic electron bunches were generated by operating in the highly nonlinear "bubble" regime [9–11]. In the bubble regime, the laser pulse duration is shorter than plasma wavelength, and its intensity is high enough to expel all background electrons from the first wake trough behind the laser pulse, forming a cavity containing the laser pulse and devoid of plasma electrons. As the cavity propagates through the plasma with the laser pulse, some of the background plasma electrons are trapped at the back side of the cavity and accelerated. These electrons have a quasi-monoenergetic energy spectrum [198].

In order for significant acceleration in the bubble regime, the laser pulse should be relativistically self-guided up to the acceleration dephasing length. For such short resonant pulses, with durations shorter than the plasma wavelength ($c\tau_L < \lambda_p$), the leading edge will be eroded [40,41] while, for the correct choice of laser and plasma parameters, the main body of the pulse can self-guide several times the Rayleigh length [199,200]. For stable self-guiding in the bubble regime, the bubble cavity radius, which is almost equal to the laser beam spot radius w_0 at focus, should be matched to half the plasma wavelength, and in turn, matched to the pulse length [201]:

$$R \approx w_0 \approx \frac{\lambda_p}{2} \geq c\tau_L \qquad 5.1$$

Here R is the cavity radius, $w_0$is the laser beam spot radius, and $\tau_L$is the FWHM laser pulse duration. The optimal spot size for a given intensity in the bubble regime can be

approximated from the relation $k_p R \sim \sqrt{a_0}$, which is calculated by balancing the ponderomotive force of the laser pulse $k_p \nabla a_0^2/\gamma \sim a_0/(k_p R)$, with the electrostatic force from the ion cavity $\sim k_p R$. Here k_p is the wavenumber, and a_0 is the normalized vector potential of the laser pulse. The commonly used relation

$$k_p R \simeq k_p w_0 = 2\sqrt{a_0} \quad , \tag{5.2}$$

found from scaling arguments applied to the results of 3D particle in cell (PIC) simulations, leads to only slight oscillations in the laser spot size and the bubble shape as the laser pulse propagates through the plasma [52,202] and hence the self-guiding and the acceleration are more stable.

Two important length scales in LWFA, which also apply to the bubble regime, are the pump depletion length and the dephasing length. In the bubble regime, the energy transfer from the laser pulse to the plasma happens dominantly at the front of the pulse where the electron density is higher. This causes local pump depletion, and the front of the laser pulse etches back at an effective speed (in the frame of the pulse) $v_{etch} \simeq c\omega_p^2/\omega_0^2$ as it propagates through the plasma [199]. The etching speed is deduced from the 1D nonlinear wakefield equation, Eq. 1.15 in the $\gamma_p \gg 1$ limit [40,41,199]. Using the etch speed, the pump depletion length is estimated by [52]

$$L_{depl} \simeq \frac{c}{v_{etch}} c\tau = \frac{\omega_0^2}{\omega_p^2} c\tau \tag{5.3}$$

The etching of the front side of the laser pulse also reduces the phase velocity of the plasma wake to $v_\phi = v_g - v_{etch}$, which is slower than the group velocity v_g of

the driver pulse. Including the effect of etching, the LWFA dephasing length becomes [52]:

$$L_d \simeq \frac{c}{c - v_\phi} R \simeq \frac{2}{3}\frac{\omega_0^2}{\omega_p^2} R \qquad 5.4$$

For high efficiency acceleration, the depletion and dephasing lengths should be comparable, $L_{depl} \approx L_d$. By reducing the plasma wavelength, λ_p, through the use of higher density targets, and correspondingly focusing the drive laser pulse to smaller spot sizes, we can significantly lower the laser pulse energy E_L required for a given value of a_0 for bubble regime conditions: $E_L \propto \lambda_P^3 \propto \tau^3$ [203]. The initial experiments in the bubble regime [9–11] used $\geq 0.5\,J$ laser pulses of $\tau \sim 30 - 50 fs$ focused on gas targets with plasma density $N_e \sim 0.01 N_{cr}$, where N_{cr} is the critical density corresponding to the drive pulse central wavelength. By increasing the plasma density to $N_e \sim 0.1 N_{cr}$, the required drive pulse energy is reduced to the ~mJ level, provided that the spot size is comparable to the plasma wavelength, and the pulse duration decreases to $< 5fs$; which is ≃ 2 cycles for $\lambda = 800nm$ laser pulses.

The group velocity of a near-monochromatic laser pulse in a uniform subcritical plasma is $v_g \simeq c\left(1 - \frac{\omega_p^2}{2\omega^2}\right) = c(1 - \frac{N_e}{2N_{cr}})$ where ω is the central frequency. The variation of v_g across the very large bandwidth, $\Delta\omega$, of a few-cycle pulse is $\Delta v_g \simeq c\frac{\omega_p^2}{\omega^2}(\frac{\Delta\omega}{\omega}) = -c\frac{N_e}{N_{cr}}(\frac{\Delta\lambda}{\lambda})$. Typical wakefield acceleration experiments are carried out at $\frac{N_e}{N_{cr}} \ll 1$ and $\frac{\Delta\lambda}{\lambda} \ll 1$, making dispersion negligible ($\left|\Delta v_g / v_g\right| \ll 1$). In our experiments carried out at near-critical plasma densities and with very large

bandwidth laser pulses ($\frac{\Delta\lambda}{\lambda}$~0.25), the dispersion $\left|\Delta v_g/v_g\right|$ is non-negligible, and its contribution on the refractive index $n = \left(1 - \frac{1}{2}\frac{\omega_{p0}^2}{\omega^2}\left(1 - \frac{\mathbf{a}^2}{2} + \frac{\Delta N_p}{N_0} + \frac{\delta N}{N_0} - 2\frac{\delta\omega}{\omega}\right)\right)$ cannot be ignored compared to other effects (Sec. 1.4.4). The nonlinear propagation in plasma can cause bandwidth broadening, and the anomalous dispersion of the plasma can help to compress the laser pulse [82,204], allowing a pulse with an appropriately chosen initial chirp to reach its highest intensity deep inside the plasma [203].

In addition to the dispersion, given the few-cycle duration of the pulse, the carrier envelope phase (CEP) is more important to the dynamics (especially in experiments with ionization injection) than when longer pulses are employed [192,205,206]. The preceding discussion makes it clear that the complicated 3D nonlinear dynamics of laser propagation and plasma interaction demands extensive 3D PIC simulations for adequate modeling of electron acceleration in the bubble regime.

5.2 Experimental Setup

The setup for the experiments described in this chapter is very similar to that of Chapter 4. The main difference is the driver pulse and its focusing geometry. Here, we used ~7fs FWHM few-cycle pulse with ~2.5mJ energy generated using the HCF compressor setup described in Chapter 2. The driver beam spectrum peaks at ~680nm, with ~160nm FWHM bandwidth, and an $1/e^2$ intensity beam diameter of $2w_0$~8mm measured before the focusing off-axis parabolic mirror (OAP) used to

focus the beam. Similar to Chapter 4, the open time of the solenoid valve used in the gas jet setup is limited to avoid the accumulation of gamma radiation dose from the accelerated electron bunches colliding with the beam dump. The valve is open for 10ms in all of the data points presented in this chapter; each measured electron spectrum or beam profile is the sum from 10 successive shots. These are divided by 10 for presentation of per-shot results.

All turning mirrors in the beam downstream of the HCF exit point require high reflectivity and low GDD across the whole pulse bandwidth. To avoid the accumulation of a nonlinear phase shift (and beam distortion) in the air after exiting the HCF, the beam is sent to the experimental vacuum chamber through a helium-filled beam transport box that connects the HCF exit chamber and the experimental chamber. The nonlinear refractive index of helium is approximately 20× less than that of air [90]. Helium is very slowly flowed through the beam transport box to keep its pressure marginally over 1 atm, keeping air out. The chirped mirror compressor, fused silica wedges used for fine tuning the pulse duration, and a delay arm for a probe beam are located inside this box. The optical windows between the HCF exit chamber and the helium box, and between the helium box and the experimental vacuum chamber are very thin to avoid dispersion and self-focusing. For this purpose, we used custom broadband anti-reflection coated 1mm thick fused silica windows. The windows were sufficiently thick to avoid significant bowing on the vacuum chamber.

5.2.1 Focusing geometry

The beam is focused on the high density gas jet target using two different geometries. In the first set of experiments, we use an OAP with a focal length of ~25.4mm, corresponding to *f*/3.2 focusing. Assuming a diffraction limited focused spot, the FWHM spot size, in this case, is $\sim 1.6\mu m$, corresponding to a peak vacuum intensity of $\sim 1.2 \times 10^{19} W/cm^2$ and $a_0 \simeq 2$. In the second focusing geometry, the focal length of the OAP is ~50.8mm corresponding to f/6.4 focusing, leading to a FWHM spot size of $\sim 3.2\mu m$, peak vacuum intensity of $\sim 3 \times 10^{18} W/cm^2$, and $a_0 \simeq 1$.

Figure 5.2 shows the nozzle, cooling block, and the OAP, along with a transverse shadowgram as the laser pulse is focused on the hydrogen jet, at a distance $\sim 100\mu m$ above the nozzle orifice. As discussed in Chapter 3, cryo-cooling the valve reservoir gas with liquid nitrogen increases the jet density, enabling interactions at near-critical plasma densities. For argon and nitrogen, used in some of the experiments in this chapter, excessive cooling of those gases in the high pressure valve reservoir (approaching $-160^{\circ} C$ at ~1000Psi) causes a phase change to liquid. To avoid liquefying the gas, the valve is not cooled for experiments with argon and nitrogen jets. Even so, the plasma density for these gases is still near-critical owing to the multiple ionization of Ar and N_2 at our peak vacuum intensities of $> 10^{18} W/cm^2$.

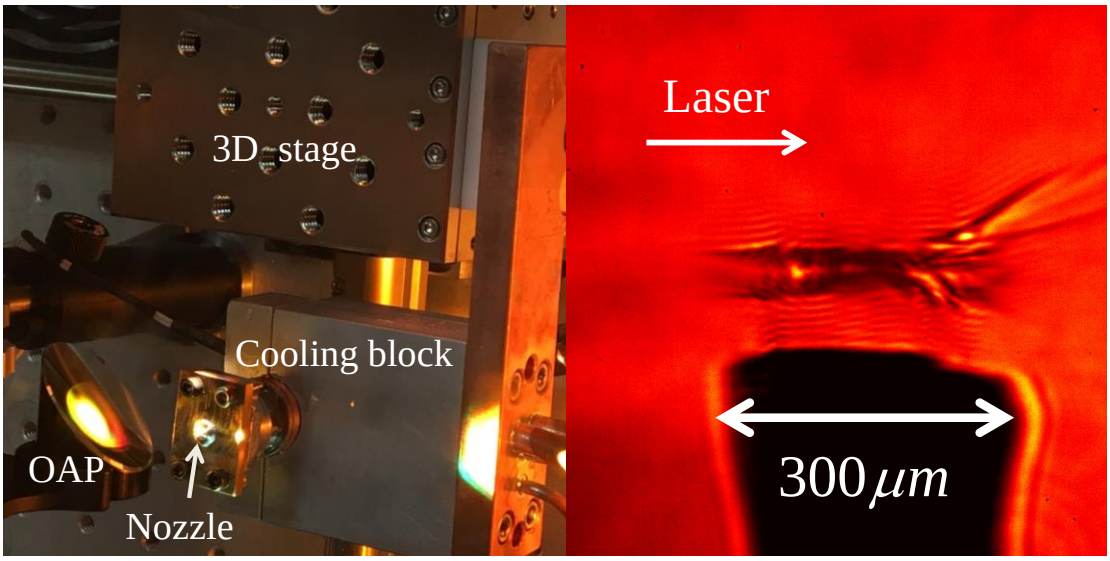

Figure 5.2. (Left panel) The nozzle, cooling block, and OAP as the few-cycle beam is focused on the jet. (Right panel) Transverse shadowgram showing laser interaction with the hydrogen jet.

5.3 Experimental results

5.3.1 Short focal length

Using *f*/3.2 focusing (intensity FWHM $\sim 1.6 \mu m$, peak intensity $\sim 1.2 \times 10^{19} W/cm^2$), we observe accelerated electron bunches from argon, nitrogen and hydrogen jets under various conditions. The Rayleigh length of the laser beam is $\sim 10 \mu m$ in this configuration, whereas the FWHM of the plasma density profile is $150 - 250 \mu m$ for all experiments. Focusing the beam at the entrance side of a hydrogen jet leads to quasi-monoenergetic electron beams peaked at ~1.5MeV, the highest electron energy we could regularly obtain at *f*/3.2. In a small number of shots, we observe accelerated bunches at >2 MeV. However, the electron beam pointing fluctuates shot-to-shot up to ~100mrad (comparable to the beam diameter) in this configuration. Focusing the laser at the far side of the jet and further from the nozzle

orifice (where the density is lower) leads to lower energy beams (~0.5MeV) with better pointing stability from all three gases. The beam divergence is ≥50mrad for all gasses when the laser is focused at the far side of the nozzle. Figure 5.3 compares shadowgrams of the interaction regions, and the corresponding electron beam profile from two successive shots, for the cases where the laser beam is focused (*f*/3.2) at entrance side and exit side of a hydrogen jet. The peak values of N_e/N_{cr}, where the critical density N_{cr} is evaluated at $\lambda = 680nm$, (the spectral peak of the 7fs few-cycle pulse) are given for each case. The counts of the electron beam profile for focus at exit side are multiplied ×1.5 before normalization.

Given that the laser confocal parameter is much smaller than the jet width, it is not surprising that moving the focus with respect to the jet has a significant effect on the accelerated electron bunch energy and pointing stability, although understanding the effects in detail require extensive 3D PIC simulations.

The spectrum of the electron beam from nitrogen jet shows a distinct weak peak at ~1MeV, in addition to a strong peak at ~0.5MeV that exists for all targets with laser focused at the exit side of the jet. The weak higher energy peak in the nitrogen spectrum suggests two different populations of electrons with different injection mechanisms.

In both configurations in Fig. 5.3, for front and back focusing, electrons are accelerated near the beam waist, which in each case is located at a lower density than the jet peak density. For front focusing, as seen in the left panel, the relativistic self-focusing pulse collapse is followed to the right by further complex propagation of the leftover laser pulse energy in higher density plasma. This can lead to the possible

formation of additional wakefields, reducing the overall quality of the beam profile, and introducing the large shot-to-shot pointing fluctuations observed in this case.

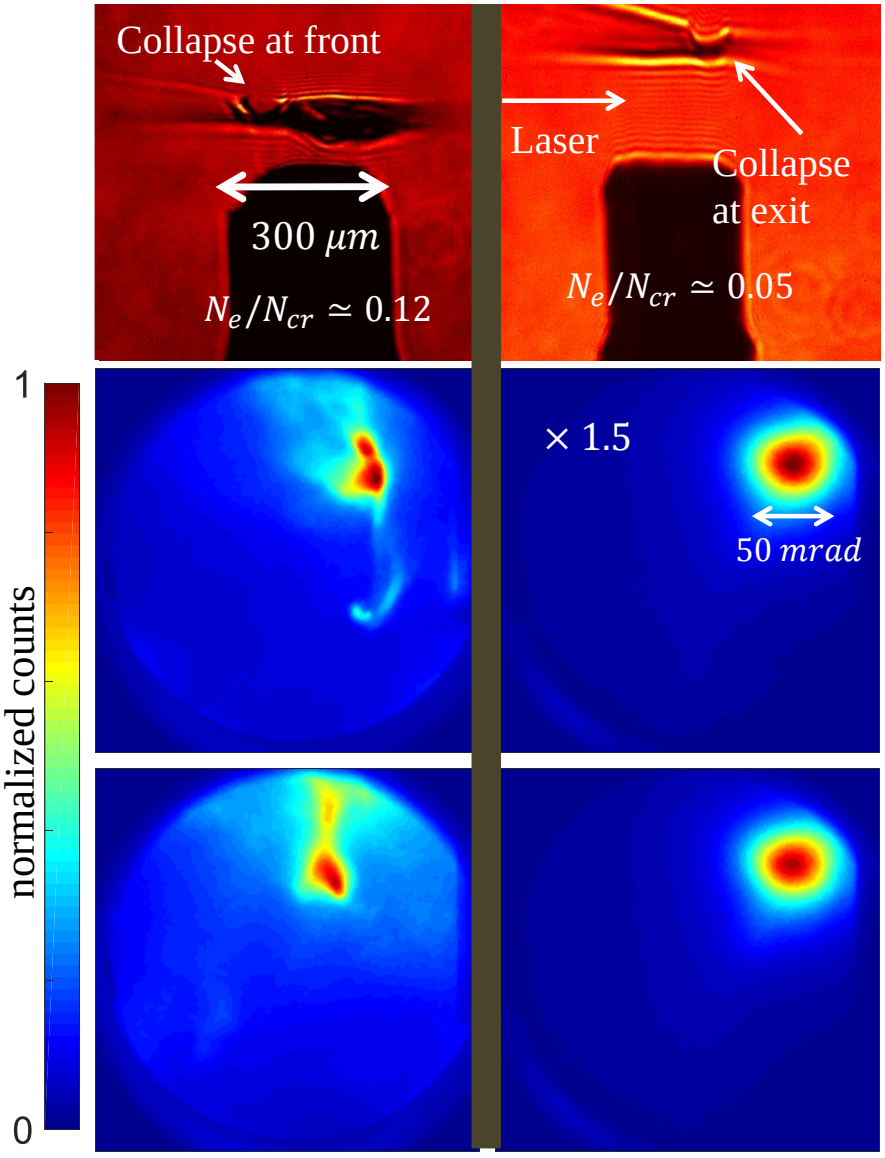

Figure 5.3. Shadowgrams and the corresponding electron beam profiles from two successive shots when the laser pulse focused at entrance side (left), and exit side (right) of a hydrogen gas jet at *f*/3.2 with an OAP. The values of N_e/N_c are shown for each interaction. Focusing at the entrance side leads to higher energy beams with less shot-to-shot stability.

For focusing at the exit side of the jet the leftover laser energy diffracts quickly in the low density plasma, it is unlikely to form additional wakefields, and the

shot to shot stability of the beam pointing gets enhanced compared to the focus at entrance case. The lower energy of the electron beam, in this case, is probably due to the decreasing phase velocity of the wake in the density downramp [207] in addition to lower wakefield amplitude at the lower density plasma.

5.3.2 Long focal length

The Rayleigh length for the longer focal length OAP (*f*/6.4 focusing) is $\sim 35\mu m$. Unlike the *f*/3.2 case, where we had two distinct focus positions across the jet leading to electron acceleration, in *f*/6.4 case, we only have a single focus position with ≥ MeV electron beams. In this configuration, with the beam focused near the center of the jet, the electron beams from hydrogen jets have higher peak energy, lower beam divergence, and better shot-to-shot pointing stability compared to any condition in the case of *f*/3.2 focusing. We didn't detect any electron beams from argon, nitrogen, and helium jets in this configuration. Figure 5.4 compares the electron beam spectra and beam profile for four different peak electron densities in the H_2 jet. The beam charges and divergences are shown in the figure. To compare electron beam profiles, the counts in each case are multiplied by factors shown in the figure before normalization. Quasi-monoenergetic bunches are observed and the beam divergence angle is smaller than 50mrad in all cases. For $\frac{N_e}{N_{cr}} \simeq 0.07$, the quasi-monoenergetic spectrum peaks at $\lesssim$ 1MeV energy, where the LANEX screen has the highest efficiency; the signal from the LANEX screen saturates the CCD camera in this case. Increasing the plasma density to $\frac{N_e}{N_{cr}} \simeq 0.12$ increases the bunch energy, lowers the total accelerated charge and reduces the beam divergence. Increasing the

plasma density beyond this point lowers the beam energy and increases the divergence again. As can be seen from the figure, the lowest beam divergence doesn't necessarily correspond to highest bunch energy.

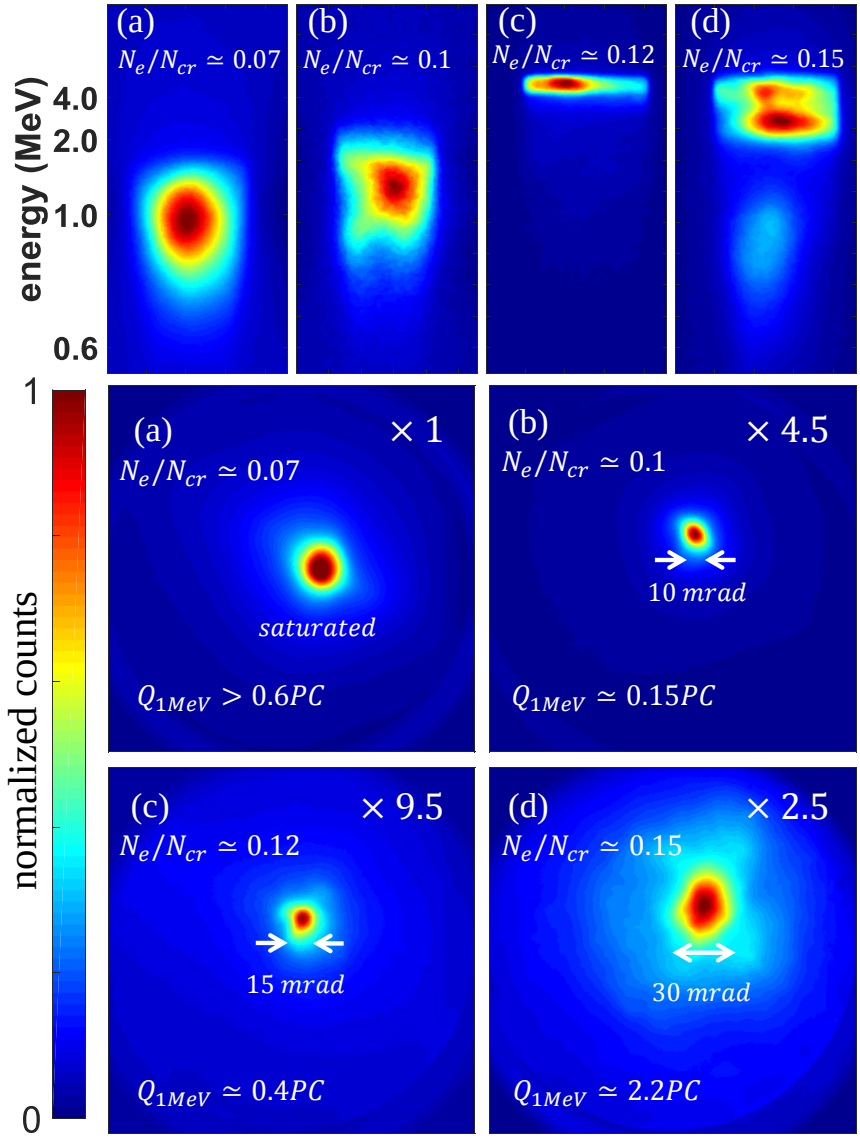

Figure 5.4. Energy spectra (top) and corresponding electron beam profiles (bottom) for hydrogen jet with four different peak electron densities. The beam divergence angle, the total charge with > 1MeV energy, and the beam image scaling factor are shown in each panel.

Figure 5.5 shows the quasi-monoenergetic energy spectrum (linear energy axis) in Fig. 5.4(c)(top) for $\frac{N_e}{N_{cr}} \simeq 0.12$, where the measured resolution of the E=4.8 MeV peak is $\frac{\Delta E}{E} \simeq 0.4$. The width of the 4.8 MeV peak, $\Delta E \gtrsim 2\ MeV$, is comparable to the projected width of the magnetic spectrometer's entrance slit on the LANEX detector for the case of no spectrometer magnetic field. As the measured electron spectrum is the convolution of the spectrometer response with the actual spectrum, we conclude that our measured $\frac{\Delta E}{E}$ is slit width-limited and that the actual energy resolution is better. This will be verified in upcoming experiments using a narrower slit in our magnetic spectrometer.

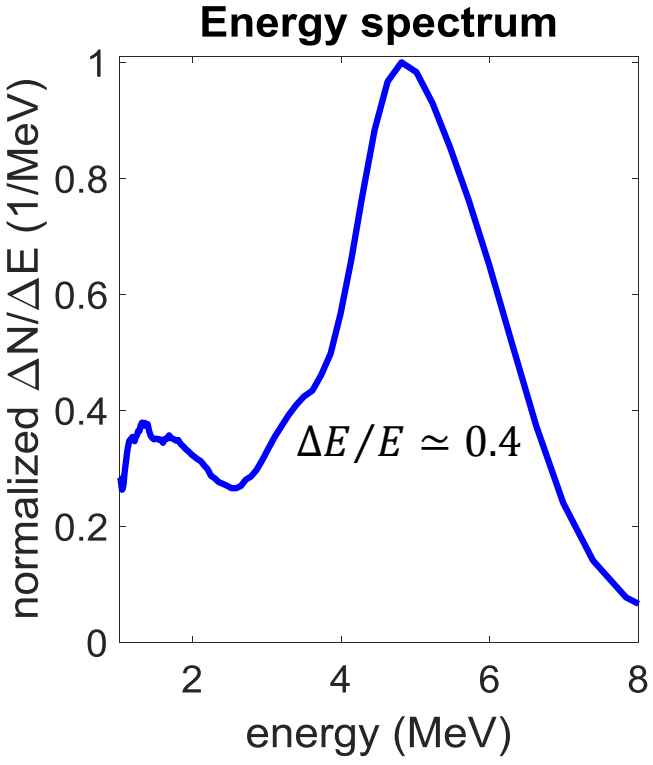

Figure 5.5. Quasi-monoenergetic electron energy spectrum for plasma density $\frac{N_e}{N_{cr}} \simeq 0.12$. We conclude that our measured value of $\frac{\Delta E}{E}$ is spectrometer entrance slit width-limited.

5.3.3 Beam stability

With *f*/3.2 focusing the beam pointing was more stable when the laser pulse was focused at the far side of the jet. Even in this case, the total accelerated charge fluctuated shot-to-shot. Switching to *f*/6.4 focusing leads to higher energy electron beams with better shot-to-shot stability in terms of bunch energy, pointing, and charge. Figure 5.6 compares the energy stability for *f*/3.2 focusing at the entrance of hydrogen jet at plasma density of $\frac{N_e}{N_{cr}} \simeq 0.12$, with *f*/6.4 focusing on hydrogen jet at plasma density of $\frac{N_e}{N_{cr}} \simeq 0.2$. In the latter case, we use a nozzle with 150μm diameter nozzle and the laser is focused in a region with longer FWHM comparing to the beams in Fig 5.4. The beam pointing in *f*/3.2 case fluctuates and it misses the slit in some shots. The figure also indicates poor shot to shot spectrum stability for the *f*/3.2 case as the spectrum of the shots passing through the slit also fluctuates

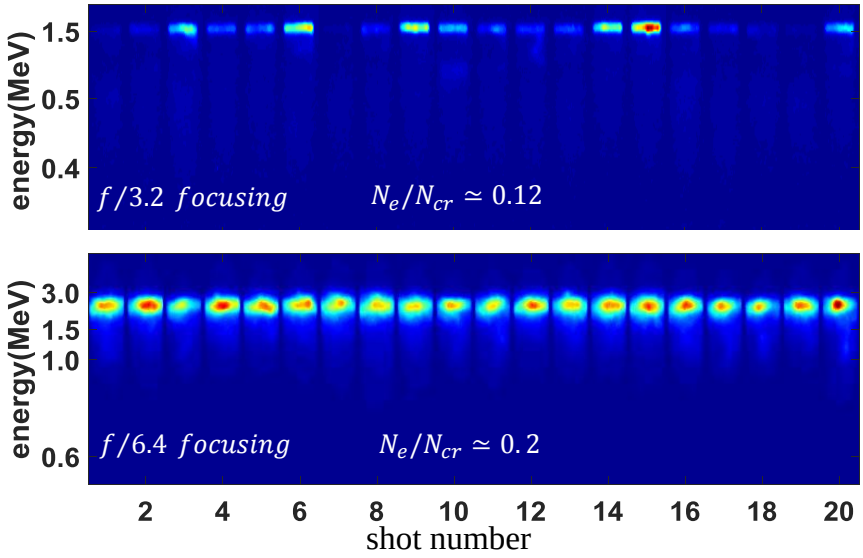

Figure 5.6. Electron beam energy and pointing stability comparison for *f*/3.2 (top) and *f*/6.4 (bottom) focusing on hydrogen jets. Each panel shows 20 successive collected beam images. Each beam image is the average from 10 successive shots, for a total of 200 shots.

5.4 Discussion

The highest energy observed in these experiments was $\lesssim$ 5 MeV for $\frac{N_e}{N_{cr}} \simeq 0.12$, for which $\lambda_p \sim 2\mu m$. This is close to the length $c\tau \simeq 2.1\mu m$ of the $\tau = 7fs$ FWHM pulse used in these experiments. Both $c\tau$ and λ_p are slightly smaller than the beam spot size ($w_0 \simeq 2.7\mu m$) for *f*/6.4 focusing. Although a lower density and bigger λ_p is a better match for satisfying $c\tau \simeq \lambda_p/2$, our pulse energy is not high enough to drive a high amplitude plasma wake at lower densities. In order to keep the a_0 value constant, the pulse energy should increase significantly for longer plasma wavelengths $E_L \propto \lambda_P^3$.

From Eqs. 5.3 and 5.4 the depletion length for the laser pulse at $\frac{N_e}{N_{cr}} \simeq 0.12$ is $L_{depl} \simeq 17\mu m$ and the dephasing length calculated for a cavity size equal to the focused spot size is $L_d \simeq 15\mu m$ for *f*/6.4 focusing. The dephasing length and the depletion length are almost equal for *f*/6.4 focusing and this leads to more efficient acceleration. Highest quality beams in this case occur for $\lambda_p \sim c\tau$.

Comparing the two different focusing configurations, in the case of *f*/3.2 focusing the beam spot radius $w_0 \simeq 1.4\mu m$ is considerably smaller than the laser pulse length ($w_0 < c\tau_L$). This requires the bubble radius to be smaller than the pulse length, so, Eq. 5.1 cannot be satisfied for any plasma density and stable self-guided propagation cannot occur for distances longer than Rayleigh length. For *f*/6.4 focusing, the beam waist $w_0 \simeq 2.7\mu m$ satisfies $w_0 > c\tau_L$ and Eq. 5.1 is satisfied at a specific plasma density found along the laser beam path. It is possible that this applies

to our highest energy result, where acceleration occurs at a lower plasma density in the profile than the peak.

Our laser pulse intensity is lower than typical intensities of experiments in the bubble regime (with $a_0 > 2$), and for most conditions with detected electron beams we have $k_p w_0 > 2\sqrt{a_0}$, i.e. our conditions do not satisfy Eq. 5.2. So we expect that use of higher energy few-cycle pulses [208], with similar focusing geometry and target density, should lead to better matching of the condition for self-guided beam propagation in plasma and acceleration of electron bunches to higher energies [209].

Other than the dephasing and depletion lengths, the other important length scale in LWFA experiments is the FWHM of the plasma density along the beam propagation direction, which is $\sim 150 - 250\mu m$ for all the experiments in this chapter. This length scale is longer than depletion length, dephasing length, and the Rayleigh length for all of the experiments. Use of thinner jets with FWHM comparable to the Rayleigh length and sharper density gradients can help to achieve more efficient acceleration [210], and lead to lower energy spread beams by lowering the chance of multiple electron injections in the long acceleration span [211].

For the higher intensity laser pulses achieved in *f*/3.2 focusing, electron acceleration from jets of various gases was observed, whereas for the lower intensity case (*f*/6.4) we only observed accelerated electrons from hydrogen jets. This is understood in the same way as for the SM-LWFA results of Chapter 4: low energy pulses lead to accelerated electron bunches only in hydrogen due to much less ionization-induced defocusing [20].

In the hydrogen plasma bubble regime accelerator, injection likely occurs as a result of the wavebreaking and the transverse oscillations of the cavity due to varying CEP of the few-cycle pulse as it propagates in the plasma [212,213]. In the case of nitrogen (*f*/3.2 focusing), we commonly see two distinct peaks in the energy spectra. The main peak is similar to what we measure for hydrogen targets, with injection mainly by wavebreaking. However, the weaker peak with higher energy can be attributed to ionization injection [203,214], which cannot occur in hydrogen plasma. The amplitude of the electric field changes by less than 1% due to the variations in the CEP in our case ($\tau = 7fs$, $\lambda = 680\,nm$ pulses) and the ionization injection does not occur for hydrogen jets, so we don't expect an observable effect from unstable CEP in our experiments with *f*/6.4 focusing. Extensive 3D PIC simulations are required for better understanding of the laser pulse dynamics, and the electron bunch injection and acceleration.

5.5 Summary and conclusion

In summary, the use of few-cycle laser pulses and operating in the bubble regime leads to significantly higher electron beam quality compared to the SM-LWFA regime experiments described in Chapter 4. Using 7fs FWHM, 2.5mJ laser pulses, we demonstrated the generation of ~5MeV quasi-monoenergetic electron bunches. This is in strong contrast to the exponential electron energy distributions generated by SM-LWFA. As well, the beam divergence is about 10 times smaller in the bubble regime compared to the SM-LWFA. The total accelerated charge per shot with >1MeV is ~ 1pC for both the bubble and SM-LWFA regimes, while the driving

pulse energy is ~4× lower in the bubble regime. Our results indicate better electron beam quality and higher peak energy for a longer focal length OAP. For that case, the laser beam parameters are better matched to the bubble regime condition in Eq. 5.1.

These results bring us closer to a high repetition rate table top ~MeV accelerator with high quality electron bunches. Such a high-repetition-rate, high-flux ultrafast source has applications in time-resolved probing of matter for scientific, medical, or security applications, either using the electrons directly or using a high-Z foil converter to generate ultrafast γ rays.

Chapter 6: Summary and directions for future research

6.1 Summary

Laser-driven electron acceleration is a promising path for making future generations of electron accelerators. However, more research is required to improve the electron beam parameters such as energy spread, emittance, repetition rate, shot to shot stability, and average current to match those needed for the intended applications. The experiments in this dissertation were designed to lower the threshold laser energy required for electron acceleration and generate high quality electron bunches (in terms of the emittance and energy spread) at a kHz repetition rate. Use of a near critical density jet target lowers the critical power for relativistic self-focusing and enables wakefield acceleration with lower pulse energies delivered from higher repetition rate lasers. In Chapter 3 of the dissertation, we described the generation of a thin and high density gas jet target for laser plasma interaction experiments. Cryogenic cooling of hydrogen or helium gas before its injection into a vacuum chamber through a ~$100\mu m$ scale nozzle allows it to reach overcritical densities (for ~800nm pulses) at the nozzle exit. A laser pulse focused at the near critical density region of the jet ($N_e/N_{cr} \geq 0.1$), only requires sub-terawatt peak power for relativistic self-focusing and subsequent electron acceleration in the SM-LWFA regime. Chapter 4 presented the results of electron acceleration from high density hydrogen and helium plasmas driven by 30fs laser pulses with $\leq$ 10mJ energy. In these experiments, which were carried out at a kHz repetition rate, we

observed electron bunches with ~1pC charge per shot at >MeV energies [20]. In the case of hydrogen jets, electron acceleration was observed using laser pulses with only ~1mJ energy, clearing the way for even higher repetition rates.

The electron bunches accelerated in Chapter 4 have a thermal energy distribution and a rather large divergence angle. It is well known that electron beams generated in the bubble regime have smaller energy spreads and divergences compared to those in the SM-LWFA regime. High intensity drive laser pulses, with a pulse length shorter than the plasma wavelength, focused to a spot size comparable to the plasma wavelength can eject all of the plasma electrons out of the focal region and form an ion cavity. As the cavity (bubble) propagates through the plasma, following the laser pulse, some of the background electrons are trapped at the back side of the cavity and get accelerated [52,57]. For a high density plasma ($N_e/N_{cr} \geq 0.1$) the laser pulse duration should be only a few femtoseconds in order to operate at the bubble regime. Chapter 2 discussed the details of bandwidth broadening and few-cycle pulse generation through the use of a hollow core fiber (HCF). The few-cycle pulses (~7fs duration, ~2.5mJ energy) generated through the HCF were focused on near critical density jet targets in Chapter 5 for electron acceleration at the bubble regime. The results showed significant improvement in the energy spread and divergence angle compared to the SM-LWFA case. Electron bunches at ~5MeV and with ~1pC charge per shot accelerated in bubble regime produce a distinct peak with $\Delta E/E \simeq 0.4$ and a divergence angle of ~15 mrad, more than 10 times smaller than the divergence in SM-LWFA experiments.

6.2 Directions for future research

6.2.1 Further optimizations and use of the laser-driven electron beams for ultrafast studies

The electron bunches generated in Chapter 5 were a big step forward, but there is still room to improve the electron beam energy spread, divergence, and peak energy by optimizing the experiment setup. The bandwidth of the laser pulse from the hollow core fiber used in the experiments corresponds to ~4fs transform limited pulses. Lowering the amount of glass in the beam path and in turn number of reflections from the chirped mirrors, reduces the higher order phase from these components and makes the pulse duration shorter. This enables us to operate at the bubble regime with higher plasma densities. Using a gas jet with a sharp density gradient (Sec. 3.6) and a density FWHM comparable to the Rayleigh length, dephasing length, and the depletion length should improve the beam charge [210], energy spread, and the divergence angle [211].

One of the advantages of operating at a high repetition rate is the possibility of quick scanning and optimization due to improved data statistics. Fine adjustments of the driver pulse spatiotemporal profile through the use of feedback loops, including control of the spectral phase [215,216] and the wavefront of the beam [217,218], can further improve and stabilize electron beam parameters such as energy spread, emittance, and peak energy. Laser-driven electron bunches are of great interest for ultrafast studies due to their short duration and being inherently synchronized to a laser pulse. Using laser-driven accelerated electron with sub-MeV energy for ultrafast

electron diffraction has already been demonstrated [17]; multi-MeV electron bunches from our experiment stretch less due to the space charge effect and can be used for better temporal resolution as well as for interrogating denser material in ultrafast studies.

6.2.2 Few-cycle beam interaction with clusters

In Chapter 3 we discussed the characterization of the size and the density of the clusters that are formed due to the rapid expansion of gas out of a high pressure nozzle as the flow moves away from the nozzle tip. In high power laser interactions with clusters, the ionization process starts with the generation of initial free electrons through optical field ionization. The subsequent collisional ionization in the cluster bulk, which has a near solid density $N_{bulk} \geq 10^{22} cm^{-3}$, enhances the absorption of the laser energy. The heated cluster eventually explodes on a sub-picosecond time scale [159,219]. The efficient absorption of the laser energy makes the clusters an interesting target for various laser plasma interaction experiments including x-ray generation [160,220,221], ion [161,222,223] and electron acceleration [163,224], and fusion [134,225].

The induced dipole moment of the cluster is given by $\boldsymbol{P} = \Gamma \boldsymbol{E}$ where $\Gamma = a^3(\frac{\varepsilon-1}{\varepsilon+2})$ is the cluster polarizability, a is the cluster radius, and ε is the dielectric constant of the bulk plasma internal to the cluster [219]. The real value of the cluster's polarizability, Γ_r , evolves with time as the cluster becomes ionized and expands. Initially, the optical response from the overcritical density portion of the cluster is dominant, $\Gamma_r > 0$ and increases with time. Further expansion of the cluster causes Γ_r

to decrease, cross zero, and approach asymptotic negative values as the subcritical density portion becomes dominant [226]. Considering the radial and temporal variations of the polarizability, the average polarizability of the cluster ensemble, $\overline{\Gamma_r}$, rises faster near the beam axis, where the intensity is higher than at the edge of the beam. So at early times after ionization, $\overline{\Gamma_r}$ and, in turn, the effective refractive index is peaked on axis, leading to self-focusing of laser pulses shorter than the cluster expansion time scale (order $\sim 100 fs$ depending on field intensity and the cluster size). The beam lensing becomes negligible for longer pulses because the plasma becomes more uniform on longer timescales and a larger portion of the pulse resides outside the region where $\overline{\Gamma_r}$ decreases with radius [227]. Previous experiments have demonstrated pulse length dependent self-focusing in a cluster gas using moderate intensities of 3.5×10^{16} W/cm^2 [227]. At higher intensities ($\sim10^{17}$ W/cm^2) using 70fs, 50mJ laser pulses, has led to the generation of x-rays with $\sim 850 keV$ energy, which is associated with self-focusing in the cluster gas [228].

In our experiments focusing few-cycle pulses in clustered gases, we observe a strong self-focusing with almost no trace of the laser beam forming plasmas in a gap with $> 150 \mu m$ length near the focus position as the pulse passes from the focus. Glowing from plasma regions surrounded by sharp boundaries can be seen upstream and downstream of this gap. For these experiments, we use the same setup as f/6.4 focusing in Chapter 5, except here we focus the beam higher above the nozzle. Figure 6.1 shows shadowgrams taken at ~0.7 ns probe delay, where the laser is focused 1.25mm above a $150 \mu m$ diameter nozzle injecting hydrogen gas, at $-160°C$ temparature and with 1000psi, 500psi, and 250psi backing pressures, into the vacuum

chamber. The cluster radius is ~2nm with a backing pressure of 1000 psi pressure, ≤1nm at 500 psi and drops below the detection limit (~0.5nm) at 250 psi (Sec. 3.5.2). Our experiments confirm that the gap is formed due to clusters because the two sections connect if we make the cluster size smaller by lowering the backing pressure, increasing the gas temperature, or focusing the laser closer to the nozzle. The gap also disappears when using helium jet targets where no clusters are formed at accessible temperatures and pressures. No electron beams were detected under the conditions where we observe the gap.

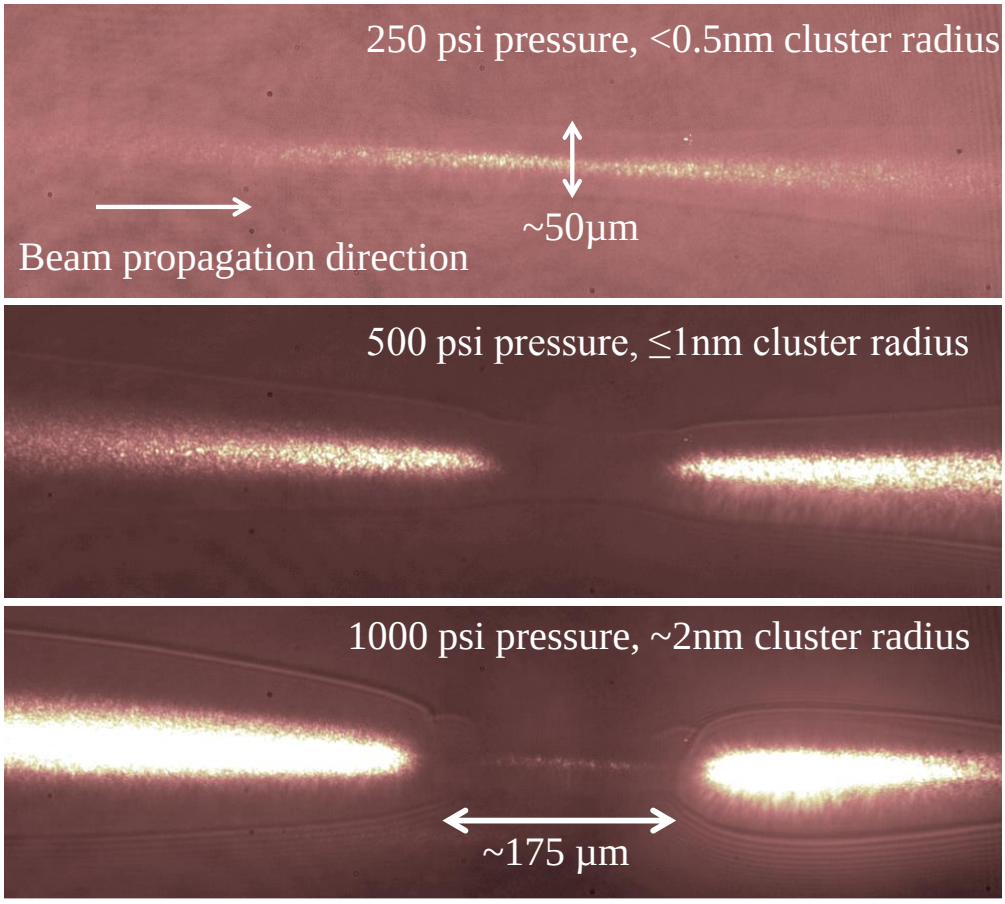

Figure 6.1. Self-focusing of few-cycle laser pulses in clustered hydrogen gas with 250psi (top), 500psi (middle), and 1000psi (bottom) backing pressure. Glowing from plasma regions and sharp boundaries in the probe beam are visible upstream and downstream of the focus, but there is a gap with no significant plasma formation in the middle.

In addition to the strong self-focusing, the forward spectrum of the beam collected downstream of the gas jet shows a blue shifted peak with a central wavelength near 600 nm and a >25nm bandwidth from the few-cycle pulse interaction with the plasma. We observe this blue shifted peak when the beam is focused in plasmas with densities ranging from $N_e<0.01N_{cr}$ to $N_e> 0.1\ N_{cr}$ produced by ionization of different gas species including hydrogen, helium, nitrogen, and argon. The relative strength of the blue shifted peak changes depending on the peak plasma density and the focusing position on the gas jet. Increasing the pump laser pulse duration shifts the center wavelength of the peak to larger values, and eventually causes the peak to disappear. Constant blue shifting, independent of density, has been observed in previous experiments and has been attributed to filamentation of the pulse in the background gas [229,230]. Also, simulations of the few-cycle pulse interaction with clusters suggest pulse energy conversion to radiation at Mie frequency as the expanding cluster density passes through the resonance point [231]. Both of these suggestions may contribute partially to the blue-shifted peak that we detect, but further experiments and modeling are required for a complete understanding of our results observed in few-cycle pulse interaction with plasma.

Bibliography

1. R. W. Hamm and M. E. Hamm, "The beam business: Accelerators in industry," Phys. Today **64**, 46 (2011).

2. M. Reiser, "*Theory and Design of Charged Particle Beams*" (Wiley, 2008).

3. T. P. Wangler and T. P. Wangler, "*RF Linear Accelerators*" (Wiley-VCH, 2008).

4. A. Grudiev, S. Calatroni, and W. Wuensch, "New local field quantity describing the high gradient limit of accelerating structures," Phys. Rev. Spec. Top. -Accel. Beams **12**, 102001 (2009).

5. D. Dannheim, P. Lebrun, L. Linssen, D. Schulte, F. Simon, S. Stapnes, N. Toge, H. Weerts, and J. Wells, "CLIC e+e− Linear Collider Studies," arXiv:1208.1402v1 (2012).

6. T. Tajima and J. M. Dawson, "Laser Electron Accelerator," Phys. Rev. Lett. **43**, 267 (1979).

7. V. Malka, S. Fritzler, E. Lefebvre, M.-M. Aleonard, F. Burgy, J.-P. Chambaret, J.-F. Chemin, K. Krushelnick, G. Malka, S. P. D. Mangles, Z. Najmudin, M. Pittman, J.-P. Rousseau, J.-N. Scheurer, B. Walton, and A. E. Dangor, "Electron Acceleration by a Wake Field Forced by an Intense Ultrashort Laser Pulse," Science **298**, 1592 (2002).

8. W. Leemans and E. Esarey, "Laser-driven plasma-wave electron accelerators," Phys. Today **62**, 44 (2009).

9. S. P. D. Mangles, C. D. Murphy, Z. Najmudin, A. G. R. Thomas, J. L. Collier, A. E. Dangor, E. J. Divall, P. S. Foster, J. G. Gallacher, C. J. Hooker, D. A. Jaroszynski, A. J. Langley, W. B. Mori, P. A. Norreys, F. S. Tsung, R. Viskup, B. R. Walton', and K. Krushelnick, "Monoenergetic beams of relativistic electrons from intense laser–plasma interactions," Nature **431**, 535 (2004).

10. C. G. R. Geddes, C. Toth, J. van Tilborg, E. Esarey, C. B. Schroeder, D. Bruhwiler, C. Nieter, J. Cary, and W. P. Leemans, "High-quality electron beams from a laser wakefield accelerator using plasma-channel guiding," Nature **431**, 538 (2004).

11. J. Faure, Y. Glinec, A. Pukhov, S. Klselev, S. Gordienko, E. Lefebvre, J. P. Rousseau, F. Burgy, and V. Malka, "A laser-plasma accelerator producing monoenergetic electron beams," Nature **431**, 541 (2004).

12. W. P. Leemans, A. J. Gonsalves, H. S. Mao, K. Nakamura, C. Benedetti, C. B.

Schroeder, C. Tóth, J. Daniels, D. E. Mittelberger, S. S. Bulanov, J. L. Vay, C. G. R. Geddes, and E. Esarey, "Multi-Gev electron beams from capillary-discharge-guided subpetawatt laser pulses in the self-trapping regime," Phys. Rev. Lett. **113**, 245002 (2014).

13. A. J. Gonsalves, K. Nakamura, J. Daniels, C. Benedetti, C. Pieronek, T. C. H. De Raadt, S. Steinke, J. H. Bin, S. S. Bulanov, J. Van Tilborg, C. G. R. Geddes, C. B. Schroeder, C. Tóth, E. Esarey, K. Swanson, L. Fan-Chiang, G. Bagdasarov, N. Bobrova, V. Gasilov, G. Korn, P. Sasorov, and W. P. Leemans, "Petawatt Laser Guiding and Electron Beam Acceleration to 8 GeV in a Laser-Heated Capillary Discharge Waveguide," Phys. Rev. Lett. **122**, 084801 (2019).

14. S. Cipiccia, M. R. Islam, B. Ersfeld, R. P. Shanks, E. Brunetti, G. Vieux, X. Yang, R. C. Issac, S. M. Wiggins, G. H. Welsh, M.-P. P. Anania, D. Maneuski, R. Montgomery, G. Smith, M. Hoek, D. J. Hamilton, N. R. C. C. Lemos, D. Symes, P. P. Rajeev, V. O. Shea, J. M. Dias, and D. A. Jaroszynski, "Gamma-rays from harmonically resonant betatron oscillations in a plasma wake," Nat. Phys. **7**, 867 (2011).

15. A. Döpp, E. Guillaume, C. Thaury, A. Lifschitz, F. Sylla, J. P. Goddet, A. Tafzi, G. Iaquanello, T. Lefrou, P. Rousseau, E. Conejero, C. Ruiz, K. Ta Phuoc, and V. Malka, "A bremsstrahlung gamma-ray source based on stable ionization injection of electrons into a laser wakefield accelerator," Nucl. Instruments Methods Phys. Res. Sect. A **830**, 515 (2016).

16. G. C. Bussolino, A. Faenov, A. Giulietti, D. Giulietti, P. Koester, L. Labate, T. Levato, T. Pikuz, and L. A. Gizzi, "Electron radiography using a table-top laser-cluster plasma accelerator," J. Phys. D. Appl. Phys. **46**, 245501 (2013).

17. Z. H. He, B. Beaurepaire, J. A. Nees, G. Gallé, S. A. Scott, J. R. S. Pérez, M. G. Lagally, K. Krushelnick, A. G. R. Thomas, and J. Faure, "Capturing Structural Dynamics in Crystalline Silicon Using Chirped Electrons from a Laser Wakefield Accelerator," Sci. Rep. **6**, 36224 (2016).

18. E. Esarey, C. B. Schroeder, and W. P. Leemans, "Physics of laser-driven plasma-based electron accelerators," Rev. Mod. Phys. **81**, 1229 (2009).

19. E. Esarey, P. Sprangle, J. Krall, and A. Ting, "Overview of Plasma-Based Accelerator Concepts," IEEE Trans. Plasma Sci. **24**, 252 (1996).

20. F. Salehi, A. J. Goers, G. A. Hine, L. Feder, D. Kuk, B. Miao, D. Woodbury, K. Y. Kim, and H. M. Milchberg, "MeV electron acceleration at 1 kHz with <10 mJ laser pulses," Opt. Lett. **42**, 215 (2017).

21. A. J. Goers, G. A. Hine, L. Feder, B. Miao, F. Salehi, J. K. Wahlstrand, and H. M. Milchberg, "Multi-MeV Electron Acceleration by Subterawatt Laser Pulses," Phys. Rev. Lett. **115**, 194802 (2015).

22. R. R. Alfano, "*The Supercontinuum Laser Source*" (Springer, 2006).

23. R. W. Boyd, "*Nonlinear Optics*" (Academic Press, 2008).

24. A. Couairon and A. Mysyrowicz, "Femtosecond filamentation in transparent media," Phys. Rep. **441**, 47 (2007).

25. R. Y. Chiao, E. Garmire, and C. H. Townes, "Self-Trapping of Optical Beams," Phys. Rev. Lett. **13**, 126 (1964).

26. J. H. Marburger, "Self-focusing: Theory," Prog. Quant. Electr., **4**, 35 (1975).

27. L.V. Keldysh, "IONIZATION IN THE FIELD OF A STRONG ELECTROMAGNETIC WAVE," Sov. Phys. JETP **20**, 1307 (1965).

28. R. H. Stolen and W. J. Tomlinson, "Effect of the Raman part of the nonlinear refractive index on propagation of ultrashort optical pulses in fibers," J. Opt. Soc. Am. B **9**, 565 (1992).

29. F. DeMartini, C. H. Townes, T. K. Gustafson, and P. L. Kelley, "Self-steepening of light pulses," Phys. Rev. **164**, 312 (1967).

30. P. B. Corkum and C. Rolland, "Supercontinuum Generation in," Phys. Rev. Lett. **57**, 2268 (1986).

31. J. D. Jackson, "*Classical Electrodynamics* " (Wiley, 1999).

32. X. L. Chen and R. N. Sudan, "Two-dimensional self-focusing of short intense laser pulse in underdense plasma," Phys. Fluids B **5**, 1336 (1993).

33. E. Esarey, P. Sprangle, J. Krall, A. Ting, and G. Joyce, "Optically guided laser wake-field acceleration," Phys. Fluids B **5**, 2690 (1993).

34. P. Gibbon, "*Short Pulse Laser Interactions with Matter : An Introduction*" (Imperial College Press, 2005).

35. E. S. Sarachik and G. T. Schappert, "Classical theory of the scattering of intense laser radiation by free electrons," Phys. Rev. D **1**, 2738 (1970).

36. S. Corde, K. Ta Phuoc, G. Lambert, R. Fitour, V. Malka, A. Rousse, A. Beck, and E. Lefebvre, "Femtosecond x rays from laser-plasma accelerators," Rev. Mod. Phys. **85**, 1 (2013).

37. U. Mohideen, H. W. K. Tom, R. R. Freeman, J. Boker, and P. H. Bucksbaum, "Interaction of free electrons with an intense focused laser pulse in Gaussian and conical axicon geometries," J. Opt. Soc. AM. B **9**, 2190 (1992).

38. J. N. Bardsley, B. M. Penetrante, and M. H. Mittleman, "Relativistic dynamics

of electrons in intense laser fields," Phys. Rev. A **40**, 2823(1989).

39. J. M. Dawson, "Nonlinear electron oscillations in a cold plasma," Phys. Rev. **113**, 383 (1959).

40. P. Sprangle, E. Esarey, and A. Ting, "Nonlinear Theory of Intense Laser-Plasma Interactions," Phys. Rev. Lett. **64**, 2011 (1990).

41. P. Sprangle, E. Esarey, and A. Ting, "Nonlinear interaction of intense laser pulses in plasmas," Phys. Rev. A **41**, 4463 (1990).

42. E. Esarey, S. K. Ride, and P. Sprangle, "Nonlinear Thomson scattering of intense laser pulses from beams and plasmas," Phys. Rev. E **48**, 3003 (1993).

43. C. K. Birdsall and A. B. Langdon, "*Plasma Physics via Computer Simulation*" (Taylor & Francis, 2005).

44. R. A. Fonseca, L. O. Silva, F. S. Tsung, V. K. Decyk, W. Lu, C. Ren, W. B. Mori, S. Deng, S. Lee, T. Katsouleas, and J. C. Adam, "OSIRIS: A Three-Dimensional, Fully Relativistic Particle in Cell Code for Modeling Plasma Based Accelerators," Computational Science, ICCS, 342 (2002).

45. K. S. Yee, "Numerical Solution of Initial Boundary Value Problems Involving Maxwell's Equations in Isotropic Media," IEEE Trans. Antennas Propag. **14**, 302 (1966).

46. D. F. Gordon, "Improved ponderomotive guiding center algorithm," IEEE Trans. Plasma Sci. **35**, 1486(2007).

47. T. D. Arber, K. Bennett, C. S. Brady, A. Lawrence-Douglas, M. G. Ramsay, N. J. Sircombe, P. Gillies, R. G. Evans, H. Schmitz, A. R. Bell, and C. P. Ridgers, "Contemporary particle-in-cell approach to laser-plasma modelling," Plasma Phys. Control. Fusion **57**, 113001 (2015).

48. E. Esarey and M. Pilloff, "Trapping and acceleration in nonlinear plasma waves," Phys. Plasmas **2**, 1432 (1995).

49. P. Sprangle, C. M. Tang, and E. Esarey, "Self-Focusing of Radiation Beams in Plasmas.," IEEE Trans. Plasma Sci. **PS-15**, 145 (1987).

50. W. B. Mori, "The physics of the nonlinear optics of plasmas at relativistic intensities for short-pulse lasers," IEEE J. Quantum Electron. **33**, 1942 (1997).

51. G.-Z. Sun, E. Ott, Y. C. Lee, and P. Guzdar, "Self-focusing of short intense pulses in plasmas," Phys. Fluids **30**, 526 (1987).

52. W. Lu, M. Tzoufras, C. Joshi, F. S. Tsung, W. B. Mori, J. Vieira, R. A. Fonseca, and L. O. Silva, "Generating multi-GeV electron bunches using

single stage laser wakefield acceleration in a 3D nonlinear regime," Phys. Rev. Spec. Top. - Accel. Beams **10**, 061301 (2007).

53. J. Krall, A. Ting, and E. Esarey, "Enhanced acceleration in a self-modulated-laser wake-field accelerator," Phys. Rev. E **48**, 2157 (1993).

54. M. N. Rosenbluth and C. S. Liu, "Excitation of plasma waves by two laser beams," Phys. Rev. Lett. **29**, 701(1972).

55. N. E. Andreev, L. M. Gorbunov, V. I. . Kirsanov, A. A. Pogosova, and R. R. Ramazashvili, "Resonant excitation of wakefields by a laser pulse in a plasma," JETP Lett., **55**, 571 (1992).

56. D. Umstadter, E. Esarey, and J. Kim, " Nonlinear Plasma Waves Resonantly Driven by Optimised Laser Pulse Trains," Phys. Rev. Lett. **72**, 1224 (1994).

57. I. Kostyukov, A. Pukhov, and S. Kiselev, "Phenomenological theory of laser-plasma interaction in “bubble” regime," Phys. Plasmas **11**, 5256 (2004).

58. W. Lu, C. Huang, M. Zhou, M. Tzoufras, F. S. Tsung, W. B. Mori, and T. Katsouleas, "A nonlinear theory for multidimensional relativistic plasma wave wakefields," Phys. Plasmas **13**, 56709 (2006).

59. S. Kneip, C. McGuffey, J. L. Martins, S. F. Martins, C. Bellei, V. Chvykov, F. Dollar, R. Fonseca, C. Huntington, G. Kalintchenko, A. Maksimchuk, S. P. D. Mangles, T. Matsuoka, S. R. Nagel, C. A. J. Palmer, J. Schreiber, K. T. Phuoc, A. G. R. Thomas, V. Yanovsky, L. O. Silva, K. Krushelnick, and Z. Najmudin, "Bright spatially coherent synchrotron X-rays from a table-top source," Nat. Phys. **6**, 980 (2010).

60. S. V Bulanov, F. Pegoraro, A. M. Pukhov, and A. S. Sakharov, "Transverse-wake wave breaking," Phys. Rev. Lett. **78**, 4205 (1997).

61. S. P. D. Mangles, G. Genoud, M. S. Bloom, M. Burza, Z. Najmudin, A. Persson, K. Svensson, A. G. R. Thomas, and C. G. Wahlström, "Self-injection threshold in self-guided laser wakefield accelerators," Phys. Rev. Spec. Top. - Accel. Beams **15**, 011302 (2012).

62. S. Y. Kalmykov, A. Beck, S. A. Yi, V. N. Khudik, M. C. Downer, E. Lefebvre, B. A. Shadwick, and D. P. Umstadter, "Electron self-injection into an evolving plasma bubble: Quasi monoenergetic laser-plasma acceleration in the blowout regime," Phys. Plasmas **18**, 56704 (2011).

63. S. Bulanov, N. Naumova, F. Pegoraro, and J. Sakai, "Particle injection into the wave acceleration phase due to nonlinear wake wave breaking," Phys. Rev. E **58**, R5257 (1998).

64. A. Pak, K. A. Marsh, S. F. Martins, W. Lu, W. B. Mori, and C. Joshi,

"Injection and trapping of tunnel-ionized electrons into laser-produced wakes," Phys. Rev. Lett. **104**, 025003 (2010).

65. C. McGuffey, A. G. R. Thomas, W. Schumaker, T. Matsuoka, V. Chvykov, F. J. Dollar, G. Kalintchenko, V. Yanovsky, A. Maksimchuk, K. Krushelnick, V. Y. Bychenkov, I. V. Glazyrin, and A. V. Karpeev, "Ionization induced trapping in a laser wakefield accelerator," Phys. Rev. Lett. **104**, 025004 (2010).

66. M. Didomenico, J. E. Geusic, H. M. Marcos, and R. G. Smith, "Generation of ultrashort optical pulses by mode locking the YAIG: Nd laser," Appl. Phys. Lett. **8**, 180 (1966).

67. K. Zhao, Q. Zhang, M. Chini, Y. Wu, X. Wang, and Z. Chang, "Tailoring a 67 attosecond pulse through advantageous phase-mismatch," Opt. Lett. **37**, 3891 (2013).

68. D. Strickland and G. Mourou, "Compression of Amplified Chirped Optical Pulses," Opt. Commun. **56**, 219 (1985).

69. G. A. Mourou, T. Tajima, and S. V. Bulanov, "Optics in the relativistic regime," Rev. Mod. Phys. **78**, (2006).

70. B. E. A. Saleh and M. C. Teich, "*Fundamentals of Photonics*" (Wiley, 2007).

71. R. L. Fork, O. E. Martinez, and J. P. Gordon, "Negative dispersion using pairs of prisms.," Opt. Lett. **9**, 150 (1984).

72. E. Martinez, J. P. Gordon, and R. L. Fork, "Negative group-velocity dispersion using refraction.," J. Opt. Soc. AM. A **1**, 1003 (1984).

73. S. Backus, C. G. Durfee, M. M. Murnane, H. C. Kapteyn, and I. Introduction, " High power ultrafast lasers," Rev. Sci. Instrum. **69**, 1207 (1998).

74. E. B. Treacy, "Optical Pulse Compression With Diffraction Gratings," IEEE J. Quantum Electron. **5**, 454 (1969).

75. S. Kane and J. Squier, "Fourth-order-dispersion limitations of aberration-free chirped-pulse amplification systems," J. Opt. Soc. Am. B **14**, 1237 (1997).

76. R. L. Fork, C. H. Brito Cruz, P. C. Becker, and C. V. Shank, "Compression of optical pulses to six femtoseconds by using cubic phase compensation," Opt. Lett. **12**, 483 (1987).

77. B. E. Lemoff and C. P. J. Barty, "Quintic-phase-limited, spatially uniform expansion and recompression of ultrashort optical pulses," Opt. Lett. **18**, 1651 (1993).

78. R. Szipocs, K. Ferencz, C. Spielmann, and F. Krausz, "Chirped multilayer

coatings for broadband dispersion control in femtosecond lasers," Opt. Lett. **19**, 201 (1994).

79. V. Pervak, I. Ahmad, M. K. Trubetskov, A. V. Tikhonravov, and F. Krausz, "Double-angle multilayer mirrors with smooth dispersion characteristics," Opt. Express **17**, 7943 (2009).

80. V. Shumakova, P. Malevich, S. Ališauskas, A. Voronin, A. M. Zheltikov, D. Faccio, D. Kartashov, A. Baltuška, and A. Pugzlys, "Multi-millijoule few-cycle mid-infrared pulses through nonlinear self-compression in bulk," Nat. Commun. **7**, 12877 (2016).

81. M. Hemmer, M. Baudisch, A. Thai, A. Couairon, and J. Biegert, "Self-compression to sub-3-cycle duration of mid-infrared optical pulses in dielectrics," Opt. Express **21**, 28095 (2013).

82. S. Skupin, G. Stibenz, L. Bergé, F. Lederer, T. Sokollik, M. Schnürer, N. Zhavoronkov, and G. Steinmeyer, "Self-compression by femtosecond pulse filamentation: Experiments versus numerical simulations," Phys. Rev. E **74**, 056604 (2006).

83. P. F. Moulton, "Spectroscopic and laser characteristics of Ti:Al2O3," J. Opt. Soc. Am. B **3**, 125 (1986).

84. E. W. Gaul, M. Martinez, J. Blakeney, A. Jochmann, M. Ringuette, D. Hammond, T. Borger, R. Escamilla, S. Douglas, W. Henderson, G. Dyer, A. Erlandson, R. Cross, J. Caird, C. Ebbers, and T. Ditmire, "Demonstration of a 1.1 petawatt laser based on a hybrid optical parametric chirped pulse amplification/mixed Nd:glass amplifier.," Appl. Opt. **49**, 1676 (2010).

85. D. E. Spence, P. N. Kean, and W. Sibbett, "60-Femtosecond pulse generation from a self-mode-locked Ti:sapphire laser," Opt. Lett. **16**, 42 (1991).

86. F. Salin, J. Squier, and M. Piché, "Mode locking of Ti:Al2O3 lasers and self-focusing: a Gaussian approximation," Opt. Lett. **16**, 1674 (1991).

87. C. Grebing, S. Koke, B. Manschwetus, and G. Steinmeyer, "Performance comparison of interferometer topologies for carrier-envelope phase detection," Appl. Phys. B Lasers Opt. **95**, 81 (2009).

88. L. Xu, G. Tempea, A. Poppe, M. Lenzner, C. Spielmann, F. Krausz, A. Stingl, and K. Ferencz, "High-power sub-10-fs Ti:sapphire oscillators," Appl. Phys. B Lasers Opt. **65**, 151 (1997).

89. U. Morgner, S. H. Cho, Y. Chen, H. A. Haus, J. G. Fujimoto, E. P. Ippen, V. Scheuer, G. Angelow, and T. Tschudi, "Sub-two-cycle pulses from a Kerr-lens mode-locked Ti : sapphire laser," Opt. Lett. **24**, 411 (1999).

90. J. K. Wahlstrand, Y. H. Cheng, and H. M. Milchberg, "High field optical nonlinearity and the Kramers-Kronig relations," Phys. Rev. Lett. **109**, 113904 (2012).

91. J. K. Wahlstrand, Y. H. Cheng, and H. M. Milchberg, "Absolute measurement of the transient optical nonlinearity in N 2, O 2, N 2O, and Ar," Phys. Rev. A - At. Mol. Opt. Phys. **85**, 43820 (2012).

92. D. R. Herriott and H. J. Schulte, "Folded Optical Delay Lines," Appl. Opt. **4**, 883 (1965).

93. K. Fritsch, M. Poetzlberger, V. Pervak, J. Brons, and O. Pronin, "All-solid-state multipass spectral broadening to sub-20 fs," Opt. Lett. **43**, 4643 (2018).

94. C.-H. Lu, Y.-J. Tsou, H.-Y. Chen, B.-H. Chen, Y.-C. Cheng, S.-D. Yang, M.-C. Chen, C.-C. Hsu, and A. H. Kung, "Generation of intense supercontinuum in condensed media," Optica **1**, 400 (2014).

95. P. He, Y. Liu, K. Zhao, H. Teng, X. He, P. Huang, H. Huang, S. Zhong, Y. Jiang, S. Fang, X. Hou, and Z. Wei, "High-efficiency supercontinuum generation in solid thin plates at 01 TW level," Opt. Lett. **42**, 474 (2017).

96. E. W. Rosenthal, N. Jhajj, I. Larkin, S. Zahedpour, J. K. Wahlstrand, and H. M. Milchberg, "Energy deposition of single femtosecond filaments in the atmosphere," Opt. Lett. **41**, 3908 (2016).

97. C. P. Hauri, W. Kornelis, F. W. Helbing, A. Heinrich, A. Couairon, A. Mysyrowicz, J. Biegert, and U. Keller, "Generation of intense, carrier-envelope phase-locked few-cycle laser pulses through filamentation," Appl. Phys. B Lasers Opt. **79**, 673 (2004).

98. M. Nisoli, S. De Silvestri, and O. Svelto, "Generation of high energy 10 fs pulses by a new pulse compression technique," Appl. Phys. Lett. **68**, 2793 (1996).

99. T. Balciunas, C. Fourcade-Dutin, G. Fan, T. Witting, A. A. Voronin, A. M. Zheltikov, F. Gerome, G. G. Paulus, A. Baltuska, and F. Benabid, "A strong-field driver in the single-cycle regime based on self-compression in a kagome fibre," Nat. Commun. **6**, 6117 (2015).

100. K. F. Mak, J. C. Travers, N. Y. Joly, A. Abdolvand, and P. S. J. Russell, "Two techniques for temporal pulse compression in gas-filled hollow-core kagomé photonic crystal fiber," Opt. Lett. **38**, 3592 (2013).

101. D. Herrmann, L. Veisz, R. Tautz, F. Tavella, K. Schmid, V. Pervak, and F. Krausz, "Generation of sub-three-cycle, 16 TW light pulses by using noncollinear optical parametric chirped-pulse amplification," Opt. Lett. **34**, 2459 (2009).

102. H. Fattahi, H. G. Barros, M. Gorjan, T. Nubbemeyer, B. Alsaif, C. Y. Teisset, M. Schultze, S. Prinz, M. Haefner, M. Ueffing, A. Alismail, L. Vámos, A. Schwarz, O. Pronin, J. Brons, X. T. Geng, G. Arisholm, M. Ciappina, V. S. Yakovlev, D.-E. Kim, A. M. Azzeer, N. Karpowicz, D. Sutter, Z. Major, T. Metzger, and F. Krausz, "Third-generation femtosecond technology," Optica **1**, 45 (2014).

103. R. F. Cregan., B. J. Mangan, J. C. Knight, T. A. Birks, P. S. J. Russell, P. J. Roberts, and D. C. Allan, "Single-Mode Photonic Band Gap Guidance of Light in Air," Science **285**, 1537 (1999).

104. E. A. J. Marcatili and R. A. Schmeltzer, "Hollow Metallic and Dielectric Waveguides for Long Distance Optical Transmission and Lasers," Bell Syst. Tech. J. **43**, 1783 (1964).

105. T. Nagy, M. Forster, and P. Simon, "Flexible hollow fiber for pulse compressors," Appl. Opt. **47**, 3264 (2008).

106. R. L. Abrams, "Coupling Losses in Hollow Waveguide Laser Resonators," IEEE journal of quantum electronics. **QE-8**, 838 (1972).

107. P. Belland and J. P. Crenn, "Gaussian approximation of the waveguide EH11 mode pattern in the far field," Opt. Commun. **45**, 165 (1983).

108. T. Nagy, V. Pervak, and P. Simon, "Optimal pulse compression in long hollow fibers," Opt. Lett. **36**, 4422 (2011).

109. C. Vozzi, M. Nisoli, G. Sansone, S. Stagira, and S. De Silvestri, "Optimal spectral broadening in hollow-fiber compressor systems," Appl. Phys. B Lasers Opt. **80**, 285 (2005).

110. S. Zahedpour, J. K. Wahlstrand, and H. M. Milchberg, "Measurement of the nonlinear refractive index of air constituents at mid-infrared wavelengths," Opt. Lett. **40**, 5794 (2015).

111. Á. Börzsönyi, Z. Heiner, A. P. Kovács, M. P. Kalashnikov, and K. Osvay, "Measurement of pressure dependent nonlinear refractive index of inert gases," Opt. Express **18**, 25847 (2010).

112. A. Suda, M. Hatayama, K. Nagasaka, and K. Midorikawa, "Generation of sub-10-fs, 5-mJ-optical pulses using a hollow fiber with a pressure gradient," Appl. Phys. Lett. **86**, 111116 (2005).

113. S. Bohman, A. Suda, T. Kanai, S. Yamaguchi, and K. Midorikawa, "Generation of 50 fs, 50 mJ pulses at 1 kHz using hollow-fiber pulse compression," Opt. Lett. **35**, 1887 (2010).

114. F. Böhle, M. Kretschmar, A. Jullien, M. Kovacs, M. Miranda, R. Romero, H.

Crespo, U. Morgner, P. Simon, R. Lopez-Martens, and T. Nagy, "Compression of CEP-stable multi-mJ laser pulses down to 4 fs in long hollow fibers," Laser Phys. Lett. **11**, 095401 (2014).

115. V. Cardin, N. Thiré, S. Beaulieu, V. Wanie, F. Légaré, and B. E. Schmidt, "0.42 TW 2-cycle pulses at 1.8 μ m via hollow-core fiber compression," Appl. Phys. Lett. **107**, 181101 (2015).

116. S. C. Pinault and M. J. Potasek, "Frequency broadening by self-phase modulation in optical fibers," J. Opt. Soc. Am. B **2**, 1318 (1985).

117. R. Trebino, "*Frequency-Resolved Optical Gating: The Measurement of Ultrashort Laser Pulses*" (Springer US, 2000).

118. L. Gallmann, D. H. Sutter, N. Matuschek, G. Steinmeyer, U. Keller, C. Iaconis, and I. A. Walmsley, "Characterization of sub-6-fs optical pulses with spectral phase interferometry for direct electric-field reconstruction," Opt. Lett. **24**, 1314 (1999).

119. M. Miranda, T. Fordell, C. Arnold, A. L'Huillier, and H. Crespo, "Simultaneous compression and characterization of ultrashort laser pulses using chirped mirrors and glass wedges," Opt. Express **20**, 688 (2012).

120. M. Miranda, C. L. Arnold, T. Fordell, F. Silva, B. Alonso, R. Weigand, A. L'Huillier, and H. Crespo, "Characterization of broadband few-cycle laser pulses with the d-scan technique," Opt. Express **20**, 18732 (2012).

121. T. Witting, D. Greening, D. Walke, P. Matia-Hernando, T. Barillot, J. P. Marangos, and J. W. G. Tisch, "Time-domain ptychography of over-octave-spanning laser pulses in the single-cycle regime," Opt. Lett. **41**, 4218 (2016).

122. H. J. Eichler, "Introduction to the Special Issue on Dynamic Gratings and Four-Wave Mixing," IEEE J. Quantum Electron. **22**, 1194 (1986).

123. M. Li, J. P. Nibarger, C. Guo, and G. N. Gibson, "Dispersion-free transient-grating frequency-resolved Optical Gating," Appl. Opt. **38**, 5250 (1999).

124. J. N. Sweetser, D. N. Fittinghoff, and R. Trebino, "Transient-grating frequency-resolved optical gating," Opt. Lett. **22**, 519 (1997).

125. D. Lee, S. Akturk, P. Gabolde, and R. Trebino, "Experimentally simple, extremely broadband transient-grating frequency-resolved-opticalgating arrangement," Opt. Express **15**, 760 (2007).

126. R. Trebino and D. J. Kane, "Using phase retrieval to measure the intensity and phase of ultrashort pulses: frequency-resolved optical gating," J. Opt. Soc. Am. A **10**, 1101 (1993).

127. K. W. Delong and R. Trebino, "for frequency-resolved optical gating," J. Opt. Soc. AM. A. **11**, 2429 (1994).

128. Y. Fukuda, A. Y. Faenov, M. Tampo, T. A. Pikuz, T. Nakamura, M. Kando, Y. Hayashi, A. Yogo, H. Sakaki, T. Kameshima, A. S. Pirozhkov, K. Ogura, M. Mori, T. Z. Esirkepov, J. Koga, A. S. Boldarev, V. A. Gasilov, A. I. Magunov, T. Yamauchi, R. Kodama, P. R. Bolton, Y. Kato, T. Tajima, H. Daido, and S. V. Bulanov, "Energy Increase in Multi-MeV Ion Acceleration in the Interaction of a Short Pulse Laser with a Cluster-Gas Target," Phys. Rev. Lett. **103**, 165002 (2009).

129. A. Lifschitz, F. Sylla, S. Kahaly, A. Flacco, M. Veltcheva, G. Sanchez-Arriaga, E. Lefebvre, and V. Malka, "Ion acceleration in underdense plasmas by ultra-short laser pulses," New J. Phys. **16**, 033031 (2014).

130. C. Gahn, G. D. Tsakiris, A. Pukhov, J. Meyer-Ter-Vehn, G. Pretzler, P. Thirolf, D. Habs, and K. J. Witte, "Multi-MeV electron beam generation by direct laser acceleration in high-density plasma channels," Phys. Rev. Lett. **83**, 4772 (1999).

131. A. Willner, F. Tavella, M. Yeung, T. Dzelzainis, C. Kamperidis, M. Bakarezos, D. Adams, M. Schulz, R. Riedel, M. C. Hoffmann, W. Hu, J. Rossbach, M. Drescher, N. A. Papadogiannis, M. Tatarakis, B. Dromey, and M. Zepf, "Coherent control of high harmonic generation via dual-gas multijet arrays," Phys. Rev. Lett. **107**, 175002 (2011).

132. C. Altucci, C. Beneduce, R. Bruzzese, C. De Lisio, G. S. Sorrentino, T. Starczewski, and F. Vigilante, "Characterization of pulsed gas sources for intense laser field-atom interaction experiments," J. Phys. D. Appl. Phys. **29**, 68 (1996).

133. A. Depresseux, E. Oliva, J. Gautier, F. Tissandier, G. Lambert, B. Vodungbo, J.-P. P. Goddet, A. Tafzi, J. Nejdl, M. Kozlova, G. Maynard, H. T. Kim, K. T. Phuoc, A. Rousse, P. Zeitoun, S. Sebban, K. Ta Phuoc, A. Rousse, P. Zeitoun, and S. Sebban, "Demonstration of a Circularly Polarized Plasma-Based Soft-X-Ray Laser," Phys. Rev. Lett. **115**, 083901 (2015).

134. T. Ditmire, J. Zweiback, V. P. Yanovsky, T. E. Cowan, G. Hays, and K. B. Wharton, "Nuclear fusion from explosions of femtosecond laser-heated deuterium clusters," Nature **398**, 489 (1999).

135. M. Krishnan, K. W. Elliott, C. G. R. R. Geddes, R. A. van Mourik, W. P. Leemans, H. Murphy, and M. Clover, "Electromagnetically driven, fast opening and closing gas jet valve," Phys. Rev. Spec. Top. - Accel. Beams **14**, 033502 (2011).

136. F. Sylla, M. Veltcheva, S. Kahaly, A. Flacco, and V. Malka, "Development

and characterization of very dense submillimetric gas jets for laser-plasma interaction," Rev. Sci. Instrum. **83**, 033507 (2012).

137. E. Parra, S. J. McNaught, and H. M. Milchberg, "Characterization of a cryogenic, high-pressure gas jet operated in the droplet regime," Rev. Sci. Instrum. **73**, 468 (2002).

138. S. Semushin and V. Malka, "High density gas jet nozzle design for laser target production," Rev. Sci. Instrum. **72**, 2961 (2001).

139. R. Azambuja, M. Eloy, G. Figueira, and D. Neely, "Three-dimensional characterization of high-density non-cylindrical pulsed gas jets," J. Phys. D. Appl. Phys. **32**, L35 (1999).

140. A. Murakami, J. Miyazawa, H. Tsuchiya, T. Murase, N. Ashikawa, T. Morisaki, R. Sakamoto, and H. Yamada, "Characteristics of hydrogen supersonic cluster beam generated by a Laval nozzle," J. Plasma Fusion Res. Ser. **9**, 79 (2010).

141. J. Fan, T. R. Clark, and H. M. Milchberg, "Generation of a plasma waveguide in an elongated, high repetition rate gas jet," Appl. Phys. Lett. **73**, 3064 (1998).

142. D. Kaganovich, M. H. Helle, D. F. Gordon, and A. Ting, "Measurements and simulations of shock wave generated plasma-vacuum interface," Phys. Plasmas **18**, 120701 (2011).

143. A. Buck, J. Wenz, J. Xu, K. Khrennikov, K. Schmid, M. Heigoldt, J. M. Mikhailova, M. Geissler, B. Shen, F. Krausz, S. Karsch, and L. Veisz, "Shock-front injector for high-quality laser-plasma acceleration," Phys. Rev. Lett. **110**, 185006 (2013).

144. B. D. Layer, A. G. York, S. Varma, Y.-H. Chen, and H. M. Milchberg, "Periodic index-modulated plasma waveguide.," Opt. Express **17**, 4263 (2009).

145. S. J. J. Yoon, A. J. J. Goers, G. A. A. Hine, J. D. D. Magill, J. A. A. Elle, Y.-H. H. Chen, M. Milchberg, and H. M. Milchberg, "Shock formation in supersonic cluster jets and its effect on axially modulated laser-produced plasma waveguides," Opt. Express **21**, 15878 (2013).

146. T. Nakamura, S. V. Bulanov, T. Z. Esirkepov, and M. Kando, "High-energy ions from near-critical density plasmas via magnetic vortex acceleration," Phys. Rev. Lett. **105**, 135002 (2010).

147. D. Haberberger, S. Tochitsky, F. Fiuza, C. Gong, R. a. Fonseca, L. O. Silva, W. B. Mori, and C. Joshi, "Collisionless shocks in laser-produced plasma generate monoenergetic high-energy proton beams," Nat. Phys. **8**, 95 (2012).

148. U. Even, "The Even-Lavie valve as a source for high intensity supersonic

beam," EPJ Tech. Instrum. 2 (2015).

149. K. Schmid and L. Veisz, "Supersonic gas jets for laser-plasma experiments," Rev. Sci. Instrum. **83**, 053304 (2012).

150. D. B. Atkinson and M. A. Smith, "Design and characterization of pulsed uniform supersonic expansions for chemical applications," Rev. Sci. Instrum. **66**, 4434 (1995).

151. N. Lemos, N. Lopes, J. M. Dias, and F. Viola, "Design and characterization of supersonic nozzles for wide focus laser-plasma interactions," Rev. Sci. Instrum. **80**, 103301 (2009).

152. P. M. Gerhart, R. J. Gross, and J. I. Hochstein, "*Fundamentals of Fluid Mechanics*" (Addison-Wesley, 1992).

153. P. H. Oosthuizen and W. E. Carscallen, "*Compressible Fluid Flow*" (McGraw-Hill, 1997).

154. S. P. Nikitin, T. M. Antonsen, T. R. Clark, Y. L. Li, and H. M. Milchberg, "Guiding of intense femtosecond pulses in preformed plasma channels," Opt. Lett. **22**, 1787 (1997).

155. K. Y. Kim, V. Kumarappan, and H. M. Milchberg, "Measurement of the average size and density of clusters in a gas jet," Appl. Phys. Lett. **83**, 3210 (2003).

156. M. Takeda, H. Ina, and S. Kobayashi, "Fourier-transform method of fringe-pattern analysis for computer-based topography and interferometry," J. Opt. Soc. Am. **72**, 156 (1982).

157. M. Kalal and K. A. Nugent, "Abel inversion using fast Fourier transforms," Appl. Opt. **27**, 1956 (1988).

158. B. R. Munson, D. F. Young, and T. H. Okiishi, "*Fundamentals of Fluid Mechanics*", 2nd ed. (John Wiley & Sons, Inc., 1997).

159. H. M. Milchberg, K. Y. Kim, V. Kumarappan, B. D. Layer, and H. Sheng, "Clustered gases as a medium for efficient plasma waveguide generation," Phil. Trans. R. Soc. A **364**, 647 (2006).

160. T. Ditmire, T. Donnelly, R. W. Falcone, and M. D. Perry, "Strong x-ray emission from high-temperature plasmas produced by intense irradiation of clusters," Phys. Rev. Lett. **75**, 3122 (1995).

161. Y. Fukuda, H. Sakaki, M. Kanasaki, A. Yogo, S. Jinno, M. Tampo, A. Y. Faenov, T. A. Pikuz, Y. Hayashi, M. Kando, A. S. Pirozhkov, T. Shimomura, H. Kiriyama, S. Kurashima, T. Kamiya, K. Oda, T. Yamauchi, K. Kondo, and

S. V. Bulanov, "Identification of high energy ions using backscattered particles in laser-driven ion acceleration with cluster-gas targets," Radiat. Meas. **50**, 92 (2013).

162. L. M. Chen, J. J. Park, K. H. Hong, J. L. Kim, J. Zhang, and C. H. Nam, "Emission of a hot electron jet from intense femtosecond-laser-cluster interactions," Phys. Rev. E **66**, 025402 (2002).

163. Y. L. Shao, T. Ditmire, J. W. G. Tisch, E. Springate, J. P. Marangos, and M. H. R. Hutchinson, "Multi-keV electron generation in the interaction of intense laser pulses with Xe clusters," Phys. Rev. Lett. **77**, 3343 (1996).

164. T. Caillaud, F. Blasco, F. Dorchies, Y. Glinec, C. Stenz, and J. Stevefelt, "Experimental study of K-shell X-ray emission from argon clusters irradiated by an ultra-intense laser pulse," Nucl. Instruments Methods Phys. Res. Sect. B **205**, 329 (2003).

165. T. Ditmire, J. Zweiback, V. P. Yanovsky, T. E. Cowan, G. Hays, and K. B. Wharton, "Nuclear fusion in gases of deuterium clusters heated with a femtosecond laser," Phys. Plasmas **7**, 1993 (2000).

166. C. Lettieri, D. Yang, and Z. Spakovszky, "An Investigation of Condensation Effects in Supercritical Carbon Dioxide Compressors," J. Eng. Gas Turbines Power **137**, 082602 (2015).

167. G. Gyarmathy, "Nucleation of steam in high-pressure nozzle experiments," Proc. Inst. Mech. Eng. Part A J. Power Energy **219**, 511 (2005).

168. O. F. Hagena, "Cluster Formation in Expanding Supersonic Jets: Effect of Pressure, Temperature, Nozzle Size, and Test Gas The," Rev. Sci. Instrum. **63**, 2374 (1992).

169. O. F. Hagena and W. Obert, "Cluster formation in expanding supersonic jets: effect of pressure, temperature, nozzle size, and test gas," J. Chem. Phys. **56**, 1793 (1972).

170. O. F. Hagena, "Nucleation and growth of clusters in expanding nozzle flows," Surf. Sci. **106**, 101 (1981).

171. D. G. Jang, Y. S. You, H. M. Milchberg, H. Suk, and K. Y. Kim, "All-optical characterization of cryogenically cooled argon clusters in continuous gas jets," Appl. Phys. Lett. **105**, 021906 (2014).

172. W. F. Louisos, A. A. Alexeenko, D. L. Hitt, and A. Zilic, "Design considerations for supersonic micronozzles," Int. J. Manuf. Res. **3**, 80 (2008).

173. S. P. D. D. Mangles, B. R. Walton, Z. Najmudin, A. E. Dangor, K. Krushelnick, V. Malka, M. Manclossi, N. Lopes, C. Carias, G. Mendes, and F.

Dorchies, "Table-top laser-plasma acceleration as an electron radiography source," Laser Part. Beams **24**, 185 (2006).

174. R. D. Edwards, M. A. Sinclair, T. J. Goldsack, K. Krushelnick, F. N. Beg, E. L. Clark, A. E. Dangor, Z. Najmudin, M. Tatarakis, B. Walton, M. Zepf, K. W. D. Ledingham, I. Spencer, P. A. Norreys, R. J. Clarke, R. Kodama, Y. Toyama, and M. Tampo, "Characterization of a gamma-ray source based on a laser-plasma accelerator with applications to radiography," Appl. Phys. Lett **80**, 2129 (2002).

175. Z. H. He, B. Hou, J. A. Nees, J. H. Easter, J. Faure, K. Krushelnick, and A. G. R. Thomas, "High repetition-rate wakefield electron source generated by few-millijoule, 30 fs laser pulses on a density downramp," New J. Phys. **15**, 053016 (2013).

176. Z. H. He, A. G. R. Thomas, B. Beaurepaire, J. A. Nees, B. Hou, V. Malka, K. Krushelnick, and J. Faure, "Electron diffraction using ultrafast electron bunches from a laser-wakefield accelerator at kHz repetition rate," Appl. Phys. Lett. **102**, 064104 (2013).

177. A. G. Mordovanakis, J. Easter, N. Naumova, K. Popov, P. E. Masson-Laborde, B. Hou, I. Sokolov, G. Mourou, I. V. Glazyrin, W. Rozmus, V. Bychenkov, J. Nees, and K. Krushelnick, "Quasimonoenergetic electron beams with relativistic energies and ultrashort duration from laser-solid interactions at 0.5 kHz," Phys. Rev. Lett. **103**, 235001 (2009).

178. S. Feister, D. R. Austin, J. T. Morrison, K. D. Frische, C. Orban, G. Ngirmang, A. Handler, J. R. H. Smith, M. Schillaci, J. A. LaVerne, E. A. Chowdhury, R. R. Freeman, and W. M. Roquemore, "Relativistic electron acceleration by mJ-class kHz lasers normally incident on liquid targets," Opt. Express **25**, 18736 (2017).

179. G. Sciaini and R. J. D. D. Miller, "Femtosecond electron diffraction: Heralding the era of atomically resolved dynamics," Reports Prog. Phys. **74**, 096101 (2011).

180. B. Miao, L. Feder, J. Elle, A. J. Goers, D. Woodbury, F. Salehi, J. K. Wahlstrand, and H. M. Milchberg, "Coherent ultra-broadband laser-assisted injection radiation from a laser plasma accelerator," Phys. Rev. E **98**, 43206 (2018).

181. W. L. Kruer, "*The Physics Of Laser Plasma Interactions*" (Addison-Wesley, 1988).

182. T. R. Clark and H. M. Milchberg, "Time- and space-resolved density evolution of the plasma waveguide," Phys. Rev. Lett. **78**, 2373 (1997).

183. J. Berger, M.J., Coursey, J.S., Zucker, M.A., and Chang, "National Institute of Standards and Technology, 2010, “ESTAR, Stopping Power and Range Tables for Electrons” (http://physics.nist.gov/PhysRefData/Star/Text/ESTAR.html),".

184. Y. Glinec, J. Faure, A. Guemnie-Tafo, V. Malka, H. Monard, J. P. Larbre, V. De Waele, J. L. Marignier, and M. Mostafavi, "Absolute calibration for a broad range single shot electron spectrometer," Rev. Sci. Instrum. **77**, 103301 (2006).

185. A. Buck, K. Zeil, A. Popp, K. Schmid, A. Jochmann, S. D. Kraft, B. Hidding, T. Kudyakov, C. M. S. Sears, L. Veisz, S. Karsch, J. Pawelke, R. Sauerbrey, T. Cowan, F. Krausz, and U. Schramm, "Absolute charge calibration of scintillating screens for relativistic electron detection," Rev. Sci. Instrum. **81**, 033301 (2010).

186. S. Augst, D. D. Meyerhofer, D. Strickland, and S. L. Chint, "Laser ionization of noble gases by Coulomb-barrier suppression," J. Opt. Soc. Am. B **8**, 858 (1991).

187. A. B. Langdon, B. F. Lasinski, and W. L. Kruer, "Nonlinear saturation and recurrence of the two-plasmon decay instability," Phys. Rev. Lett. **43**, 133 (1979).

188. C. B. Schroeder, E. Esarey, C. G. R. Geddes, C. Tóth, B. A. Shadwick, J. van Tilborg, J. Faure, and W. P. Leemans, "Frequency chirp and pulse shape effects in self-modulated laser wakefield accelerators," Phys. Plasmas **10**, 2039 (2003).

189. X. Zhang, B. Shen, L. Ji, W. Wang, J. Xu, Y. Yu, L. Yi, X. Wang, N. A. M. Hafz, and V. Kulagin, "Effect of pulse profile and chirp on a laser wakefield generation," Phys. Plasmas **19**, 053103 (2012).

190. B. S. Rao, A. Moorti, P. A. Naik, and P. D. Gupta, "Effect of chirp on self-modulation and laser wakefield electron acceleration in the regime of quasimonoenergetic electron beam generation," Phys. Rev. Spec. Top. - Accel. Beams **16**, 091301 (2013).

191. W. P. Leemans, P. Catravas, E. Esarey, C. G. R. Geddes, C. Toth, R. Trines, C. B. Schroeder, B. A. Shadwick, J. van Tilborg, and J. Faure, "Electron-yield enhancement in a laser-wakefield accelerator driven by asymmetric laser pulses," Phys. Rev. Lett. **89**, 174802 (2002).

192. B. Beaurepaire, A. Lifschitz, and J. Faure, "Electron acceleration in sub-relativistic wakefields driven by few-cycle laser pulses," New J. Phys. **16**, 023023 (2014).

193. D. Umstadter, S.-Y. Chen, A. Maksimchuk, G. Mourou, and R. Wagner, "Nonlinear Optics in Relativistic Plasmas and Laser Wake Field Acceleration

of Electrons," Science **273**, 472 (1996).

194. C. I. Moore, A. Ting, K. Krushelnick, E. Esarey, R. F. Hubbard, B. Hafizi, H. R. Burris, C. Manka, and P. Sprangle, "Electron Trapping in Self-Modulated Laser Wakefields by Raman Backscatter," Phys. Rev. Lett. **79**, 3909 (1997).

195. A. Ting, C. I. Moore, K. Krushelnick, C. Manka, E. Esarey, P. Sprangle, R. Hubbard, H. R. Burris, R. Fischer, and M. Baine, "Plasma wakefield generation and electron acceleration in a self-modulated laser wakefield accelerator experiment," Phys. Plasmas **4**, 1889 (1997).

196. C. Gahn, G. D. Tsakiris, G. Pretzler, K. J. Witte, P. Thirolf, D. Habs, C. Delfin, and C.-G. Wahlström, "Generation of MeV electrons and positrons with femtosecond pulses from a table-top laser system," Phys. Plasmas **9**, 987 (2002).

197. D. Woodbury, L. Feder, V. Shumakova, C. Gollner, R. Schwartz, B. Miao, F. Salehi, A. Korolov, A. Pugžlys, A. Baltuška, and H. M. Milchberg, "Laser wakefield acceleration with mid-IR laser pulses," Opt. Lett. **43**, 1131 (2018).

198. A. Pukhov, J. Meyer-ter-vehn, and A. Physics, "Laser wake field acceleration : the highly non-linear broken-wave regime," Appl. Phys. B **B 74**, 355 (2002).

199. C. D. Decker, W. B. Mori, K. C. Tzeng, and T. Katsouleas, "The evolution of ultra intense, short pulse lasers in underdense plasmas," Phys. Plasmas **3**, 2047 (1996).

200. P. Mora and T. M. Antonsen, "Kinetic modeling of intense, short laser pulses propagating in tenuous plasmas," Phys. Plasmas **4**, 217 (1997).

201. M. Geissler, J. Schreiber, and J. Meyer-ter-Vehn, "Bubble acceleration of electrons with few-cycle laser pulses," New J. Phys. **8**, 186 (2006).

202. S. Gordienko and A. Pukhov, "Scalings for ultrarelativistic laser plasmas and quasimonoenergetic electrons," Phys. Plasmas **12**, 43109 (2005).

203. D. Guénot, D. Gustas, A. Vernier, B. Beaurepaire, F. Böhle, M. Bocoum, M. Lozano, A. Jullien, R. Lopez-Martens, A. Lifschitz, and J. Faure, "Relativistic electron beams driven by kHz single-cycle light pulses," Nat. Photonics **11**, 293 (2017).

204. C. Ren, B. J. Duda, R. G. Hemker, W. B. Mori, T. Katsouleas, T. M. Antonsen, and P. Mora, "Compressing and focusing a short laser pulse by a thin plasma lens," Phys. Rev. E **63**, 026411 (2001).

205. A. F. Lifschitz and V. Malka, "Optical phase effects in electron wakefield acceleration using few-cycle laser pulses," New J. Phys. **14**, 053045 (2012).

206. J. Faure, D. Gustas, D. Guénot, A. Vernier, F. Böhle, M. Ouillé, S. Haessler, R. Lopez-Martens, and A. Lifschitz, "A review of recent progress on laser-plasma acceleration at kHz repetition rate," Plasma Phys. Control. Fusion **61**, 014012 (2019).

207. X. L. Xu, F. Li, W. An, T. N. Dalichaouch, P. Yu, W. Lu, C. Joshi, and W. B. Mori, "High quality electron bunch generation using a longitudinal density-tailored plasma-based accelerator in the three-dimensional blowout regime," Phys. Rev. Accel. Beams **20**, 111303 (2017).

208. F. Tavella, Y. Nomura, L. Veisz, V. Pervak, A. Marcinkevičius, and F. Krausz, "Dispersion management for a sub-10-fs, 10 TW optical parametric chirped-pulse amplifier," Opt. Lett. **32**, 2227 (2007).

209. K. Schmid, L. Veisz, F. Tavella, S. Benavides, R. Tautz, D. Herrmann, A. Buck, B. Hidding, A. Marcinkevicius, U. Schramm, M. Geissler, J. Meyer-Ter-Vehn, D. Habs, and F. Krausz, "Few-cycle laser-driven electron acceleration," Phys. Rev. Lett. **102**, 124801 (2009).

210. D. Gustas, D. Guénot, A. Vernier, S. Dutt, F. Böhle, R. Lopez-Martens, A. Lifschitz, and J. Faure, "High-charge relativistic electron bunches from a kHz laser-plasma accelerator," Phys. Rev. Accel. Beams **21**, 013401 (2018).

211. N. A. M. Hafz, S. K. Lee, T. M. Jeong, and J. Lee, "Evolution of self-injected quasi-monoenergetic electron beams in a plasma bubble," *Nuclear Instruments and Methods in Physics Research A* **637**, S51 (2011).

212. E. N. Nerush and I. Y. Kostyukov, "Carrier-Envelope Phase Effects in Plasma-Based Electron Acceleration with Few-Cycle Laser Pulses," Phys. Rev. Lett. **103**, 035001 (2009).

213. A. Zhidkov, T. Fujii, and K. Nemoto, "Electron self-injection during interaction of tightly focused few-cycle laser pulses with underdense plasma," Phys. Rev. E **78**, 036406 (2008).

214. A. J. Goers, S. J. Yoon, J. A. Elle, G. A. Hine, and H. M. Milchberg, "Laser wakefield acceleration of electrons with ionization injection in a pure N5+ plasma waveguide," Appl. Phys. Lett. **104**, 214105 (2014).

215. C. Liu, J. Zhang, S. Chen, G. Golovin, S. Banerjee, B. Zhao, N. Powers, I. Ghebregziabher, and D. Umstadter, "Adaptive-feedback spectral-phase control for interactions with transform-limited ultrashort high-power laser pulses.," Opt. Lett. **39**, 80 (2014).

216. H. T. Kim, V. B. Pathak, K. Hong Pae, A. Lifschitz, F. Sylla, J. H. Shin, C. Hojbota, S. K. Lee, J. H. Sung, H. W. Lee, E. Guillaume, C. Thaury, K. Nakajima, J. Vieira, L. O. Silva, V. Malka, and C. H. Nam, "Stable multi-GeV

electron accelerator driven by waveform-controlled PW laser pulses," Sci. Rep. **7**, 10203 (2017).

217. Z. H. He, B. Hou, V. Lebailly, J. A. Nees, K. Krushelnick, and A. G. R. Thomas, "Coherent control of plasma dynamics," Nat. Commun. **6**, 7156 (2015).

218. J. Lin, Y. Ma, R. Schwartz, D. Woodbury, J. A. Nees, M. Mathis, A. G. R. Thomas, K. Krushelnick, and H. Milchberg, "Adaptive control of laser-wakefield accelerators driven by mid-IR laser pulses," Opt. Express **27**, 10912 (2019).

219. H. M. Milchberg, S. J. McNaught, and E. Parra, "Plasma hydrodynamics of the intense laser-cluster interaction," Phys. Rev. E **64**, 7 (2001).

220. A. McPherson, B. D. Thompson, A. B. Borisov, K. Boyer, and C. K. Rhodes, "Multiphoton-induced X-ray emission at 4-5 keV from Xe atoms with multiple core vacancies," Nature **370**, 631 (1994).

221. L. M. Chen, W. C. Yan, D. Z. Li, Z. D. Hu, L. Zhang, W. M. Wang, N. Hafz, J. Y. Mao, K. Huang, Y. Ma, J. R. Zhao, J. L. Ma, Y. T. Li, X. Lu, Z. M. Sheng, Z. Y. Wei, J. Gao, and J. Zhang, "Bright betatron X-ray radiation from a laser-driven-clustering gas target," Sci. Rep. **3**, 1912 (2013).

222. T. Ditmire, J. W. G. Tisch, E. Springate, M. B. Mason, N. Hay, R. A. Smith, J. Marangos, and M. H. R. Hutchinson, "High-energy ions produced in explosions of superheated atomic clusters," Nature **386**, 54 (1997).

223. R. Matsui, Y. Fukuda, and Y. Kishimoto, "Quasimonoenergetic Proton Bunch Acceleration Driven by Hemispherically Converging Collisionless Shock in a Hydrogen Cluster Coupled with Relativistically Induced Transparency," Phys. Rev. Lett. **122**, 014804 (2019).

224. M. Mirzaie, N. A. M. Hafz, S. Li, K. Gao, G. Li, Qurat-Ul-Ain, and J. Zhang, "Laser acceleration in argon clusters and gas media," Plasma Phys. Control. Fusion **58**, 034014 (2016).

225. Y. Kishimoto, T. Masaki, and T. Tajima, "High energy ions and nuclear fusion in laser–cluster interaction," Phys. Plasmas **9**, 589 (2002).

226. K. Y. Kim, I. Alexeev, E. Parra, and H. M. Milchberg, "Time-Resolved Explosion of Intense-Laser-Heated Clusters," Phys. Rev. Lett. **90**, 023401 (2003).

227. I. Alexeev, T. M. Antonsen, K. Y. Kim, and H. M. Milchberg, "Self-Focusing of Intense Laser Pulses in a Clustered Gas," Phys. Rev. Lett. **90**, 103402 (2003).

228. D. R. Symes, A. S. Moore, A. J. Comley, J. Lazarus, M. Hohenberger, J. W. G. Tisch, and R. A. Smith, "Blast-wave diagnosis of self-focusing of an intense laser pulse in a cluster medium," Phys. Plasmas **14**, 063102 (2007).

229. H. Kotaki, Y. Hayashi, M. Mori, M. Kando, J. K. Koga, and S. V. Bulanov, "Limitation of the plasma channel due to the frequency blueshift," J. Phys. Conf. Ser. **688**, 012054 (2016).

230. J. K. Koga, N. Naumova, M. Kando, L. N. Tsintsadze, K. Nakajima, S. V. Bulanov, H. Dewa, H. Kotaki, and T. Tajima, "Fixed blueshift of high intensity short pulse lasers propagating in gas chambers," Phys. Plasmas **7**, 5223 (2000).

231. A. M. Bystrov and V. B. Gildenburg, "Infrared to ultraviolet light conversion in laser-cluster interactions," Phys. Rev. Lett. **103**, 083401 (2009).